

**NASA TECHNICAL
TRANSLATION**

NASA TT F-651



NASA TT F-651

2.1

**LOAN COPY: RETURN TO
AFWL (DOG)
KIRTLAND AFB,**

0069201



TECH LIBRARY KAFB, NM

**THE FIRST PANORAMIC VIEWS
OF THE LUNAR SURFACE**

Volume 2

Edited by Yu. I. Yefremov

"Nauka" Press, Moscow, 1969

NATIONAL AERONAUTICS AND SPACE ADMINISTRATION • WASHINGTON, D. C. • FEBRUARY 1971



0069201

NASA 'T' 'F' -001

THE FIRST PANORAMIC VIEWS
OF THE LUNAR SURFACE

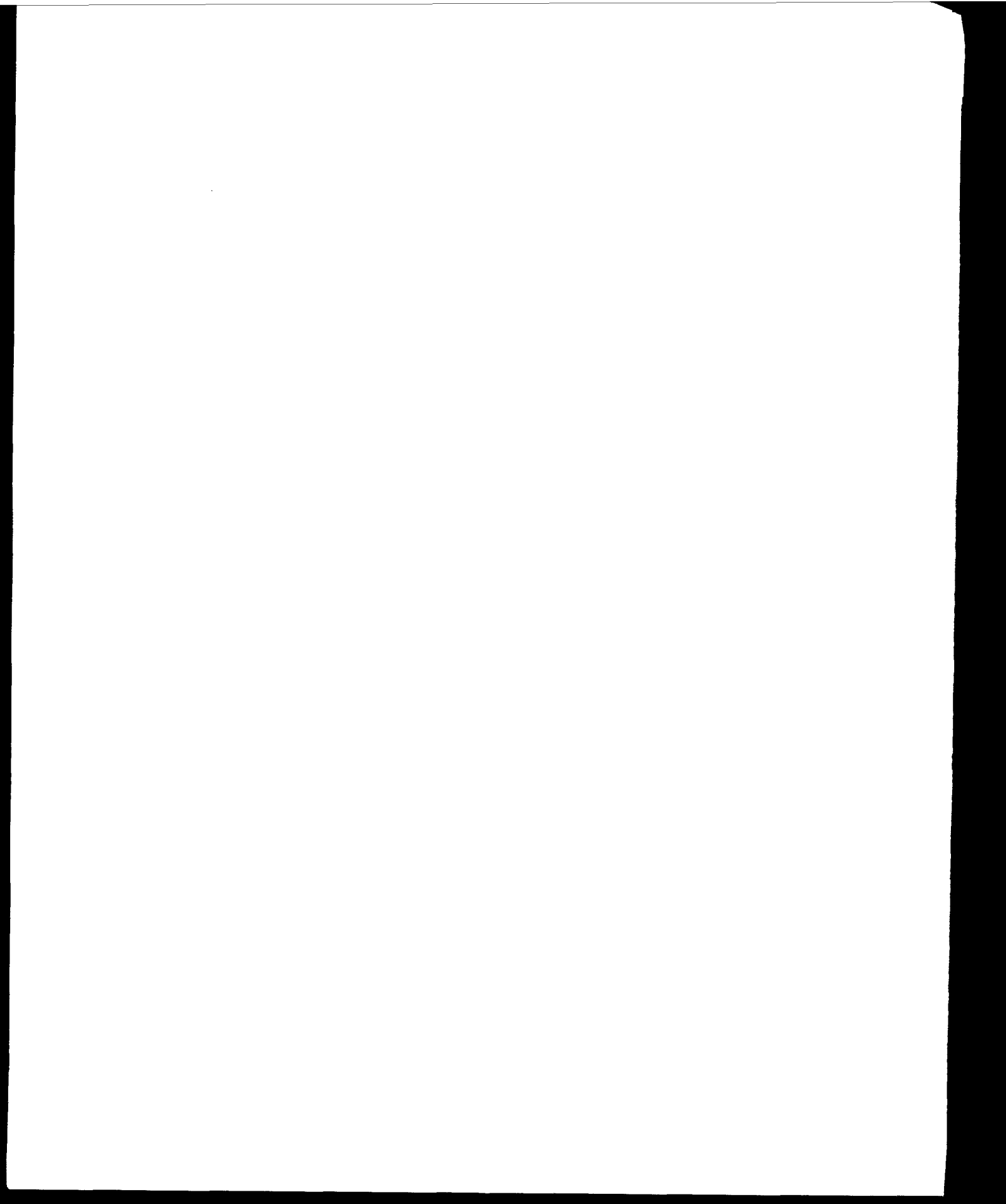
Volume 2

Edited by Yu. I. Yefremov

Translation of "Pervyye panoramy lunnoy poverkhnosti.
Tom II." "Nauka" Press, Moscow, 1969

NATIONAL AERONAUTICS AND SPACE ADMINISTRATION

For sale by the National Technical Information Service, Springfield, Virginia 22151 - Price \$3.00



FOREWORD

The soft landing of the automatic lunar probe "Luna-13" on the surface of the Moon represents new progress in lunar studies by means of space vehicles. "Luna-13" continued the long series of lunar studies that began with the first Moon rocket in 1959.

The panoramic views of the lunar surface transmitted by "Luna-13" have substantially extended the material available for studying the structure of the Moon's surface. "Luna-13" confirmed the earlier conclusions regarding the absence of an appreciable layer of dust, the presence of a great many surface rocks and the prevalence of negative relief forms.

In addition, "Luna-13" made the first direct measurements of the physico-mechanical properties of the surface layer of the lunar soil, representing yet another forward step in the study of the nature of the Moon.

The panoramic views obtained by "Luna-13" are produced with documentary accuracy in this book, together with the preliminary results of their analysis and a description and the results of the experiments made to investigate the physico-mechanical properties of the surface layer of the Moon.

Academy of Sciences USSR

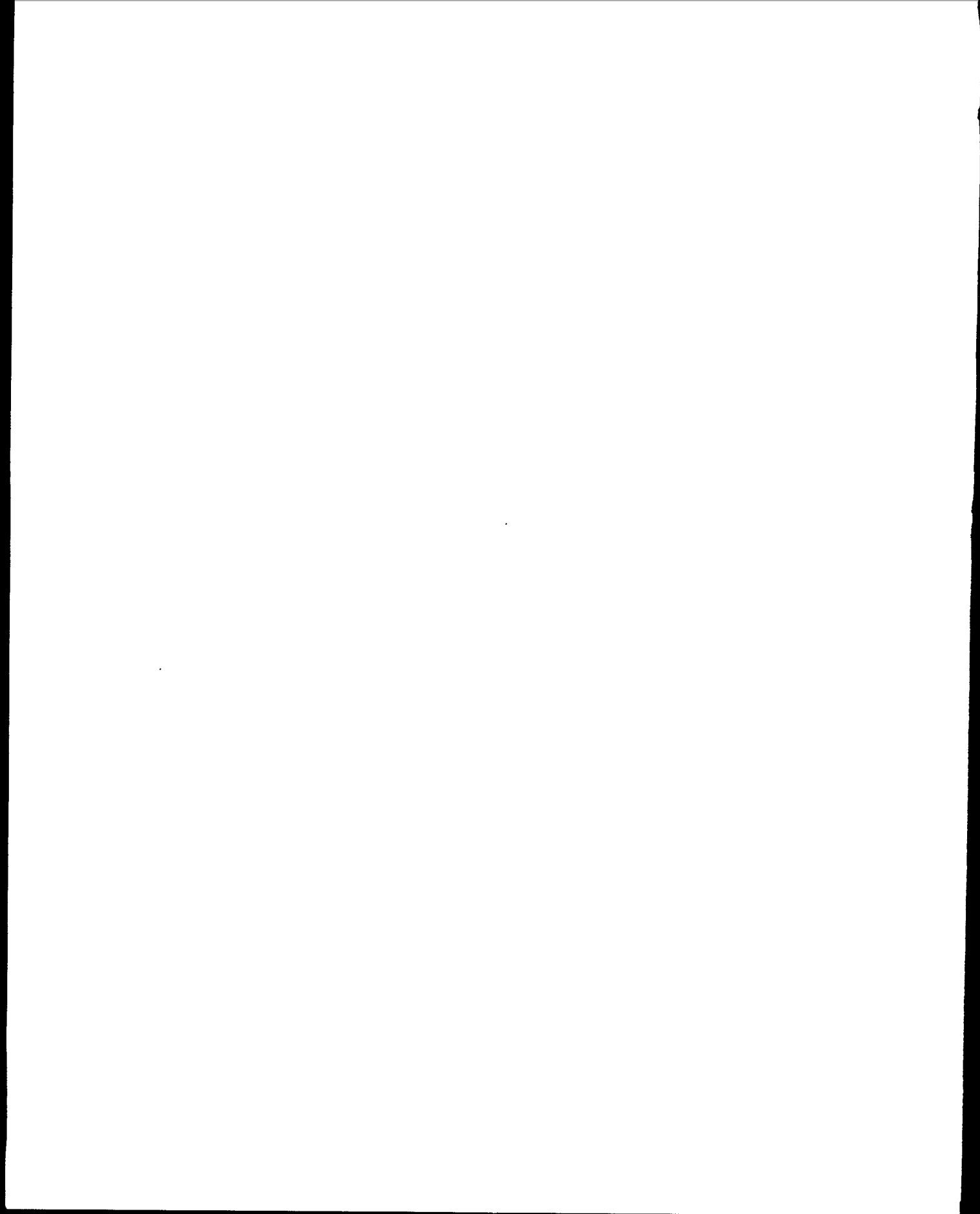


TABLE OF CONTENTS

	Page
FOREWORD	iii
Part I Description of Equipment and Flight Conditions	1
Chapter 1 Lunar Probe Design and Flight Conditions	2
1. The Automatic Lunar Probe "Luna-13"	2
2. Luna-13 Flight Conditions	2
3. Thermal Regulation System	2
4. Mechanisms for Transporting Instruments outside for Investigations of the Luna Surface	5
Chapter 2 Scientific Instrumentation	7
1. Methods of Determining the Mechanical Properties of the Lunar Soil	7
2. Ground-Penetrometer	7
3. Radiation Densimeter	9
4. Dynamograph	12
5. Radiometer	12
Part II Results of the Scientific Investigations	16
Chapter 1 Investigations of the Properties of the Lunar Soil	17
1. Simulated Materials	17
2. Calibration of Radiation Densimeter	20
3. Calibration of the Ground-Penetrometer	21
4. The Effect of Gravity on Ground-Penetrometer Readings	21
5. The Effect of a Vacuum on the Thrust of the Ground-Penetrometer Engine	22
6. The Effect of Surface Irregularities on the Instrument Readings	23
7. Mechanical Properties of the Lunar Soil	25
8. Thermal Characteristics	27
Chapter 2 Photogrammetric Analysis of the Lunar Panoramas	30
1. Construction of Ground Plan of the Luna-13 Landing Site	30
2. Study of Lunar Surface Relief along the Horizon Line	32
3. Stereophotogrammetric Study of the Shape of a Rock	36

Chapter 3 Morphological Features of the Landing Site	41
1. Lunar Pits	42
2. Linear Structures	46
3. Rocks and Nodular Clumps	48
Part III Panoramic Photographs of the Lunar Surface	60
Supplement: Topographical Plan and Diagram of the Landing Site	91

PART I
DESCRIPTION OF EQUIPMENT AND
FLIGHT CONDITIONS

CHAPTER 1

LUNAR PROBE DESIGN AND FLIGHT CONDITIONS

1. THE AUTOMATIC LUNAR PROBE "LUNA-13"

The lunar probes Luna-13 and Luna-9 differ mainly in their complements of scientific equipment. The Luna-13, in addition to transmitting lunar panoramas with television gear similar to that used in Luna-9, also made determinations of the density, firmness and radiation temperature of the lunar soil, using special on-board equipment. The Luna-13 was also equipped with a new thermal regulation system.

/9*

Like the Luna-9, Luna-13 was protected against thermal radiations from the lunar surface and sun by special thermal insulation on its body.

The design of the probe made provision for mechanisms to bring out the instruments from the probe to the lunar surface; these mechanisms ensured placement of the instruments at a sufficient distance from the probe (1.5 meters), smoothly, without shock and without upsetting on an uneven surface.

The brightness standards and the three two-surface mirrors on Luna-9 were not present on Luna-13.

An external view of Luna-13 is shown in Fig. 1.

2. LUNA-13 FLIGHT CONDITIONS

/10

The automatic lunar probe Luna-13 was launched December 21, 1966 at 13h 17m 08s, Moscow time.

The overall arrangement and flight control principles set forth in Volume I for Luna-9 remained substantially unchanged, both in flight to the moon and retardation phases. A total of 24 communication schedules were completed with the Luna-13, of which nine were after the landing on the lunar surface. The sequence of operations carried out by the probe on the Moon's surface is detailed in Table 1.

3. THERMAL REGULATION SYSTEM

The new thermal regulation system consisted of the following elements: a water tank, an exploding valve, a valve-evaporator, a blower and a system of piping.

* Numbers in the margin indicate pagination in the foreign text.

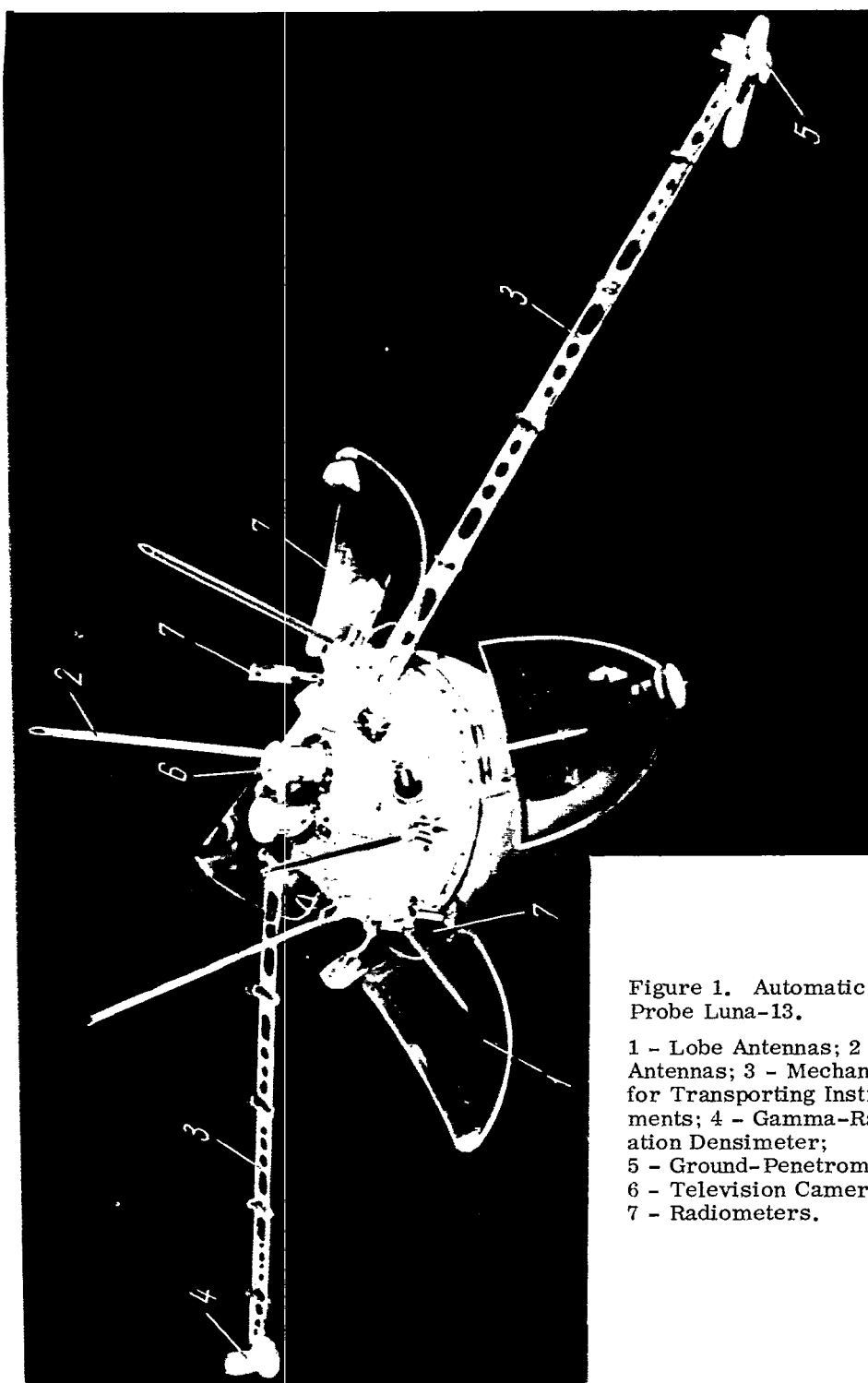


Figure 1. Automatic Lunar Probe Luna-13.

1 - Lobe Antennas; 2 - Rod Antennas; 3 - Mechanism for Transporting Instruments; 4 - Gamma-Radiation Densimeter; 5 - Ground-Penetrometer; 6 - Television Camera; 7 - Radiometers.

TABLE 1.

/11

Se- quence No.	Date and time	Operation	Se- quence No.	Date and time	Operation
1	<u>24 December</u> 21h 01m	Automatic lunar probe Luna-13 made soft landing	5	<u>26 December</u> 16h 00m-- 18h 23m	Transmission of second lunar panorama and telemetry data
2	21h 05m 30s	Reception of first signal from the lunar surface	6	<u>27 December</u> 16h 46m-- 19h 55m	Transmission of third lunar panorama and telemetry data
3	21h 06m 21h 18m	First radio communication period. Reception of telemetry data and instrument calibration	7	20h 30m-- 21h 32m	Second radio communication period. Telemetry data re- ception
4	<u>25 December</u> 15h 15m-- 16h 53m	Period of transmission of televi- sion pictures and telemetry data Switch-on of television equipment of the automatic lunar probe Scanning of lunar landscape and transmission of the first pano- ramic views of the lunar surface to Earth Reception of telemetry data on the condition and operation of the on-board systems, scientific and servicing gear	8	<u>27-28</u> <u>December</u> 23h 02m-- 0h 21m	Transmission of fourth lunar panorama and telemetry data
			9	<u>28 December</u> 0h 41m-- 1h 06m	Third radio communication period
			10	2h 23m-- 2h 48m	Fourth radio communication period
			11	7h 05m-- 9h 13m	Transmission of fifth lunar panorama and telemetry data

After the landing on the Moon the exploding valve was blown open by autonomous command, which turned on the water vaporizing system. The blower was turned on at the same time to expedite heat transfer to the gas.

The main element of the thermal regulation system is the valve-evaporator. It is opened and closed automatically as governed by thermal expansion of the valve body. The valve thus serves three functions: it is a sensing element, the water-feed regulator and the evaporator. Use of this valve made the entire system more reliable since the special automatic devices used in the thermal regulation system of the Luna-9 were not needed.

Water was supplied from the tank to the valve-evaporator by gas pressure in the probe. It is vaporized in the valve and takes up heat from the gas blown through the valve by the blower. The higher the temperature of the valve-vaporizer body, the larger the supply of water and the greater the amount of heat removed.

4. MECHANISMS FOR TRANSPORTING INSTRUMENTS OUTSIDE FOR INVESTIGATIONS OF THE LUNAR SURFACE

The ground-penetrator and the radiation densimeter are installed in the non-hermetic portion of the probe between the upper half-shell of the body and the lobe antennas on mechanisms designed to place the instruments outside the probe for investigations of the lunar surface material (Fig. 2).

The limited space below the lobe antennas on the one hand, and the necessity for placing the instruments as far as possible from the probe on the other, required construction of the mechanisms as folding, multi-link devices permitting extension of the instruments to a distance of 1.5 meters. The mechanisms could thus be made lighter and smaller in size, avoiding high loading when they are developed under lunar conditions. The mechanisms are held in place in the folded state by locks that open when the lobe antennas are deployed. To prevent mutual interference during simultaneous deployment of the lobe and rod antennas, the mechanisms begin to operate after the rod antennas are fully deployed and after the lobe antennas have completed about two-thirds of their travel. Thus the opening of the mechanisms coincides with the process of orienting the probe on the lunar surface by the action of the springs that deploy the lobe antennas. The rapid motion of the lunar probe in the plane perpendicular to the plane of opening of the mechanisms generates a substantial load due to the inertial forces on the deployed mechanisms. Tests were made to examine the effects of this loading on the mechanisms; in the tests the mechanisms and the lobe antennas were opened under lunar gravity conditions and with various initial orientations of the probe. The mechanisms were provided with a system of cables for synchronization purposes to ensure simultaneous and proportionate opening of all links and complete extension of the mechanisms prior to placing them on the surface. /12

Yokes to hold the ground-measuring devices or the radiation densimeter are hinge-mounted at the ends of the terminal links of the mechanisms. The axis of rotation of the instruments relative to the yoke and the axis of fastening of the yoke relative to the mechanism form a Cardan suspension, which permits orientation of the instruments on the lunar surface. /13

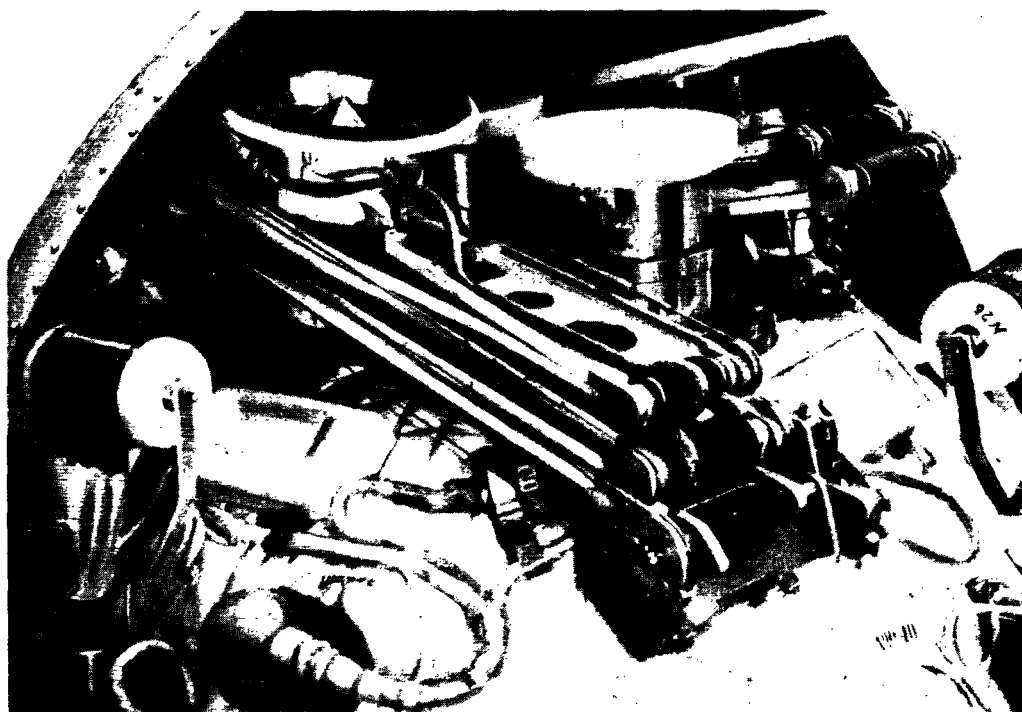


Figure 2. Mechanisms for Transporting the Ground Investigation Instruments outside the Probe. Mechanisms in Folded State.

In many orientations of the probe on the lunar surface the extending mechanisms can fall within the field of view of the telecamera.

In the lunar surface panorama taken on 24 December 1966, the hinge between the first and second links of the mechanism, the terminal link and the sharp shadow of the entire mechanism are visible; this indicates that it opened normally and dropped to the lunar surface in the fully opened state.

SCIENTIFIC INSTRUMENTATION

1. METHODS OF DETERMINING THE MECHANICAL PROPERTIES OF THE LUNAR SOIL

The problem of defining the solidity and density of lunar soils has for many years attracted the attention of scientists and designers of spacecraft.

But until recently all knowledge of the surface layers of the Moon has been acquired by the indirect methods of astronomy or radio-physics.

The first direct information on the firmness of the lunar soil and on its surface structure was obtained from the soft landing of the lunar probe Luna-9. However, this probe was not equipped with special instrumentation for examining the mechanical properties of the ground. The first such equipment was used in Luna-13.

The ground was investigated by the Luna-13 probe using three instruments:

- a radiation densimeter to define the density of the surface layer;
- a ground-penetrometer to establish the mechanical solidity of this layer;
- a dynamograph to estimate the rigidity of the surface layer in terms of the dynamics of the shock at the instant the probe contacted the moon.

The overall aim of the experiments was to categorize the material of the lunar surface layer (rockes, porous mineral mass, granular soil or dust) from the readings of the instruments and to establish to a first approximation its density and mechanical parameters.

/15

In this connection, during the design of the radiation densimeter and the ground-penetrometer, these instruments were repeatedly calibrated on terrestrial soils and simulated materials and the physical properties of these materials were determined by the standard methods of soil mechanics. The calibrations were made under normal atmospheric pressure and in a vacuum, with normal gravitational acceleration $g_e = 9.81 \text{ m/sec}^2$ and in an aircraft flying in a trajectory such that $g_a = 1.63 \text{ m/sec}^2$, with static and dynamic loads on the penetrometer and on materials having smooth and rough surfaces.

The Luna-13 experiments to define the mechanical properties of the soil represent the beginning of a new stage in lunar research, in which for the first time engineering-geological survey instruments were delivered to the lunar surface.

2. GROUND-PENETROMETER

The ground-penetrometer is designed to estimate the mechanical strength of the upper layer of the lunar soil. It consists (Fig. 3) of a plastic body whose

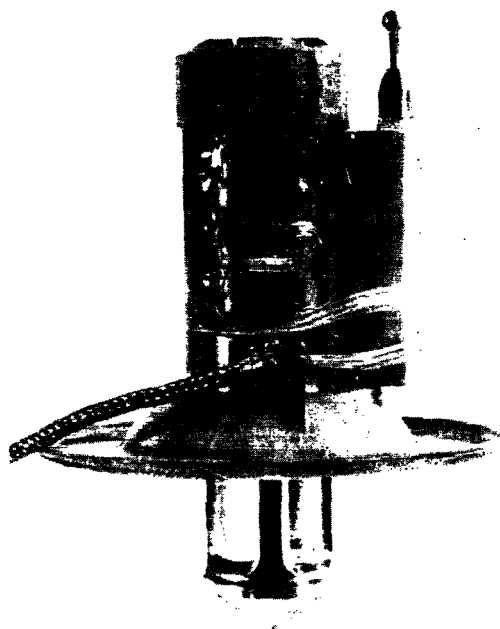


Figure 3. Ground-penetrometer.

lower portion forms a circular punch with an outside diameter of 12 cm and an inside diameter of 7.15 cm, and an indenter with a conical lower section. The body is made of fiberglass, the indenter is of titanium. The point angle of the indenter body is 103° ; the maximum diameter of the cone is 3.5 cm. The indenter can be extended 5 cm beyond the body.

A sliding-contact potentiometer is mounted on the body of the device. The sliding contact is tied to the extensible indenter. Thus the potentiometer arm ratio changes as the indenter travels and the voltage at the output terminals of the potentiometer is changed.

The indenter body also houses a solid-fuel engine with a nozzle directed upward. Directly behind the nozzle section is an electric-pyrotechnic device for starting the engine which is jettisoned by the pressure of the hot gases after the

engine has operated. The firing command is given after the lobe antennas of the probe are deployed and the instruments have been lowered to the surface of the Moon. The instrument is first interrogated via the telemetry system to obtain its zero reading.

After the instrument has been lowered to the surface and the engine has operated, an estimate of the mechanical properties of the ground is made according to the depth of penetration of the indenter, or in loss and dusty soils also according to the depth of penetration of the circular punch of the body of the instrument.

When the engine is started the body cover and the starting device are jettisoned. This breaks the electrical circuit of the starting device, the ball-bearing detent securing the indenter to the body of the instrument is freed and the indenter can move downward freely to a distance up to 5 cm under the action of the engine thrust.

The depth of penetration is registered by the potentiometer. The engine operated for 0.6-1.0 seconds, the average thrust under terrestrial conditions is 5-7 kg and 25-37 mm Hg (5.5-7.5 kg) in vacuo. The indenter displacement is measured to an accuracy of about 0.3 mm.

As tests have shown, the indenter penetrates very rapidly into dry and solid porous materials (0.003-0.05 sec) and with continued engine operation no increase in penetration is noted. In compact material, on the other hand, the penetration process continues for more than 0.5 sec, although even in this case the major portion of the deformation takes place at the very beginning

The indenter remains in the position it has reached at the instant of engine cutoff. The next interrogation of the instrument via the telemetry system immediately establishes its depth of penetration, and subsequent interrogations allow following the temporal changes in this quantity. /17

In very friable and dust-like soils the indenter penetrates to its limiting depth of 5 cm, at which time its flange, which is connected to the potentiometer slide, rests on the end section of the body and begins to transmit to it the load from the still operating engine. As a result the circular punch serving as the lower portion of the body begins to penetrate into the ground.

The depth of this penetration may be judged from the televised picture if the instrument falls within the field of view of the camera. It is not observed in compact-porous, frothy and compact granular soils.

It was taken into consideration when selecting the dimensions of the indenter cone that the largest grain size of the soil is measured in millimeters. Special tests established that minimum dispersion in the experimental data for such soils occurred with a cone diameter of 30-40 mm. The cone angle was initially chosen to be 150° , but was later decreased to 103° to improve the measuring accuracy when operating in compact-porous materials.

Based on the requirement for examining a broad range of soils and rock species, the penetrometer force was computed so that its cone would penetrate substantially into the most dry and porous species that might be expected on the lunar surface.

3. RADIATION DENSIMETER

The radiation densimeter is designed to establish the density of an upper layer of the lunar surface of average thickness up to 15 cm. It consists of a pickup fastened to the extender mechanism and placed directly on the surface, and an electronic unit that processes the information from the pickup and transmits it via the telemetry system. The electronics unit is located in the hermetically-sealed body of the probe.

Figure 4 shows a photograph of the pickup; its image, transmitted from the Moon, is shown in Fig. 5.

The pickup of the radiation densimeter consists of an elongated flat body, dimensions 25.8 x 4.8 cm by 1 cm high, with two lateral segments to provide stability on an uneven surface. The body has a superstructure that serves to connect the pickup to the extender mechanism. The radioactive isotope (Cs^{137} , activity equivalent to 1 mg of radium), a lead screen and three sets of counters (SBM-10M) to record the scattered gamma radiation are installed inside the body. /18

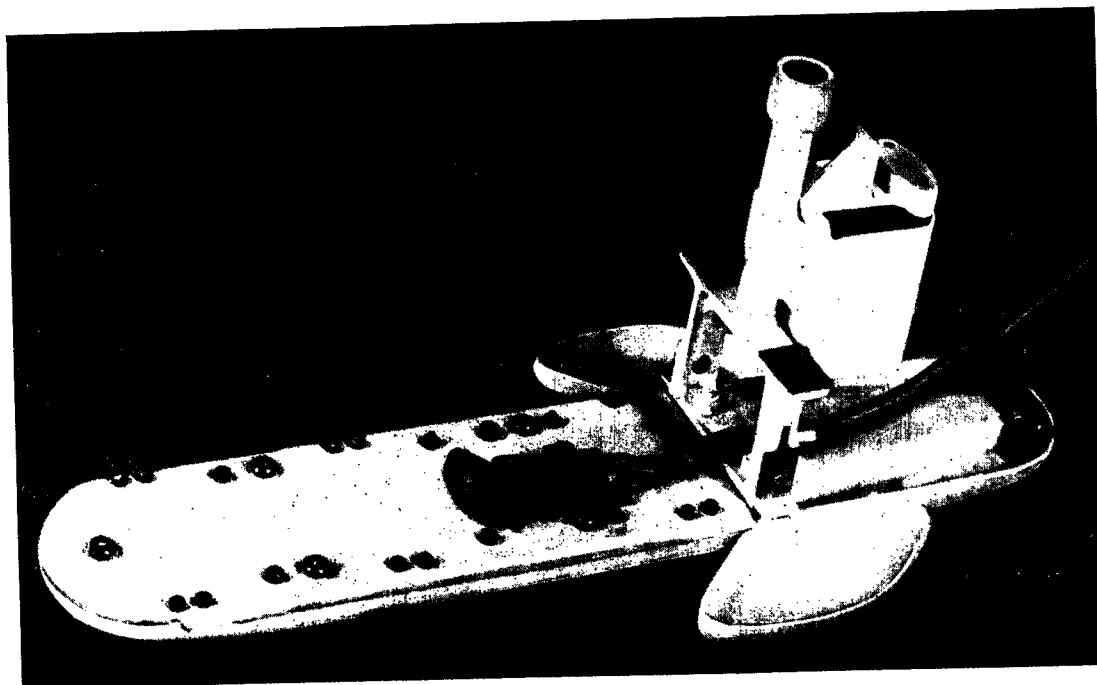


Figure 4. Radiation Densimeter.



Figure 5. Television Picture of the Radiation Densimeter Transmitted from the Moon.

A cable to the pickup supplies the counter anodes and the associated electronics.

The principle of operation of the radiation densimeter is as follows: Gamma quanta radiated by the isotope penetrate the ground beneath the surface on which the pickup is located. Some portion of the gamma radiation is absorbed by the ground due to scattering and absorption, and another portion is returned to the surface and may be recorded by the counters.

The lead screens mentioned above are placed between the isotope and the counters to prevent gamma radiation from by-passing the ground and reaching the counters directly.

The electronics consist of three separate channels associated with the three groups of counters. The number of pulses arriving from the counters are summed for each of the three groups over the two-minute intervals between the sequential interrogations of the telemetry system. /20

4. DYNAMOGRAPH

The dynamograph is designed to investigate the dynamics of the collision between Luna-13 and the lunar surface during the landing. It records the duration and magnitude of the dynamic load and consists of a system of three mutually-perpendicular accelerometers. The dynamograph is mounted on the instrument rack in the probe. The accelerometer signals are fed to an integration and storage unit, from which the information is telemetered to Earth.

5. RADIOMETER

The radiometer measured the thermal radiation of the lunar surface. The instrument has four identical pickups, located so that no matter what the position of the probe relative to the sun the field of view of at least one of them would not be the shadow of the probe or the sky and its entrance aperture would not be illuminated by solar rays. Photographs and a diagram of the pickups are given in Figs. 6 and 7.

The field of view of a pickup is limited by a conical mirror having an opening angle of 28° . The mirror is a truncated, internally-polished metal cone, 60 mm in height, with a diameter of the narrow portion of 15 mm. The narrow end of the cone is attached to a rectangular chamber containing the radiation pickup. Both the pickup chamber and the conical mirror are thermally insulated externally by twenty layers of vacuum-shield insulation.

The pickups were located outside and held in place by hinged brackets that were not thermally insulated. During flight the brackets were folded up and the pickups were located in the space between the shell of the probe and the lobe antennas. The brackets were unfolded when the antennas were deployed and the pickups assumed their normal positions.

The receiver consisted of a thin plate, 15 x 20 mm in size, with a thin metal spiral cemented to it; the electrical resistance of the spiral is a measure of the /21

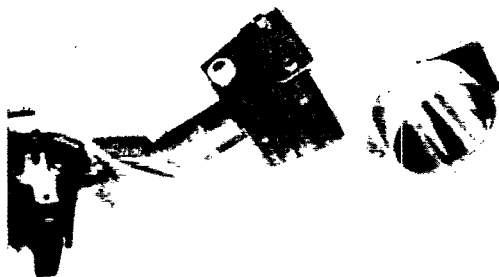


Figure 6. Photograph of the Radiometer Pickup.

temperature. The receiver was coated with a red enamel that is a good absorber of infrared radiation (from 75-85%, as a function of wavelength) and which reflected up to 80% of the visible light.

The receiver is not in contact with the body of the pickup and is well-insulated from it by the vacuum-shield insulation. As a result the pickup has two time constants; several minutes for changes in temperature of the pickup itself and several hours for changes in temperature of the inside walls of the pickup chamber, with which the receiver exchanges heat by radiation.

The pickup was calibrated with the radiation from a simulated black body with an emissivity $\epsilon \approx 0.997$. During the calibration the pickup was enclosed in a vacuum chamber with the same brackets used in the probe. The chamber pressure during calibration was about 10^{-4} mm Hg.

Figure 8 shows a projection of the disposition of the pickups on the panorama plane — i.e. the plane perpendicular to the axis around which the lunar landscape is scanned. The axes of the sensitive elements were inclined 30° below the panorama plane.

The diameter of the field of view of each sensor was about 70° . The fields of view of the sensors are delineated by the white lines on the panorama (Fig. 9). Against the sky background these lines are circular arcs with a diameter equivalent to the angular dimension of the field of view at infinity. The regions lying within the field of view of the sensors on the lunar surface are indicated by the compound curves, whose configurations are determined by the difference in the distances of surface elements from the sensors and from the pupil of the TV camera. The spot in the upper left-hand corner of the panorama

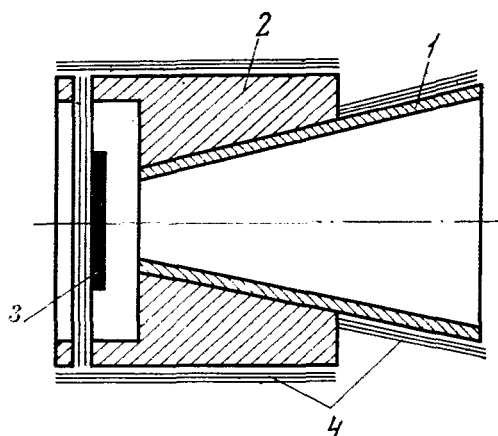


Figure 7. Diagram of Radiometer Pickup.

1 - Conical Mirror; 2 - Thermal Insulation of Foam Plastic; 3 - Radiation Receiver; 4 - Vacuum-Shield Insulation.

at an angle $\gamma \approx 100^\circ$ is the image of the sun, and the bright spots in the region $\gamma = 105 - 140^\circ$ are solar reflections from parts of the probe.

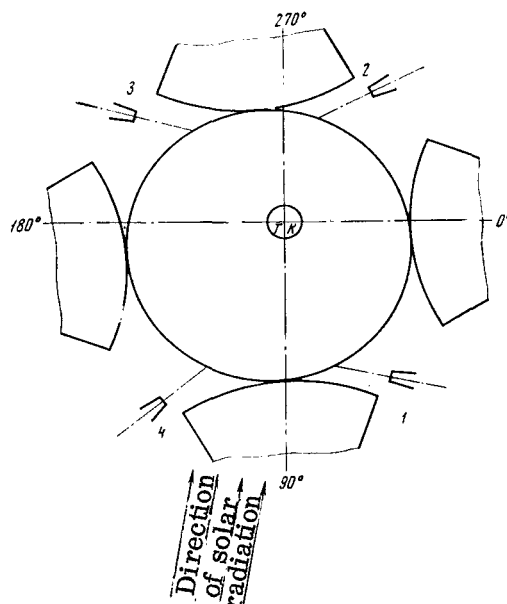


Figure 8. Diagram of the Arrangement of the Radiometer Pickups.

1, 2, 3, 4 - Pickup Number; Longitudes in the Panorama Plane are Indicated. The Parallel Arrows Show the Projection of the Sun's Rays onto the Plane of the Panorama. The Small Circle Labelled TK Indicates the Location of the TV Camera.

At low solar altitudes above the lunar horizon a part of the inside surface of the conical mirrors of sensors 1 and 5 (Fig. 8), which are directed toward the sun, is directly illuminated by the sun. The cones of elements 2 and 3 were not directly illuminated by the sun, but a portion of their fields of view is taken up by the shadow of the probe.

A portion of the field of view of elements 1, 2 and 4 were taken up by sky. Thus the indications of sensor 3 are the most useful for interpretive purposes.

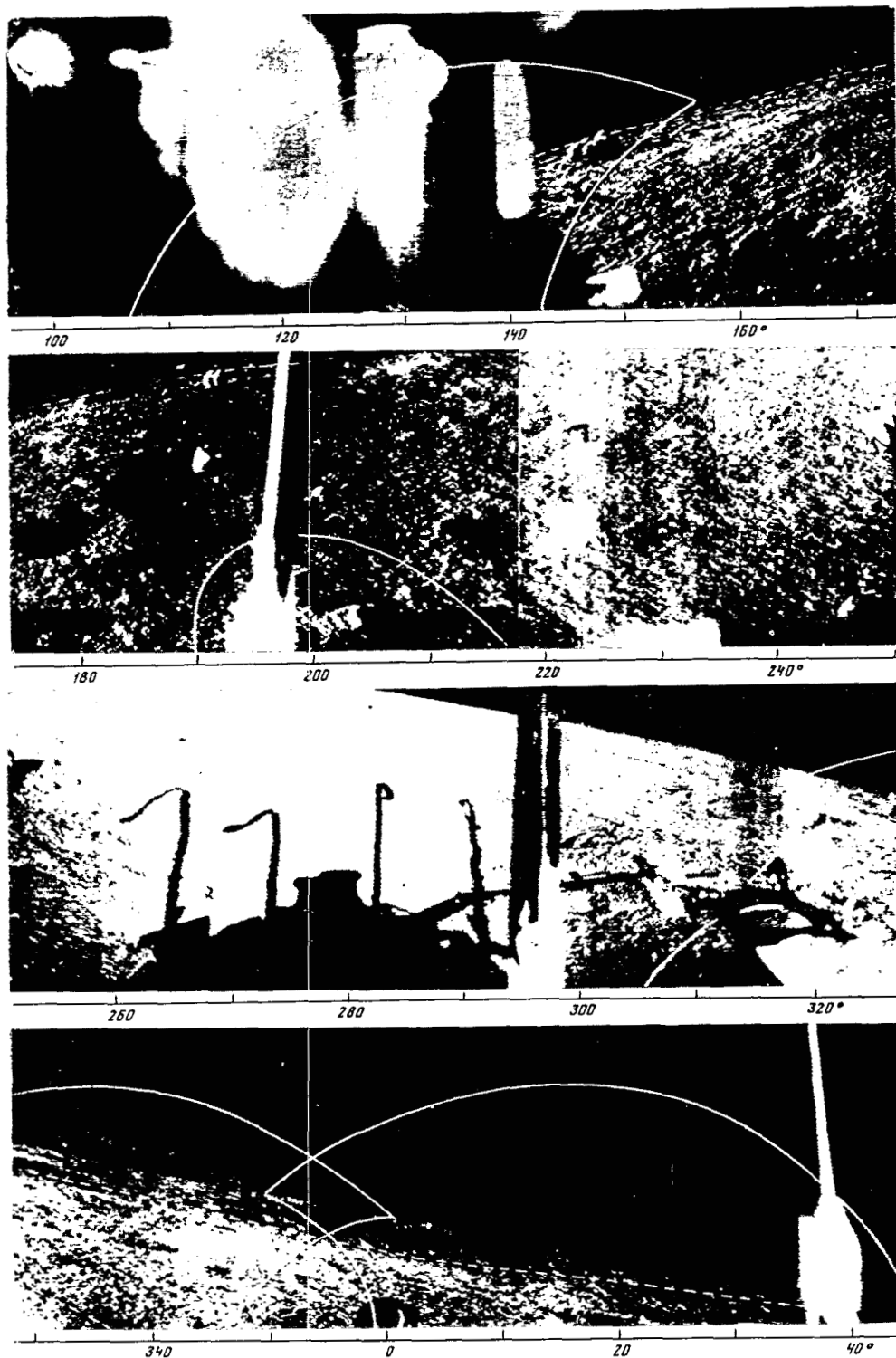


Figure 9. Limits of the Fields of View of the Radiation Pickups (Solid Lines) and the Edge Contours (Broken Line).

/23

PART II

/24

RESULTS OF THE SCIENTIFIC INVESTIGATIONS

INVESTIGATIONS OF THE PROPERTIES OF
THE LUNAR SOIL

1. SIMULATED MATERIALS

A great many conflicting hypotheses have been advanced as to the nature of the surface layer — such as, for example, a covering of lava, layers of detritus, granular material and slag, a loose dust cover and complex dendritic structures. The acquisition of data on the density and solidity of lunar soils by the direct methods in general use in terrestrial engineering-geological surveys is of great import and permits comparing the mechanical characteristics of lunar and terrestrial soils.

The ground calibration of the instruments carried by Luna-13 required the selection and preparation of materials having mechanical properties and densities corresponding to those expected for the surface layer of the Moon.

Until recently the composition of synthetic materials and the laboratory study of their properties has in general been oriented toward reproducing the optical, thermal and electrical properties of the lunar surface. Volcanic materials and powders prepared from them were given first consideration and tests were run on them to obtain a preliminary definition of their mechanical properties in a high vacuum and with a six-fold reduction in gravitational force. In addition, pulverized tufa, slag and pumice have been used in a NASA program (U.S.A.) in the construction of a "Moondrome" for testing space devices.

The published data on the assumed physico-mechanical properties of the lunar surface layer are contradictory and did not permit choosing any one material as a universal analog for use in instrument calibration. Therefore the decision was made to examine various materials covering the extreme values of density and mechanical properties assumed for lunar soils. As regards structure, materials were selected from friable and loose-granular to compact-porous and stone-like materials.

/26

Since the data available to date points to a low-density for the surface layers of the Moon, friable and porous materials of low specific weight (Figs. 10, 11) predominated among the materials tested.

A total of fourteen materials was studied. The physico-mechanical parameters of some of them, typical of the basic groups, are given in Table 2.

Prime consideration was given to materials of mineral composition, both those of natural origin and those prepared artificially.

Apart from the materials listed in the table, which were used primarily in the calibration of the ground-penetrometer, eight other materials related to a number of light and heavy cements were used specifically for calibration of the radiation densimeter. The volumetric weight of these materials ranged from 0.50-2.26 g/cm³.

/27



Figure 10. Sample of Porous Basaltic Lava.

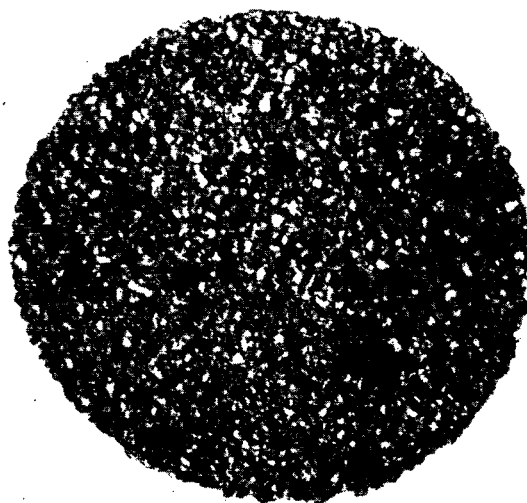


Figure 11. Sample of an Unbound Porous Agglomerate (Agloporite).

A dry silica sand of average grain size in loose ($\gamma = 1.52 \text{ g/cm}^3$) and compact ($\gamma = 1.8 \text{ g/cm}^3$) states and a soft porolated mat ($\gamma = 0.04 \text{ g/cm}^3$), whose compressibility was 1000 times greater than that of the compact sand, were used to calibrate the dynamograph.

TABLE 2. Physico-Mechanical Properties of Some Simulated Materials

Materials	Volumetric weight (g/cm ³)	Porosity (%)	Moisture content (%)	Equivalent cohesion according to N. A. Tsytovich (kg/cm ²)	Limiting strength in compression (kg/cm ²)
<u>Solid</u>					
Vesicular andesite-basaltic lava	1.95	35	0.91	210.0	> 100.0 16.25 17.86
Foamy cement	0.60	79	2.80	8.6	
Foam glass	0.24	89	0.20	3.5	
Materials	Volumetric weight (g/cm ³)	Porosity (%)	Moisture content (%)	Cohesion (kg/cm ²)	Angle of internal friction (deg.)
<u>Granular</u>					
Quartz sand	1.52	44	0.20	0.060	30
Agloporite	0.77	69	0.20	0.010	32
Fine porous clay	0.75	73	0.38	0.010	36
Crushed foamy cement	0.35	87	2.80	0.019	30
Inflated perlite sand .	0.16	—	2.10	0.004	23

2. CALIBRATION OF RADIATION DENSIMETER

Three interaction processes take place between the gamma quanta and the material in the measurement of ground density: the photo-effect, electron-positron pair formation and the Compton effect. In the photoelectric effect and pair-formation, which are absorption processes, the gamma-quanta disappear completely. On the other hand, in the Compton effect the gamma quanta are scattered by electrons in the material, which results in a partial loss of energy by a gamma quanta and a change in its direction of motion. The optimum gamma energy range for measuring the density of matter using the gamma-method lies between 0.5-3.0 Mev. The Compton effect predominates in this range; its cross-section is proportional to the ratio Z/A (Z = atomic number). For most of the elements found in rocks and soils (apart from hydrogen) this ratio changes but little, which thus ensures that the results will not depend on the chemical composition of the soil. /28

The relationship between recorded gamma intensity and soil density for the instrument described above is presented in curve form, as in Fig. 12, with the maximum centrally located. The position of the maximum and its absolute value depend on the datum of the instrument — that is, the distance between the isotope and the center of the counter unit, the source energy and the pickup design. This curve trend results from the concurrence of two parallel processes: scattering and gamma absorption.

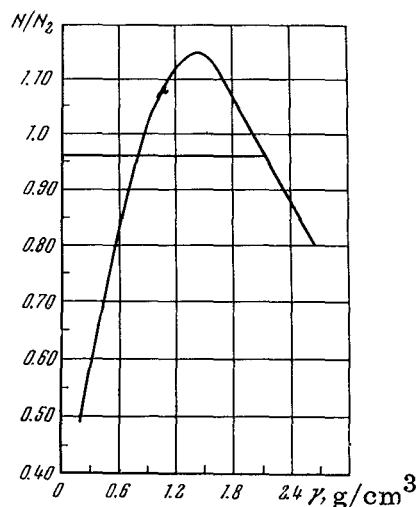


Figure 12. Calibration Curve of the Radiation Densimeter.

The probability of the Compton effect is proportional to the number of electrons per unit volume, i. e. to the density of the substance. Therefore the scattering intensity must increase with increased density, which is seen in the left-hand portion of the curve at low densities. However, as the density increases the gamma energy decreases as a result of multiple-scattering and the probability of absorption due to the photo-effect increases. Absorption gradually comes to predominate and with a further increase in density the intensity of the scattered radiation falls off, as seen in the right-hand portion of the curve.

It is inconvenient to construct the curve analytically and in practice calibration methods are used in which the scattered radiation is measured for substances of differing densities. Blocks of light and heavy cement (70 x 70 x 70 cm) and tanks (60 cm diameter, 60 cm high) filled with

granular materials were used to calibrate the radiation densimeter. The basic calibration tests were made by placing the pickup of the instrument on a

/29

carefully leveled surface of the material, and supplementary tests were made on a rough surface.

The curve of Fig. 12 was derived from these basic tests. The curve was plotted from the averages of the intensities of the scattered radiation recorded by all three sets of counters. The most important branch of the curve is the left-hand ascending branch, which corresponds to materials with densities from 0.1 to 1.5 g/cm³ (in terrestrial units). The descending branch relates to materials having densities from 1.5-2.6 g/cm³, whose presence on the Moon is considered to be of low probability. Values of density γ are plotted on the abscissa of the graph of Fig. 12, the intensity of the scattered radiation in relative units is plotted on the ordinate. Each relative unit is equal to the number of pulses recorded in 2 minutes with a material of density 2.0 g/cm³.

3. CALIBRATION OF THE GROUND-PENETROMETER

The main calibration tests were made under normal terrestrial conditions. The granular and dust-like materials were loaded into metal tanks (dia. 60 cm, height 60 cm) without packing. Solid materials were tested in block form, with the block dimensions being several times larger than the diameter of the cone of the instrument. In repeated parallel tests the instrument was loaded by a rocket engine and by weights to establish the static equivalent.

In all tests the surface of the material was carefully leveled and the tanks or samples were rigidly secured to a heavy steel plate. The depths to which the cone penetrated were established from a calibration curve plotted from an oscillogram of the voltage changes at the potentiometer output and by parallel direct measurements with a sliding caliper to within 0.01 cm. The depth the body of the instrument sank into friable and uncompacted loose materials were measured with a precision level or a steel rule to within 0.05 cm.

The test results for all materials investigated were subdivided into five groups, characterized by sharply divergent properties, and are shown in Table 3.

4. THE EFFECT OF GRAVITY ON GROUND-PENETROMETER READINGS

/30

The limiting resistance of a granular soil to depression is determined by inter-grain friction, which depends on the grain weight and therefore on gravity, and on inter-grain cohesion, which is determined by molecular forces and does not depend on gravity.

Actual soils, both terrestrial and lunar, possess both friction and inter-grain cohesion. On Earth the cohesive forces stem from the interaction of the water-colloidal envelopes of clay particles, but in dry soils the cohesive forces are attributable to direct molecular interaction between the clean mineral surfaces at the points of contact of the particles. Therefore, on going from terrestrial to lunar gravity, the limiting resistance to indentation of real soils will decrease, and the decrease will be larger the greater their friction and the lower the cohesion between grains.

TABLE 3. Results of Calibration Tests of the Ground-Penetrometer under Terrestrial Conditions

Depth of penetration (cm)		Volumetric weight (g/cm ³)	Simulated material
Indenter	Body		
0	0	2.4 — 3.0	Solid and compact rock species Heavy cement
0.0 — 1.3	0	0.25 — 2.0	Frothy and porous rock types associated with soils. Foamy cement and foam glass, porous clay filler in organic binding
1.3 — 5.0	0	1.3 — 1.7	Unbound granular soils of average density. Quartz sand
1.3 — 5.0	0 — 1.0	0.25 — 0.77	Unbound granular soils of low density. Crushed foamy-cement, porous clay filler and agloporite
5.0	> 1.0	≤ 0.16	Especially friable and dust-like soils. Expanded perlite sand

The existing findings of soil mechanics enable us to compute the load-bearing capacity of a soil—i. e. the maximum specific pressure underneath a loaded area which, if slightly exceeded, may result in a sudden and deep-seated collapse. However, it is not yet possible to compute accurately the depth to which the loaded area will collapse under such conditions, or to define accurately the relationship between the depth of impression and the gravitational force. The experimental data relevant to this question are scanty and contradictory, although they indicate generally that the effect of gravity is exhibited weakly in cohesive soils and considerably more strongly in unbound and friable soils.

/31

In this connection, special tests were made while calibrating the ground-penetrometer to clarify the effect of gravity on the depth of penetration of the conical indenter in quartz sand and in fine clay-filled gravels (unbound soils). The tests were made in devices in which load was applied to the indenter by a long spiral spring, and the depth of penetration was recorded by a mechanical recorder. The instruments were installed in an aircraft which flew in flight paths such that over a certain time span the gravitational force was reduced to that of the Moon, and the depression tests were made during these times. Parallel tests were made on the ground using the same equipment.

The tests established that under the conditions of lunar gravity the indenter of the ground-penetrometer could penetrate 1.7 times deeper into the specified soils than it could under terrestrial conditions.

5. THE EFFECT OF A VACUUM ON THE THRUST OF THE GROUND-PENETROMETER ENGINE

The thrust of the reaction angle of the ground-penetrometer depends on the atmospheric pressure and increases as the pressure decreases. To make this

relationship more precise, special tests were run in a large vacuum chamber which was held at about 25-37 mm Hg.

The tests indicated that engine thrust increased by 8.5% and, under these conditions, amounted to 6.5 kg on the average, with essentially unchanged duration of engine operation.

6. THE EFFECT OF SURFACE IRREGULARITIES ON THE INSTRUMENT READINGS

/32

Surface irregularities effect the readings of the ground-penetrometer and radiation densimeter in two ways. First, the instrument strikes large holes or rocks it may be slowed sufficiently to prohibit obtaining useful data. If this does not occur the presence of small-scale irregularities may lead to some dispersion in the results.

The Luna-9 panoramas were analyzed to estimate the overall probability of carrying out a successful experiment in view of the actual roughness of the lunar surface. The horizontal plan and the data on the sizes and number of rocks and small craters observed in the panorama given in Vol. I of this work were essential for this purpose.

Let us first consider the effect of irregularities on the operation of the ground-penetrometer.

If the instrument falls on a large stone its circular punch will not reach the surface and a gap will exist, depending on the height of the stone. When the engine starts the indenter cone will begin to penetrate the stone. If the stone is hard the penetration will be slight, the ring punch also will not touch the surface and the potentiometer will not register motion of the indenter relative to the body of the instrument. If the stone is soft and small the penetration of the indenter may be so deep that the ring punch contacts the surface of the ground alongside the stone, but only the latter stage of the penetration process will be recorded by the potentiometer. Thus if a stone is encountered the true solidity of the material will be overstated.

If a deep hole is encountered the indenter first traverses the gap between the tip of the cone and the bottom of the hole without resistance and only then penetrates the ground. In this case the potentiometer exaggerates the depth of penetration and the solidity of the material is underestimated.

If the instrument rests on the ground in a skewed position, for example if one edge rests on a stone and the other on the flat surface, or if one edge is in a hole and the other on its edge, a gap exists underneath the indenter cone and the solidity of the material is again overstated.

Inasmuch as impinging directly on a stone without being skewed must be considered to be highly unlikely, in most cases large-scale irregularity will lead to underestimating the solidity of the soil. To assess the probability of obtaining useful data under these conditions it is useful to introduce the concept of an "area defect" which, if encountered, results in gross scatter of the data

/33

and rejection of the experiment. The area defect around a large stone or hole will be equal to the area of their horizontal projections plus an annular area around them whose width is equal to the radius of the instrument, i.e. 6 cm. The diameter of the area defect will be

$$D_{\text{def}} = D + 12 \text{ cm}$$

where D is the diameter of the stone or hole.

Based on the Luna-9 survey data (and doubling the number of stones) it was computed that in the fifty square meters included in the survey the areal defect was 5.02 m² around 150 stones, 4.74 m² around 88 holes, for a total of 9.76 m², or 20% of the total area. In addition, the intervals between area defects were rolling, and analysis of profiles plotted from the plan contours showed discontinuities that could be interpreted as small protuberances or depressions. These also tend to produce abnormal operation of the instrument. If the maximum allowable error is taken to be 1.2 cm (since with a large error it becomes difficult to distinguish between compact and granular materials or between granular and loose materials from the penetrometer indications) the fractional area defect must be further increased by 10%. On the basis of the Luna-9 data the probability of obtaining useful information could be taken as 70%. It may possibly be somewhat larger in the area of the Luna-13 landing since the surface relief at this site is smoother.

Let us now turn to the radiation densimeter. Gross irregularities should affect its operation in about the same way as the ground-penetrometer, since the areas on which they rest are much the same for these two instruments.

The effect of small surface irregularities on the indication of the radiation densimeter is somewhat more involved. Imperfect contact of the body of the device and the presence of cavities in the surface layer show up differently in the instrument's readings when operating in light and heavy materials.

In dense soils, corresponding to the right-hand descending portion of the curve of Fig. 12, looseness or cavities lead to an increase in the integral counting rate. With materials of very low density (up to 0.4 g/cm³), on the other hand, the counting rate decreases. For other materials there are inversion points that are helpful in eliminating the influence of the contact conditions on the results.

Tests made with materials having densities of the order of 0.75 g/cm³ have shown that local depressions 3-4 cm in diameter and 2-3 cm deep, located directly beneath the base of the pickup, change the count rate by 5-10%, depending on the positions of the depressions relative to the counter group. In this case an intensity decrease is noted for counters with a small base and an intensity increase for counters with the largest base. If the pickup is placed on protuberances of equal height, the counting rate for maximum base increases by 15-20% and decreases by the same amount for minimum base. An inversion point occurs with irregularities of about 3 cm.

/34

Thus the sense of the effect of an imperfect contact is opposed for the different groups of counters, and averaging the results over the three groups of counters should therefore considerably decrease the effect of roughness on the final result. Based on this consideration the data from the radiation densimeter is most conveniently analyzed by plotting curves of the averaged data.

It is clear from Fig. 5 that the radiation densimeter pickup was lying on a comparatively smooth area of the surface. The micro-inhomogeneities were smoothed out and the pickup was slightly skewed to the left from the point of initial contact. It is apparent that a sufficiently firm contact exists between the ground and the base of the instrument.

7. MECHANICAL PROPERTIES OF THE LUNAR SOIL

The data obtained from all instruments were complementary. Therefore their readings were interpreted jointly and the results of all three instruments were used in reaching final conclusions regarding the nature of the upper layer of the lunar soil.

The calibration curve of Fig. 12 was used to reduce the penetrometer readings. Analysis of the telemetry data showed that the indenter was in the initial (zero) position during flight and prior to commanding operation of the engine. After operation of the engine on 24 December 1966, at 21h 06m it had been moved by 4.5 cm. Subsequent interrogation of the telemetry system verified that the position of the indenter had not changed at 16h 15m on 25 December and on 26 December, at 16h 01m, it was 4.25 cm. Then, until the operation of the probe was ended, it varied between 4.17-4.33 cm.

/35

If the instrument fell on a smooth area the indenter penetration into the ground is 4.5 cm. The subsequent decrease by 0.17-0.33 cm is most probably connected with thermal deformations of the supporting mechanism causing changes in the horizontal position of the instrument which resulted in vertical displacements of the cone.

The penetration of the indenter to 4.5 cm, less than its full free travel of 5 cm, is evidence that the detent of the indenter did not contact the body of the instrument and the engine load was not transmitted to the body and consequently the body itself did not penetrate into the ground.

To make use of the data of the calibration tests under terrestrial conditions the measured depth of penetration must be reduced to terrestrial conditions. To do this a preliminary determination is made from Table 3 of the type material corresponding to that tested on the Moon. It is obviously not a compact rocky type nor even a compact porous material such as foamy cement or foam-glass, since the depth of penetration is too great. Nor can it be a loose, dust-like material since the indenter would then have penetrated more than 5 cm and the operation would have included the body of the instrument, which was not observed. It therefore becomes a question of a granular material.

The penetration of the indenter into a granular material depends on the engine thrust and on the gravitational force. Tests made in vacuo and aboard

aircraft with lunar gravity have shown that the depth of penetration under lunar conditions should be $\sim 70\%$ greater than on Earth due to the decreased gravitational force, while the engine thrust is about 8.5% greater than under terrestrial conditions. Thus, under terrestrial conditions the depth of penetration of the indenter should be about

$$S_{\text{earth}} \approx 0.58 S_{\text{moon}}$$

or

$$S_{\text{earth}} \approx 0.58 \times 4.5 = 2.6 \text{ cm.}$$

This corresponds to operation of the device in a compact granular soil or in a loose granular soil with low grain density but with some cohesion between grains. In actual experiments with loose, clayey gravels with a volumetric weight of 0.75 g/cm^3 , the average indenter penetration depth was 5.0 cm and the body of the instrument penetrated an additional 0.8 cm. In experiments with this same material, with the grains held together by an organic binder, the average depth of penetration amounted to 0.88 cm. In loose quartz sand with a volumetric weight of 1.52 g/cm^3 the average penetration depth was 3.7 cm. It is clear that the depth of 2.6 cm can be obtained either with heavy, loose quartz sand or with a weakly-adhering light material of the porous-clay or agloporite types.

The telemetry data from the first communication period, immediately after the lunar landing and lobe opening, were used to interpret the readings of the radiation densimeter. The average overall intensity of the scattered radiation, taking the lunar background into account, turned out to be 0.95 nominal units. According to the calibration curve (Fig. 12) this corresponds to a material density of $\gamma = 0.8 \text{ g/cm}^3$ on the left-hand branch and $\gamma = 2.1 \text{ g/cm}^3$ on the right-hand branch of the curve.

The first value corresponds to a loose granular soil or a highly-porous material of the foamy-cement type; the second value corresponds to a compact stony soil or cement. Since the existence on the lunar surface of compact stony varieties is not in accord with current astronomical, radio-physical or photographic data, the result $\gamma = 2.1 \text{ g/cm}^3$ must be discarded and the value $\gamma = 0.8 \text{ g/cm}^3$ accepted as the more probable. The possibility of a surface strata of a compact porous material for which $\gamma = 0.8 \text{ g/cm}^3$ is not ruled out, but the depth of penetration of the indenter is too great for this material. Therefore the presence of a weakly-cohering granular material with a volumetric weight of $\gamma \approx 0.8 \text{ g/cm}^3$ must be taken as most probable. Taking an average value for the angle of internal friction of $\varphi = 32^\circ$ and using the methods of soil mechanics, the cohesion between grains can be approximated; this turned out to be 0.005 kg/cm^2 . These values of φ and C occur on Earth for slightly-moist sands that are weakly cohesive.

The thickness of the layer examined is defined by the depth of transparency of the soil to the radiation densimeter and was about 15 cm.

Summing up the above data it can be concluded that the surface at the Luna-13 landing site is apparently a layer of granular material with a volumetric weight $\gamma = 0.8 \text{ g/cm}^3$ or somewhat less, consisting of grains and granules of a porous mineral substance that cohere weakly at the points of contact. The angle of internal friction is $\sim 32^\circ$ and the cohesion is of the order of 0.005 kg/cm^2 .

The Luna-13 experiment established that the reliability of the instrumentation is adequate and that the data acquired were in agreement with the analyses of the photo-panoramas and the results of other investigative techniques. It represents the first successful experimental determination of the probable solidity and density of the upper layer of the lunar soil, which is directly subjected to the action of vehicles making lunar landings, lunar transport facilities and which serves as the surface on which cosmonauts move about. The instruments aboard the Luna-13 furnished specific values of the parameters that characterize the properties of this layer which can be used in setting up a computational model of the lunar ground. In addition it has been possible to narrow down considerably the scope of earlier conceptions regarding the properties of the lunar surface and to obtain data of great scientific and practical significance.

8. THERMAL CHARACTERISTICS

The first transmission of readings of the radiometer sensor began 4 minutes after the soft landing of the Luna-13, at 21h 06m, Moscow time, 24 December 1966.

This period lasted 12 minutes, during which time the sensor readings were transmitted several times. The results are shown in Fig. 13. They show systematic temperature decreases that differ for the individual sensors. This circumstance stems from a change in the radiation balance of the sensor elements after the lobe antennas are deployed. The temperatures are in agreement only for sensors 2 and 4. The straight lines approximating the sensor temperatures as functions of the time intersect at a point that corresponds to the instant of landing of the probe ($294^\circ\text{K} = 21^\circ\text{C}$), the temperature of the sensors prior to landing, while they were underneath the folded-up lobe antennas.

/38

The sun rose some hours after the probe landed and its altitude h_\odot above the lunar horizon increased to 38° during the time of observation. Figure 14 shows the h_\odot - dependence of the radiation temperature measured by the sensors. The observed initial decrease in the temperatures of sensors 2 and 3 later changed to an increase due to the heating of the lunar surface. The minimum temperatures were observed at $h_\odot = 6^\circ$, where they were below the values that could be recorded by the probe's equipment. The sharp rise in the curves of Fig. 14 for sensors 1 and 4 are small values of h_\odot is attributable to direct solar illumination. Figure 15 shows the h_\odot - dependence of the ratio T/T_{theor} , where T is the measured radiation temperature and $T_{\text{theor}} = T_\odot (\sin h_\odot)^{1/4}$, i. e. the observed temperatures of a flat surface in radiative equilibrium with the solar radiation. The ratio T/T_{theor} of sensors 2 and 3 is almost constant, but for sensor 2 it is

/39

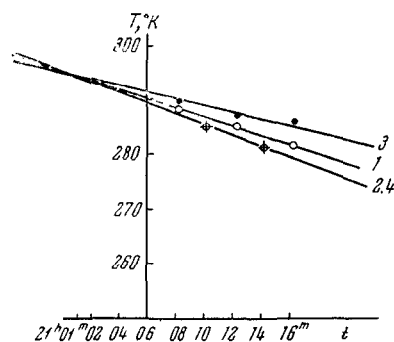


Figure 13. Temperature Changes Measured by the Radiation Pickups in the First Minutes after Landing.

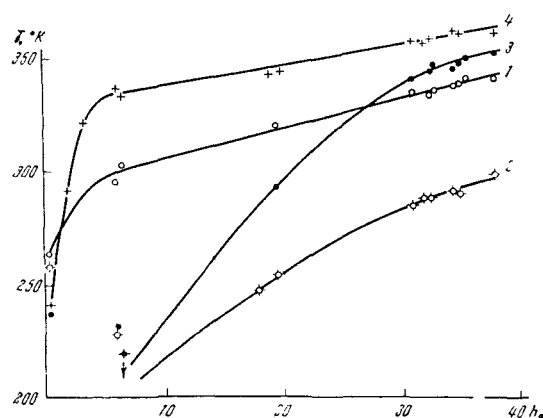


Figure 14. Dependence of the Temperatures Measured by the Radiation Pickups on the Sun's Altitude above the Lunar Horizon.

16% lower due to a partial shadowing of its field of view by the shadow of the probe and the lunar sky in the field of view. Assuming a ratio $T/T_{\text{theor}} = 1$ for sensor 3 and taking into account that the portion of the surface in the field of view is inclined toward the sun by 3° , we obtain $T_0 = 390 \pm 3^\circ\text{K}$, which represents the effective radiation temperature of the lunar ground with $h_\odot = 90^\circ$ at the Luna-13 landing site, calculated under the assumption that the surface is flat. In this case the integral albedo of the surface for solar radiation is within the limits of 2-7.5%.

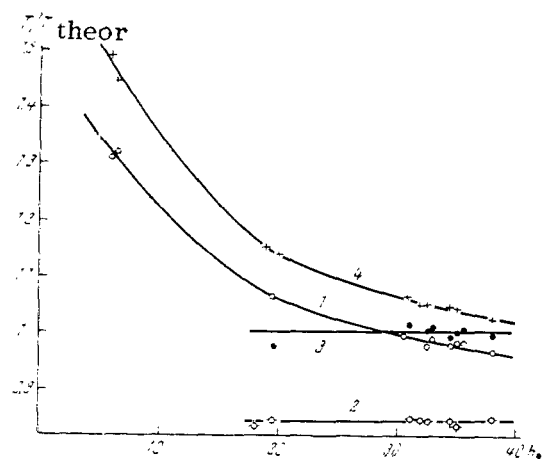


Figure 15. Ratio of the Measured Radiation Temperatures and the Temperature of a Black Surface.

PHOTOGRAMMETRIC ANALYSIS OF THE LUNAR PANORAMAS

1. CONSTRUCTION OF GROUND PLAN OF THE LUNA-13
LANDING SITE

Unlike the panoramas transmitted by the Luna-9 probe, the Luna-13 panoramas were obtained with essentially the same orientation relative to the lunar surface—i. e. from a single panorama center. Therefore the plot of the area imaged on the panorama is constructed using the perspective grid method described in the second part of Vol. I of the book "First Panoramas of the Lunar Surface" (Chapter 2, Section 1). Orientation of the panoramas relative to the quasi-vertical and the cardinal points was accomplished using the method described in Chapter 2, Section 2. The angle of inclination of the probe was found to be $13^{\circ}50'$, with an azimuth of the axis of inclination of 328° . Some probe components that were separated from it when the lobes were deployed, the radiation densimeter and the shadows of the antennas are visible on the panoramas. Since the dimensions of the probe components, radiation densimeter and antennas are known, it is possible to find the spatial panorama coordinates of points in the area on which shadows are projected or on which the jettisoned parts and radiation densimeter lie. These points were used as survey pegs for entering corrections for relief in the perspective grid and for laying out the contour lines (see Fig. 16).

The panoramas were interpreted taking into account the tests made in the stereoscopic analysis of the Luna-9 panoramas and also making use of the changed in illumination and dimensions of the shadows for various solar altitudes. This also permitted us to correct the positions of the contour lines and to extend them somewhat beyond the boundaries of the area provided with survey pegs, where they are indicated by the broken lines on the plot as being poorly defined.

/41

The portion of the panorama provided with survey pegs was represented as a topographical chart, scale 1:20, which is accurate to about $\pm 10\%$ in position and ± 5 mm in height. Just as with the Luna-9, all surveyed areas are shown as a topographical diagram to a scale of 1:40 (See Supplement).

The areas in the vicinity of the Luna-9 and Luna-13 landing sites are similar in topological relationships, abounding in small craters and rocks. However the Luna-13 site is considerably more rocky, although rocks as large as those on the Luna-9 panoramas do not occur.

Formations not noted on the Luna-9 panoramas are visible on the panoramas transmitted by Luna-13. These are micro-faults, noted on the chart as rims, small ridge-like protuberances (17, 18 on the sketch), rocks differing in brightness from other rocks (23), micro-depressions (46), rock-tracks (50) and the impression of the lobes of the probe.

The analysis of the panoramas in the Luna-13 area confirmed the correctness of the interpretation of the craters as being circular. In laying out the plan of the Luna-9 landing area the contours of most craters were related to survey-peg

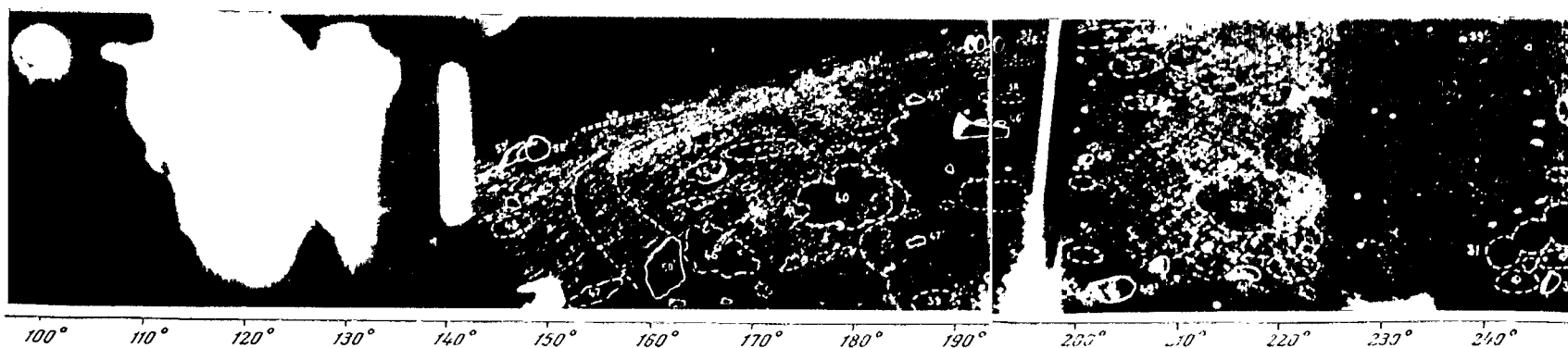
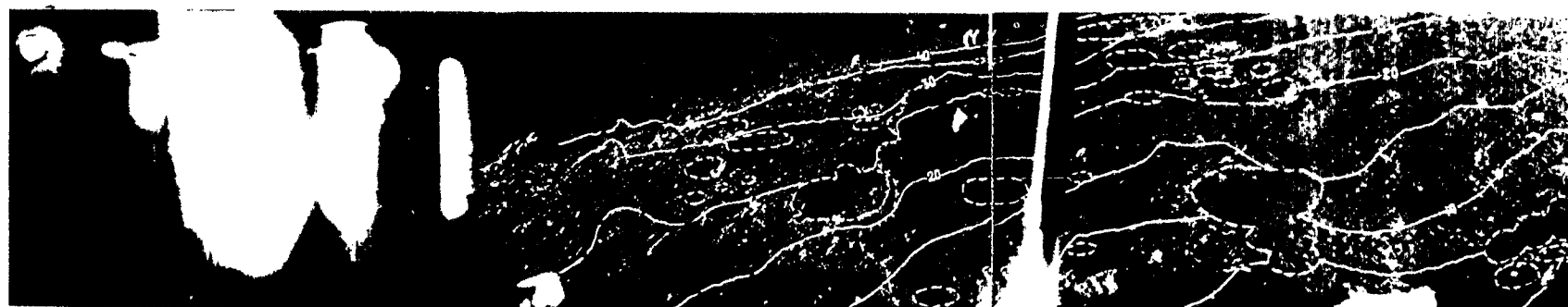
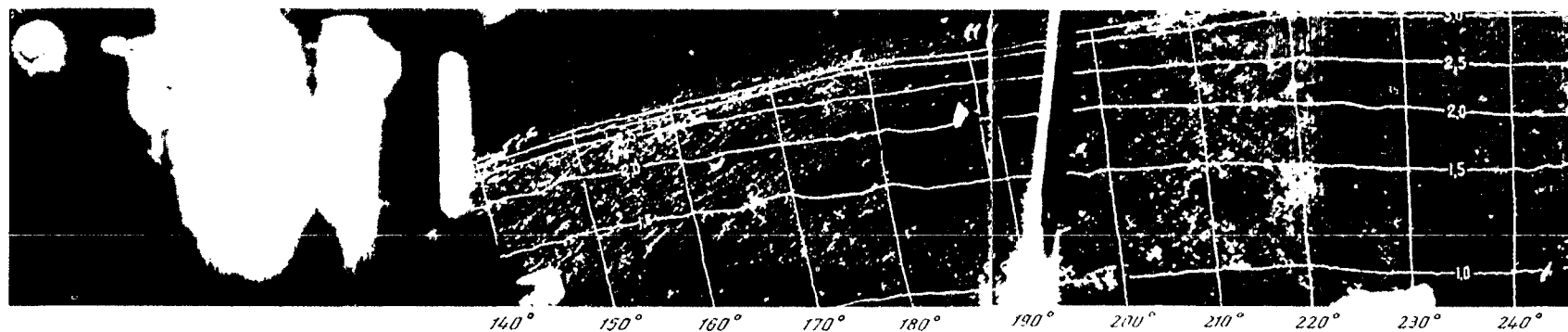
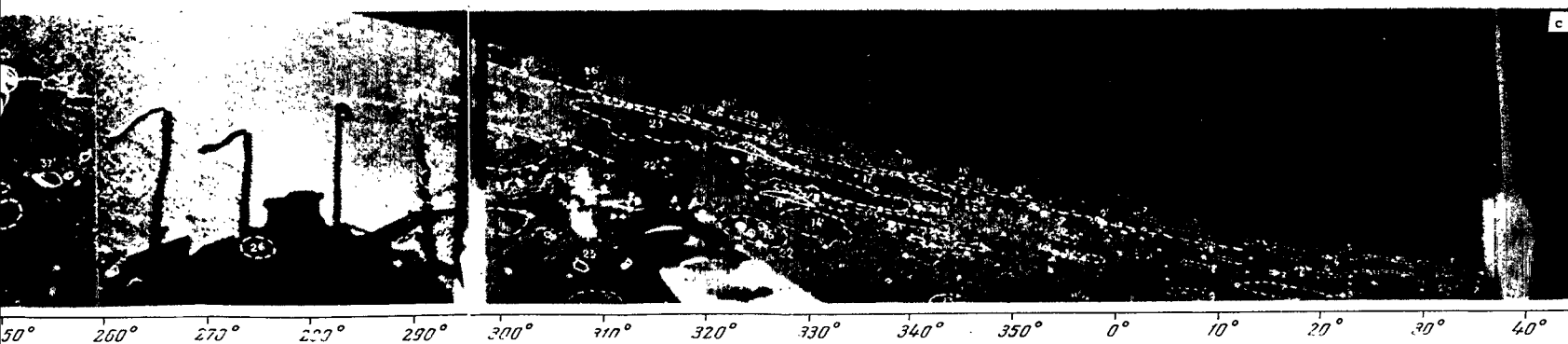
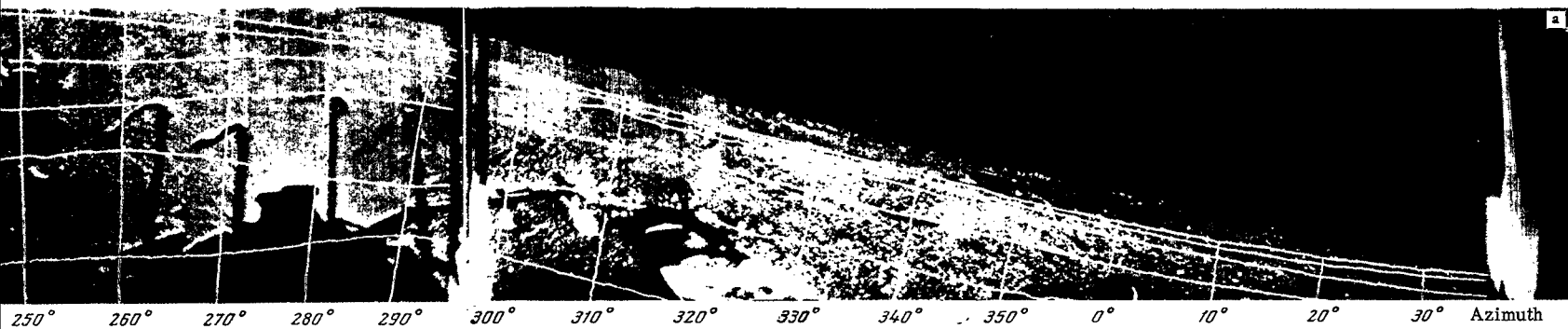


Figure 16. (a) Range Lines, Plotted each 0.5 Meter and Azimuth Lines Plotted each 10°; (b) Contours (each 10 cm.) (c) Objects Noted on the Plan and Area Sketch.



points. In those cases when the rim of a crater was fixed by more than three survey pegs they were always entered on the circumference. Craters visible in the Luna-13 panoramas were also developed as circles on the plan in accordance with the perspective grid. In view of the small slopes of the area this can only be explained by their circular form in nature.

2. STUDY OF LUNAR SURFACE RELIEF ALONG THE HORIZON LINE

The horizon line on all panoramas is distorted due to the inclination of the probe. An undistorted horizon line similar to that obtained by the photographic method used with the first Luna-9 panorama can be obtained by rectifying the panorama. This in turn affords the possibility of establishing some numerical characteristics of the relief and making a statistical appraisal of them from an undistorted horizon line.

The rectification of the distorted horizon line was made analytically to exclude the additional errors introduced by photo-rectification devices and the assembly of the individual frames. In this process a point on the horizon line was first projected onto planes tangent to the picture sphere and the perpendicular planes of the panorama, and then rectification was carried out in the vertical plane. The plane-transformed coordinates were recomputed into panorama coordinates corresponding to a panorama with zero angle of inclination.

The undistorted horizon lines shown in Fig. 17 were plotted in these coordinates. The vertical scale is larger than the horizontal scale by a factor of 10 for purposes of graphic display.

A total of 100 characteristic points were selected on the horizon line on the first Luna-9 panorama; 66 points were selected on the second Luna-13 panorama.

The amount h that the characteristic points lie above some plane taken as the horizontal can be established from the rectified panoramic picture. This plane coincides with the horizontal if the probe is located on level ground. To define the relative altitude difference h in linear measure, the distance D from the probe to the visible horizon must be known:

$$h = D \tan \beta. \quad (1)$$

In view of the smallness of the angular distance β of the characteristic points on the horizon we can write, after coordinate transformation:

$$h = D \beta. \quad (2)$$

It is possible to restrict the consideration for the relief characteristic by using only the local deviations in elevation of neighboring characteristic points on the horizon:

$$\Delta h_i = D(\beta_{i+1} - \beta_i) = D \Delta \beta_i. \quad (3)$$

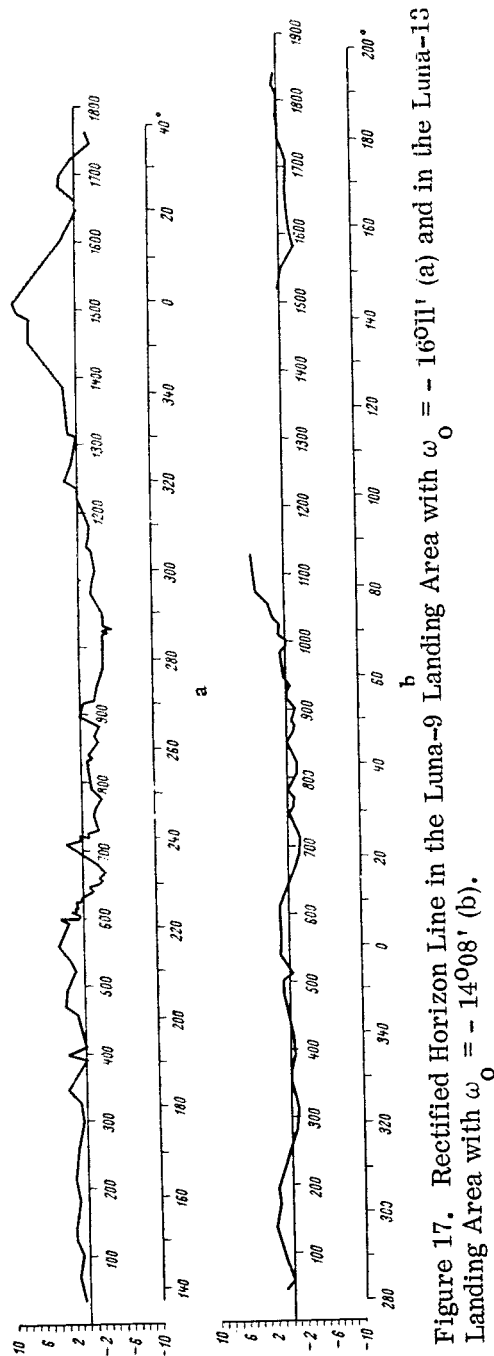


Figure 17. Rectified Horizon Line in the Luna-9 Landing Area with $\omega_0 = -16^{\circ}11'$ (a) and in the Luna-13 Landing Area with $\omega_0 = -14^{\circ}08'$ (b).

An estimate of the relief was also made from the angle of inclination γ of the region between two characteristic points, which is defined as

$$\gamma_i = \arctan \frac{\beta_{i-1} - \beta_i}{\gamma_{i-1} - \gamma_i} = \arctan \frac{\Delta \beta_i}{\Delta \gamma_i}. \quad (4)$$

Here it must be assumed that both points defining the angle γ lie on the horizon line. In this case we actually measure their projections on the vertical plane and not the angles of inclination themselves.

The average angle of inclination γ_{av} , with the zero-point values taken into account, turned out to be 0.9° for the landing area of Luna-9 and 2.5° for the Luna-13 landing site. The maximum angle of inclination was 39° .

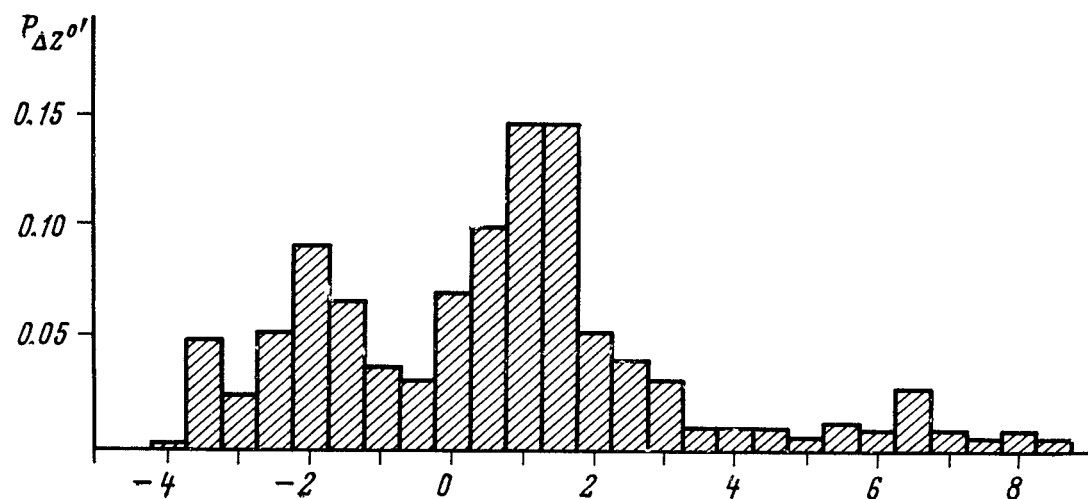
The relative elevation differences were calculated from formula (3) for the Luna-13 landing site only, since a sufficiently reliable resolution could not be obtained for Luna-9.

The average relative elevation differences for Luna-13 amounted to ± 1 meter. The elevation differences of individual points were in the range of 1-3 meters for Luna-9.

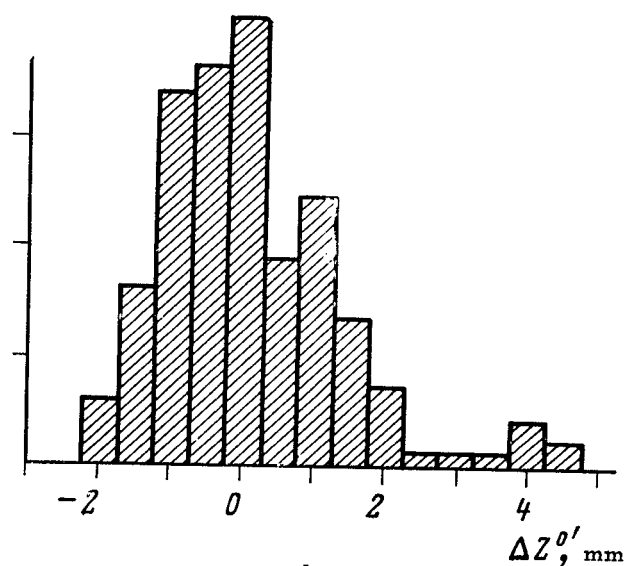
The histograms of the distribution of relative elevation differences and a angle of inclination in Figs. 18 and 19 were plotted from these data.

A comparison of the data on the angle of inclination for the Luna-9 and Luna-13 landing sites and the Ranger-7 site attests to the similarity of the integral distribution functions of the angle γ (Fig. 20).

From this we can conclude that according to the data for all three landing sites the angles of inclination of the areas lie essentially below 30° ,



a



b

Figure 18. Histogram of the Distribution of Points of the Rectified Profiles in the Landing Areas of Luna-9, with $\omega_0 = -16^{\circ}00'$ (a), and Luna-13 with $\omega_0 = -14^{\circ}08'$ (b).

with the fraction of angles above 10° being less than 1%. For the Luna-9 site this percentage was 3.3% and for the Luna-13 area it was zero.

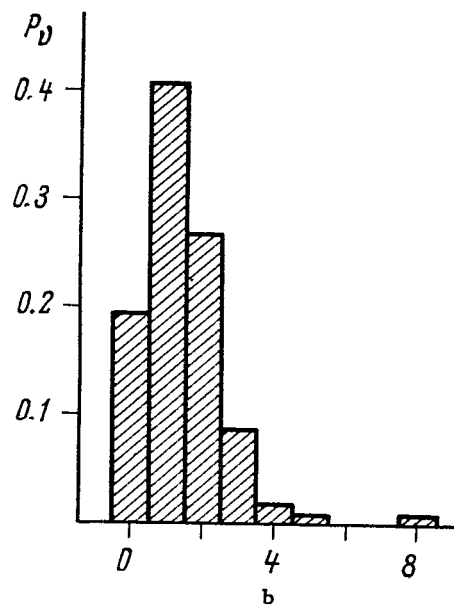
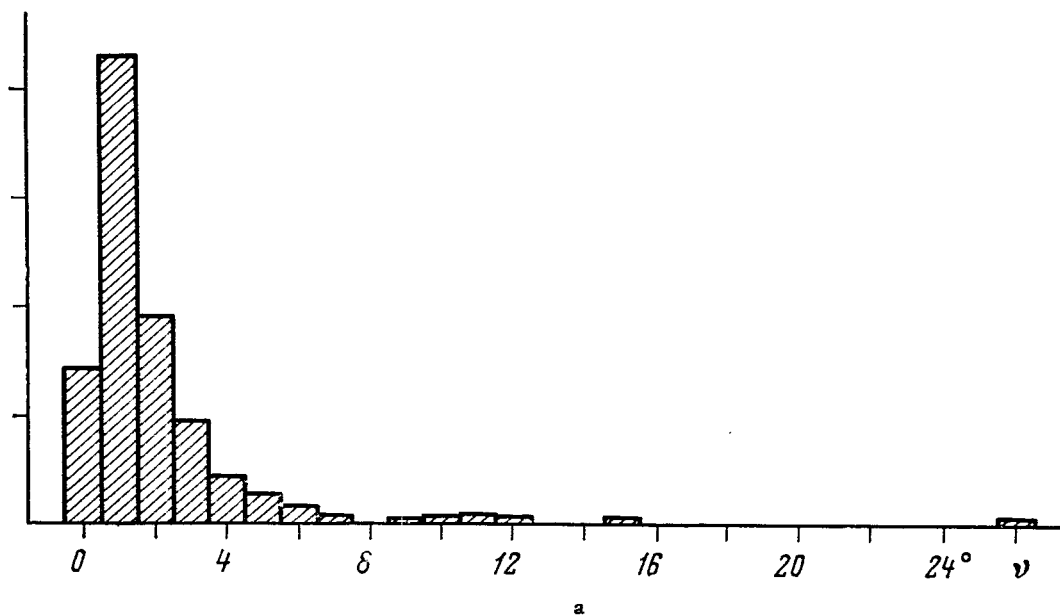


Figure 19. Histogram of the Distribution of Angle of Inclination of the Terrain in the Region of the Landing of Luna-9, with $\omega_0 = -16^{\circ}00'$ (a) and Luna-13, with $\omega_0 = -14^{\circ}08'$ (b).

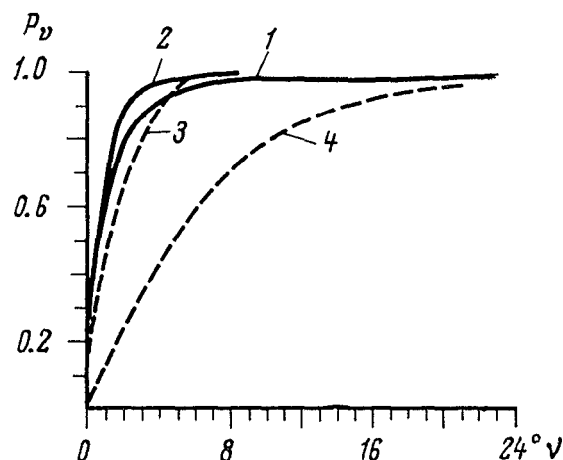


Figure 20. Integral Distribution of Angles of Inclination of the Terrain in the Landing Areas of Luna-9, Luna-13 and Ranger-7.

From Data for Luna-9 (1), Luna-13 (2) and Ranger-7 (3) with 40-ft Intervals between Cuts; (4) Ranger-7 with 1.25-Foot Intervals between Cuts.

3. STEREOPHOTOGRAMMETRIC STUDY OF THE SHAPE OF A ROCK

/46

With the aim of making a detailed study of the micro-relief of the lunar surface and of the individual formations, new photogrammetric studies were made of the panoramic views obtained with Luna-9 to supplement the results of the topographical chart and sketch and the photo-map given in the second part of Vol. 1 (Chapter 1). The new measurements were based on the solution of a spatial panoramic cut in the zone of most favorable stereo-effect using an analog stereophotogrammetric instrument.

The available stereophotogrammetric instruments only permit analysis of plane pictures, but the panoramas must be considered to be images obtained by central projection onto a sphere (see Vol. 1, Chapter 1, Section 1). The radius of the spherical surface is the reduced focal length of the TV camera and is defined from simple geometrical considerations. Therefore, in contrast to the analytical method, the method of solving a spatial panoramic cut on an analog device is not as rigorous and is limited to that portion of the panorama amenable to analysis in a single run. It is easily shown, for example, that a portion of a spherical panoramic view with angular dimensions of $15^\circ \times 15^\circ$ can be approximated by a plane, allowing for an error in coordinates equivalent to one resolution element. This means that the panorama must be handled as a series of plane pictures. Similar considerations were also observed in carrying out this study.

An interesting object for study on the panoramic views is the rock located in the area $\gamma = 150^\circ - 160^\circ$ (No. 57' on the topographical plan) and the region adjacent to it. Therefore two overlapping 10 x 10 cm sections of the third and first panoramic views, with the rock centrally located, were selected for analysis (Stereo pair 10, Vol. 1, Part 3). The section of the third panorama is the left-hand frame of the stereo-pair and the first panorama section is the right-hand frame of the stereo-pair. The pictures overlapping by $\sim 100\%$ and points close to each other were taken as cardinal points. The cardinal rays of the pictures (passing through the cardinal points) were oriented differently relative to the local vertical and also relative to the picture base and converge. Therefore the selected stereo-pair relates to the general case of ground survey photography, which is rarely encountered in photogrammetric practice. A method deviating from standard schemes was used in the analysis.

/47

The stereo-planigraph is a universal stereophotogrammetric instrument on which pictures may be analyzed in the general case of ground survey photography. By inverse projection of photographs with a base equal to that of the photo to some scale, this instrument is able to restore the bundle of rays that existed during the photographic process and, by their mutual orientation, construct a geometrical model of the area and orient it relative to the rectangular coordinate system of the instrument so that the selected area is oriented relative to the local coordinate system, and carry out accurate measurements on the model. The model being measured is projected orthogonally onto one of the coordinate planes of the instrument and the projections are mapped out by the coordinatograph to the plan scale. The focal length of the projection cameras is 200 mm and therefore, so as not to disturb the bundle of rays during projection, the selected panorama fragments were reduced by a factor of 1.9. This reduction made the reduced focal length equal to 200 mm.

To obtain a horizontal model of the area after mutual orientation, the so-called angular elements of external orientation α_L , ω_L , κ_L were computed for the left-hand photograph from the absolute tilt angle of the third panorama, the azimuth of the tilt axis and the base (see Vol. 1, Part 2, Chapter 1, Section 3). Their values ($\alpha_L = +13.6^\circ$, $\omega_L = -14.3^\circ$, $\kappa_L = -23.9^\circ$) were set up on the left-hand projection camera of the device, taking into account the scale zeros. The right-hand photograph was machine-set to the left-hand photo in the mutual orientation process, which was done by eliminating vertical parallax using the scheme applicable to converging photographs. The angular motions of the right-hand camera and the base motions b_y , b_z were used. The base b_x established was $\sim 1/10$ the base obtained in the topographical mapping. The final scaling of the model was made from the survey points on the topographical plan. Projection was made onto the XZ-plane of the instrument and the plan obtained from measurement of the model was recorded by the coordinatograph at a scale of 1:2. An estimate of the accuracy was made from 16 survey points, in general from the survey points of the topographical plan. The average deviation of points in the plan amounted to 4.3 cm, with a maximum of 8.4 cm. The mean-square error in height was ± 1.4 cm, with a deviation limit of 3.0 cm. The results are shown in Figs. 21 and 22.

/49

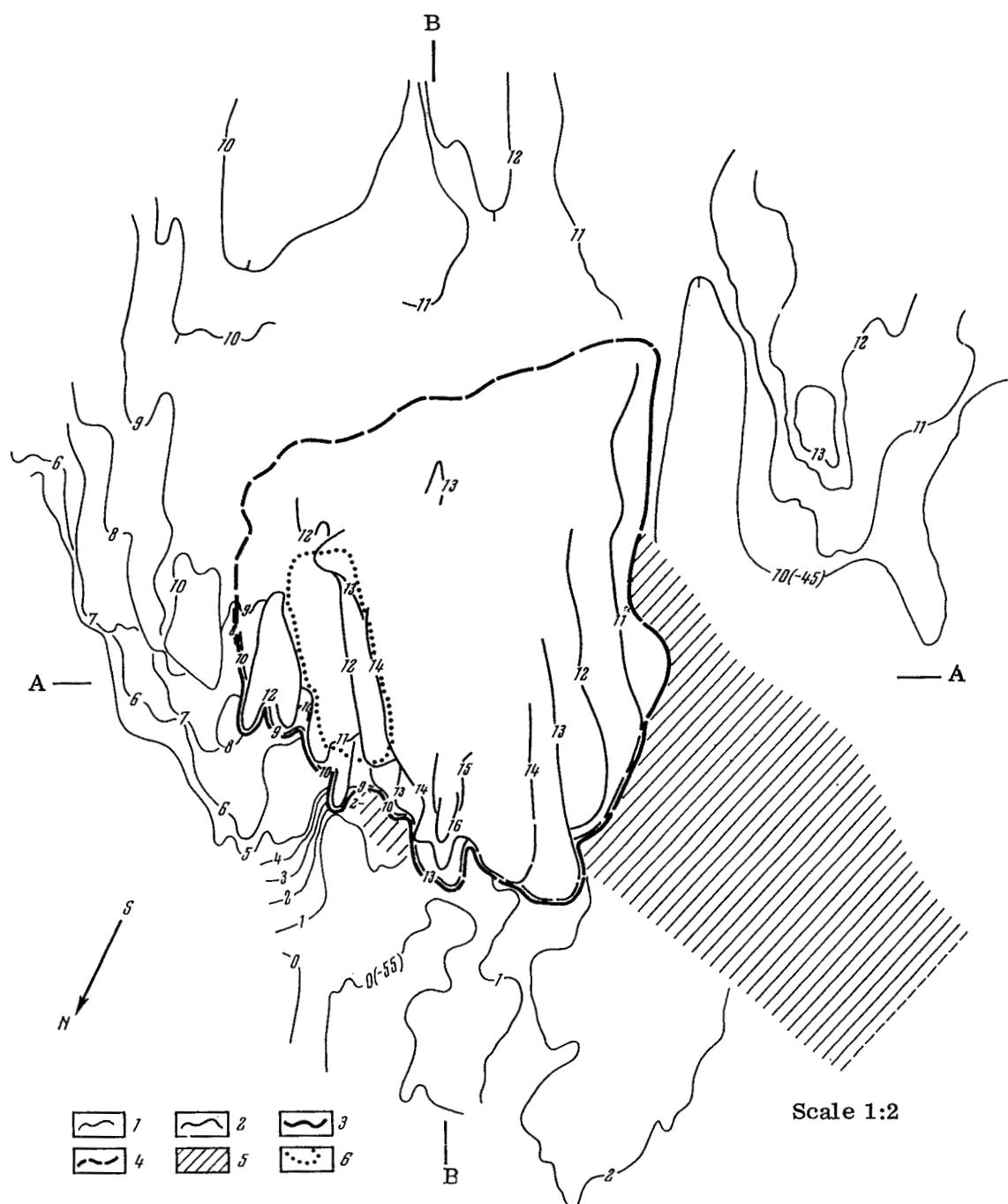


Figure 21. Rock Formation (Luna-9 Photograph, $\gamma = 150^{\circ}$ - 160°). The Contours on the Rock and in the Adjacent Portion of the Lunar Surface are Plotted at 1-cm Intervals.

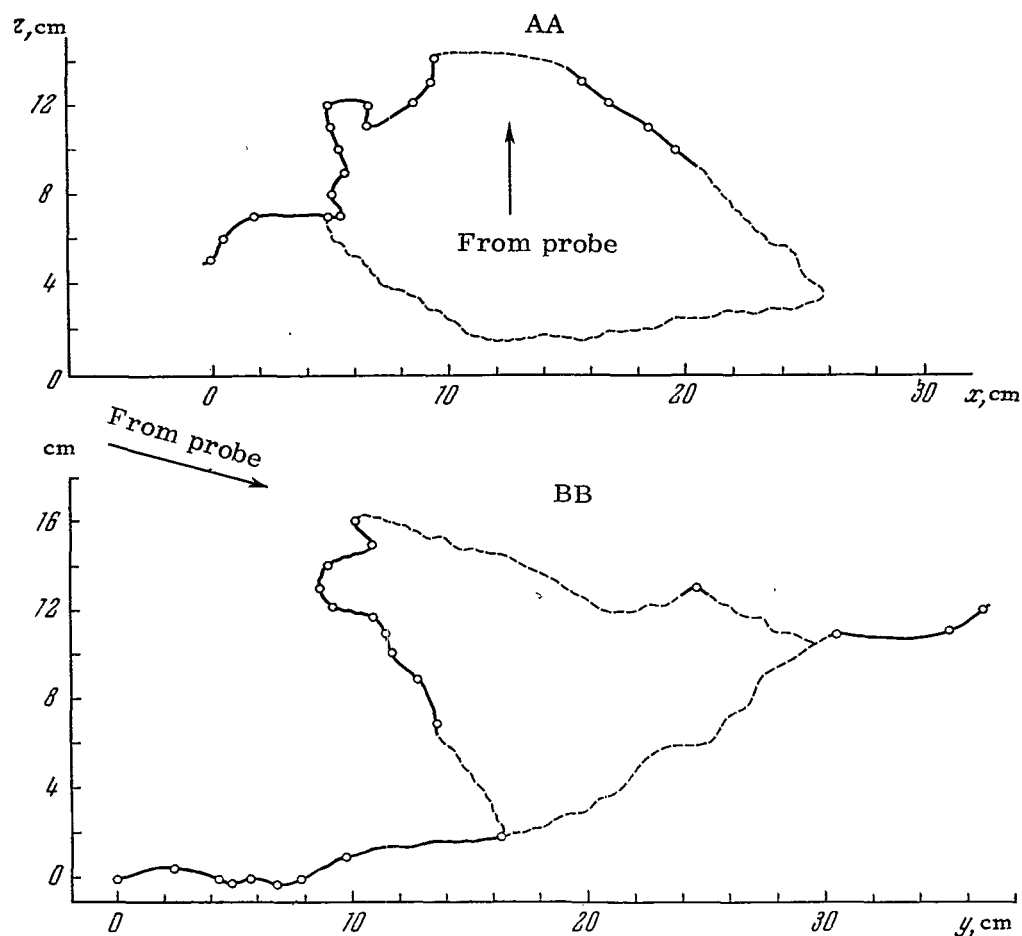


Figure 22. Rock Profiles (Luna-9 Photographs, $\gamma = 150^{\circ}$ - 160°).

Figure 21 shows the image of the rock and its immediate surroundings as contour lines (2, 1 respectively). The plan section is oriented so that the direction BB, directed upward, corresponds to the direction from the probe. The numbers of the contours in parentheses relate the heights of the plan to the topographical plan. The contours in the rock shadow are shown as conjectural by the broken line (4). The rock's shadow is the region shown shadowed on both panoramas (5). The front edge of the rock is plotted as a solid black line (3). The unseen edge is plotted provisionally by the heavy broken line (4). The contours on the rock are broken off at the junction of the visible and invisible portions of the rock. There is an unobserved (dead) zone behind the rock.

/50

The sides of the rock turned toward the probe and the northeast side are strongly differentiated, the southeast slope is less pronounced. The northeast side falls off almost perpendicularly to the base. On this same side there is a

marked flat inclined area (6) bordered on each side by small flange-like rims. The slope toward the probe overhangs toward this side. The overhang angle is $\sim 50^\circ$ from the horizontal plane. The highest point of the rock is found here. The southwest, south and southeast sides join smoothly into the surrounding area. In the long-range plan the rock is seen as a single protuberance. The rock is ~ 14 cm in height, its length in the direction of the probe is ~ 21 cm and its width in the direction AA is ~ 15 -20 cm. The rock lies on a slope and is tilted toward the probe and toward the southeast.

Profiles of the rock in two mutually perpendicular directions, AA and BB, are shown in Fig. 22. The profiles were constructed from the contour lines. The dotted lines indicate the assumed provisional outline of the rock.

MORPHOLOGICAL FEATURES OF THE LANDING SITE

The Luna-13 probe landed near the eastern edge of the Ocean of Storms near a point with coordinates $18^{\circ}52'$ N and $62^{\circ}03'$ W. This location is marked with a cross on the chart (Fig. 23) and is about 300 km from the Luna-9 landing site.

The general nature of the landing area—a flat mare plain—was similar in kind to the Luna-9 landing area. It may be noted that the Luna-13 landing site area is even more representative of normal maria plains that have not been subject to the complicating influences of "continental" regions or have developed structural relief inhomogeneities.

The Luna-13 also landed in a crater-like depression, which made the operational conditions similar to those of Luna-9. The about equal inclinations of the panning devices of the probes and an image scale identical with that of Luna-9 allowed us to confine the comparative description to panoramas yielding a better representation of the general surface characteristics of the western portion of the Ocean of Storms and avoid unnecessary repetition. At the same time it turned out to be possible to speak more confidently of the typicalness of the formative processes.

The essential difference between the panoramic views obtained is that the probes were oppositely oriented with respect to the sun. The axis of Luna-9 was inclined toward the east, so that the details closest-in are observed against the sun under conditions of high illumination contrast. The Luna-13 axis is inclined in the opposite direction (away from the sun) and a number of close-in details were shadowed by the probe. The more remote areas of the western portion of the Luna-13 panoramas are viewed in frontal illumination and are therefore not over-contrasted and exhibit a smooth transmission of all half-tones and a great many details.

/52

A stereo effect that could be interpreted as a change in position of the probe with respect to the arm of the radiation density-gauge during the panning process was noted on the Luna-13 panoramic views. However, this effect turned out to be inadequate for reliable use in plotting a chart of the area.

Because of the less rigorous conditions for compiling the topographical diagram of the landing zone from the Luna-13 panoramas, a different treatment of the mutual disposition of relief details was possible, particularly in areas not appearing on the topographical diagram. This required a very careful approach to any type of statistical treatment, while yet retaining the correctness of the qualitative results.

The lunar landscape visible on the Luna-13 panoramic views is quite similar to that seen on the Luna-9 panoramas. The flatter horizon line on the Luna-13 panoramas may be explained by assuming that the area was more level and the range to the visible horizon was greater.

The observed differences in micro-relief can apparently be explained as statistical fluctuations of local significance. This types of formations observed are described below.

In some cases it was possible to make differing interpretations of details visible on the panoramas. We then attempted to describe the respective limiting factors to indicate the probability of the different interpretations of the feature being described.

1. LUNAR PTS

As in all large-scale representations of the lunar surface, pits (small craters) are the most wisely distributed and typical negative relief formation. These are quite clearly demarcated circular depressions of various sizes in the vicinity of the landing site. As already stated, the probe itself landed in a relief depression which we shall call the central depression.

/54

This depression is depicted by the complex system of contour lines on the topographical plan and diagram of the landing site (see the plan and diagram at the end of this volume). From a number of considerations this depression can be considered to be a large craterlet.

Thus the close-in portions of the Luna-9 and Luna-13 panoramas do not show the level surface of the Moon but rather the inside slopes of small lunar craters about 10 m in diameter. The depression in which the Luna-9 was located is shown more clearly and has a more regular shape, which may possibly relate to the time of its formation.

The small crater in which the Luna-13 was located was more complex and its inside slopes were covered to a depth of about 5 cm by a more worked-over and friable material, as demonstrated by direct penetration. In this connection it was a matter of interest to define more precisely the structure of this central depression.

The structure of the central depression can be judged by analyzing the clearly visible formations on the panoramas representing the rims of craters or their analogs.

However, the lack of reliable determinations of the ranges to the rims did not permit interrelating the relief convolutions visible on the right-hand and left-hand portions of the panoramas with sufficient reliability. It should be realized that the rims that are clearly visible in certain areas extend into other areas where their location is somewhat indeterminate.

/55

In particular, two interpretations of the boundaries of the central depression are possible: According to the first of these the depression is bounded by rim I (see Fig. 9); according to the second interpretation the boundaries of the depression are rim I in the right-hand portion of the panorama and the relief fold noted in the left-hand portion of Fig. 16c.

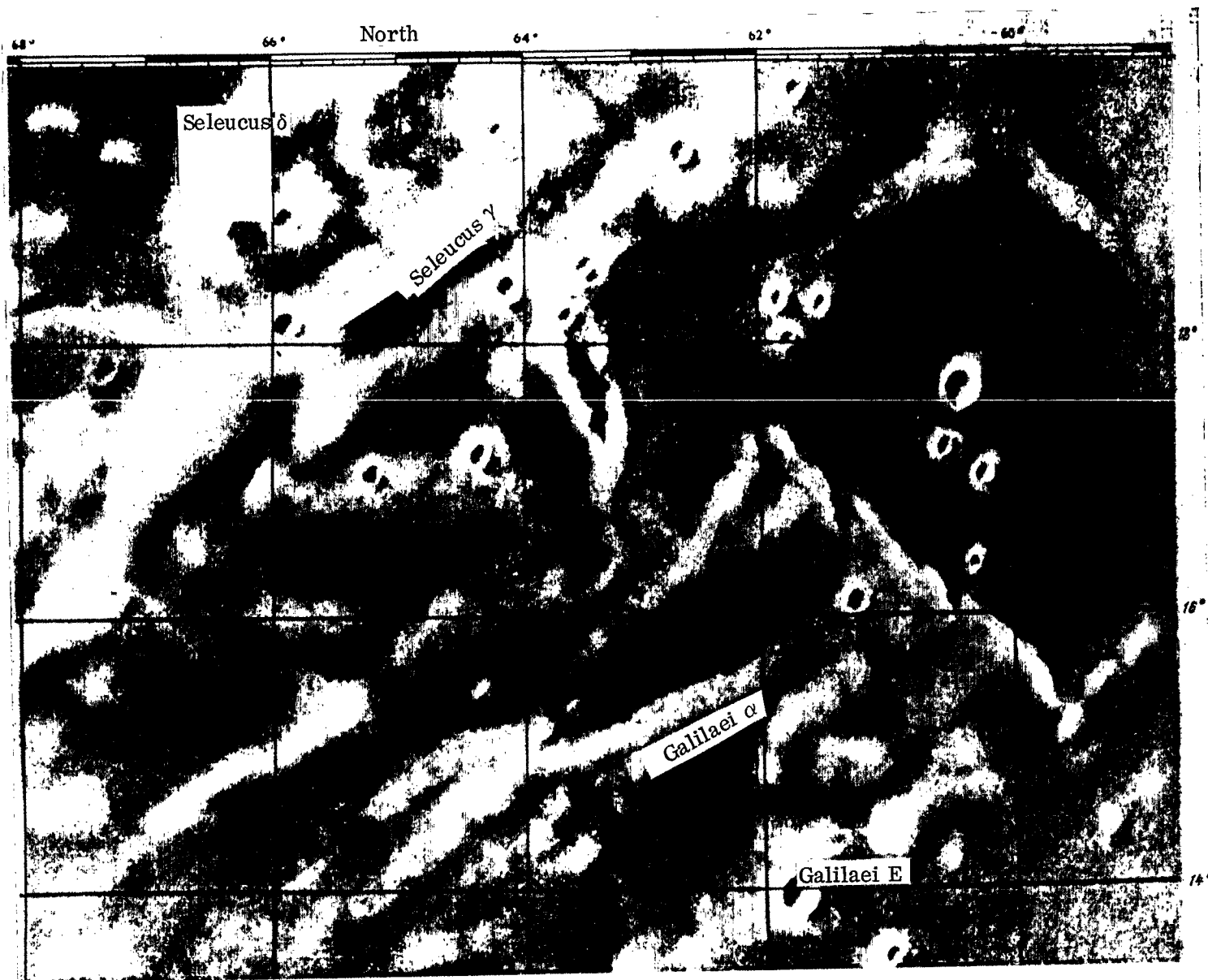


Figure 23. Chart of a Portion of the Lunar Surface.

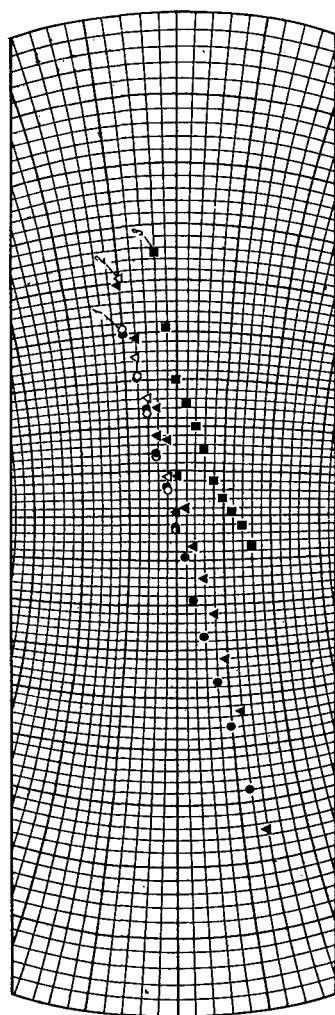


Figure 24. Spherical Coordinates of the Visible Horizon (1), Rim I (2) and Rim II (3).
The Blacked-in Symbols Relate to the Northern Portion of the Panorama, the Light Symbols Refer to the Southern Portion.

responds to the steepness of the sides of similar formations plotted from the stereoscopic pictures of Luna-9. This representation is well corroborated by the plot of the surface clearly visible in the right-hand portion of panoramas II and V (275° - 320°), but an analysis of their left-hand portions (150° - 180°) admits of the assumption of a considerable departure from the round configuration of the depression, which is also evident in the arrangement of the visible edges of the slope on the topographical diagram. In this case, if the outer rim in the plan represents a circle, the probe appears to be located on the eastern slope of the crater (Fig. 27).

It is clear that two hypotheses may be advanced as to the origin of the complex relief of the central depression: 1) the superposition of two craters of independent origin or the complex relief of a large crater, perhaps connected

The first interpretation leads to the conclusion that rim I is parallel to the horizon, rim II (Fig. 24) is tilted with respect to rim I by about 15° and is reliably traced out only on the northwest slope of the depression (Fig. 25). It should be noted that rim II is somewhat masked at the north by the out-of-focus image of the cable of the radiation densimeter arm. An analysis of the mutual disposition of the rims carried out with the perspective grids described in the first volume of this publication (plan of rims, see Fig. 25) permits deducing that the probe is located on the north slope of the depression, about 1-2 meters from the rim, while the distance to the rim toward the south is about 10 meters (see Fig. 26 for an overall diagram of the structure of the depression).

/56

In the second interpretation the distance from the probe to the outer rim is set within the limit of about 3-4 meters and 1.5-2 meters up to the inner rim (clearly expressed in the interval 275° - 032°).

Figure 27 illustrates the two possible versions of the profile of the southern portion of the central depression in this representation. The first version is plotted from the horizontal plan and yields an average slope inclination of about 6.5° . The second version is plotted on the basis of an assumed profile of a small crater with an average edge slope of the order of 9° , which cor-

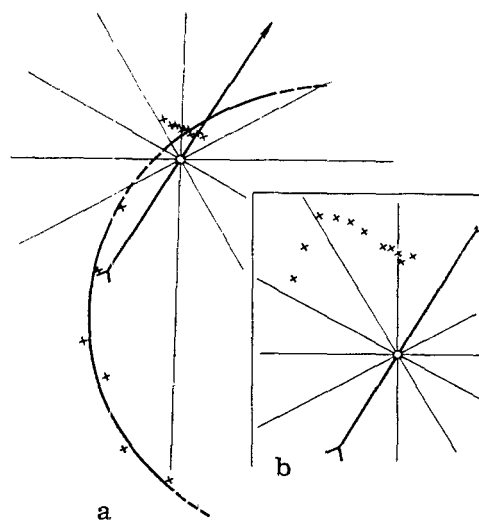


Figure 25. Plan of Rim I (a) and Rim II (b). Scales are Arbitrary and Different.

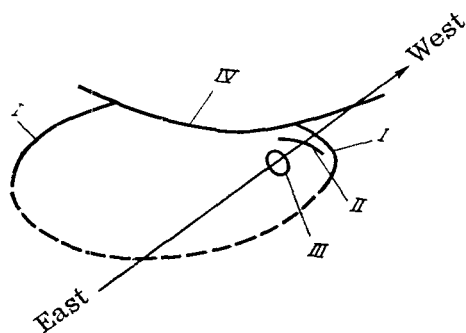


Figure 26. Overall Diagram of the Structure of a Portion of the Surface of the Luna-13 Landing Site:

I - Edge of Central Depression (Rim I); II - Rim II; III - Probe Location; IV - Upper Boundary of Panorama.

with the non-uniformity of the mechanical properties of the ground observed on the Luna-9 panoramas; 2) the presence of landslide formations, perhaps caused by the reaction of the lunar soil to the probe.

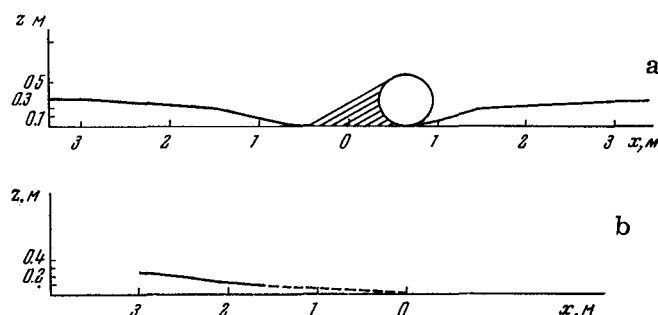


Figure 27. Possible Versions of the Relief Structure of the Luna-13 Landing Site:

a - Craterlet with a Folded Rim; Cut along the W-E Line; b - Profile of a Section along the 250° Line Taken from the Topographical Plan.

The parallelism of the northern portions of rims I and II (see Fig. 25), which may be interpreted as a breakdown of rim I, seems to support the second hypothesis.

The maximum diameter of the clearly visible pits is about 85 cm (325° - 345°). Attempts were made to separate out the smallest pits, which usually merged into the general unevenness of the pitted nodular ground. In the area of best visibility ($\sim 15 \text{ m}^2$) only 17 pits with diameters less than 5 cm could be observed out of the total of 82; of this number 7 were less than 3 cm in diameter, which is at the extreme limit for any circular depression in the ground.

/57

The nature of their size distribution can be judged from Table 4, which shows the crater distribution in this area.

An analysis of the table and the Luna-9 data indicates that the numerical density of small craters with diameters of the order of 1 cm corresponds to the number obtained by extrapolation of the curve for large craters.

The craters are not uniformly distributed; they are found in clusters, forming complex and irregular depressions in which the separation of the individual craters becomes somewhat arbitrary. It is possible that the presence of such groupings is in part conditioned by their visibility on the panorama. All craters of the sizes indicated occupy about 13% of the area of this sector. It should be noted that most of the Luna-13 craters were less clearly delineated and their contours were more diffuse and softer than the craters shown on the Luna-9 panoramas.

2. LINEAR STRUCTURES

In contrast to the linear structures described from the Luna-9 panoramas, which formed positive micro-relief elements with greater solidity than the

TABLE 4. Distribution of Craters by Size

D, cm	No. of crater	Overall area occupied by craters, cm ²
To 3	7	49,7
3 — 5	10	126.0
5 — 7	9	253,8
7 — 9	12	600.0
9 — 11	4	312.0
11 — 13	8	904.0
13 — 15	9	1350.0
15 — 17	6	1200.0
17 — 19	3	762.0
19 — 21	2	628.0
21 — 23	1	380.0
23 — 25	2	900.0
25 — 27	2	1060.0
27 — 29	4	2480.0
38	1	1130.0
50	1	1960.0
84	1	5500.0
Total	82	1.96 m ²

surrounding soil, the linear elements observed on the Luna-13 panoramas were for the most part negative micro-relief forms of the nature of fissures or cracks.

The linearity of the positive structural elements on the left side of the panorama (see, for example, panoramas IV and V, 150°-180°) is rather problematical and cannot be considered as definitely established. It is possible that this effect is only apparent and can be ascribed to lighting conditions and the psychological conditions of the observations, although a complete negation of their presence also does not seem possible.

The portion of panoramas I, II, III, V, 320°-330° containing the narrow wedge-shaped shadow running behind the elongated ridge of rock admits of a dualistic interpretation. It may be interpreted as a narrow protuberance above the surface of the bedrock about 0.5 meters in length (as shown on the topographical diagram), or also as a small slit-shaped depression extending 0.5-0.8 meters, starting from the crater.

/58

The fissure at the crater (Fig. 29, panoramas II, III, V, 180°) accompanied by a linear positive structure is more reliably observed. The rim II described

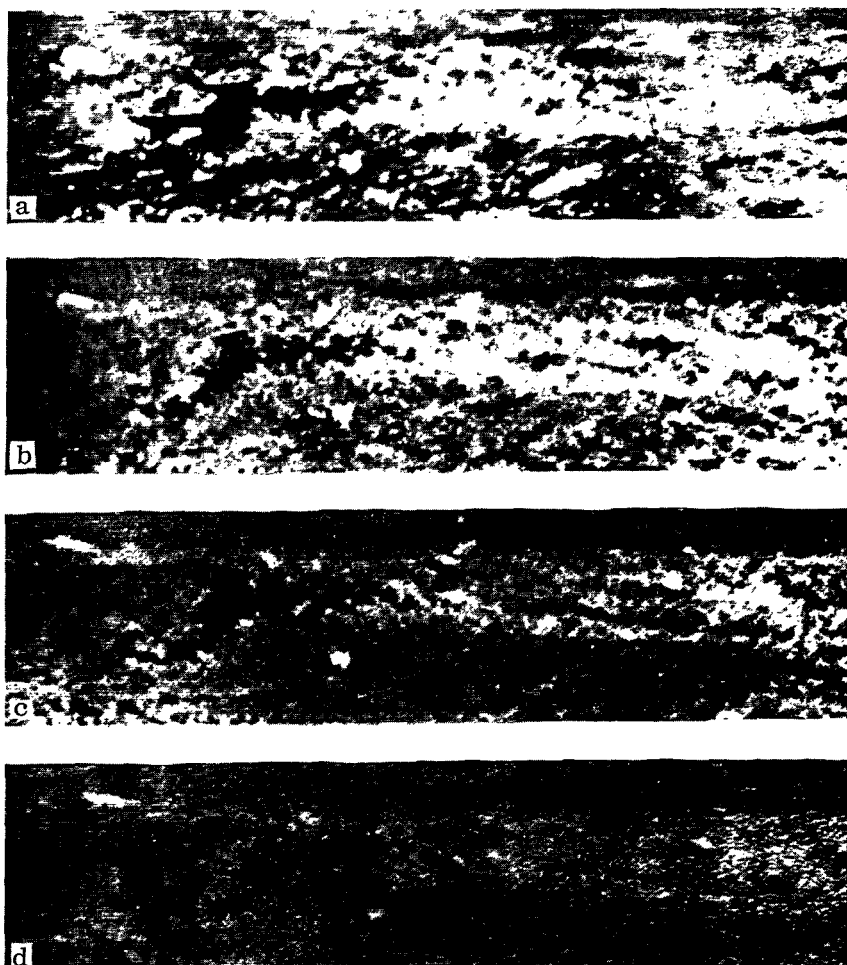


Figure 28. Elongated Wedge-Shaped Shadow from a Ridge of Rock or a Slit-Shaped Depression in the Surface (320° - 330°).
a - Panorama I; b - II; c - III; d-V.

above (Figs. 9, 16, panoramas III, V, 275° - 320°) should be placed in this category of linear formation: It appears as a clear change in the slope of the depression, perhaps of the nature of a "fault".

/60

3. ROCKS AND NODULAR CLUMPS

Unlike the Luna-9 panoramas, where only "stones" were distinguished, we here deem it possible to delineate another group of formations—the "nodules". Ground structural formations such as isolated, rather weakly-bonded nodular clumps of irregular shape are placed in this category. A clear morphological

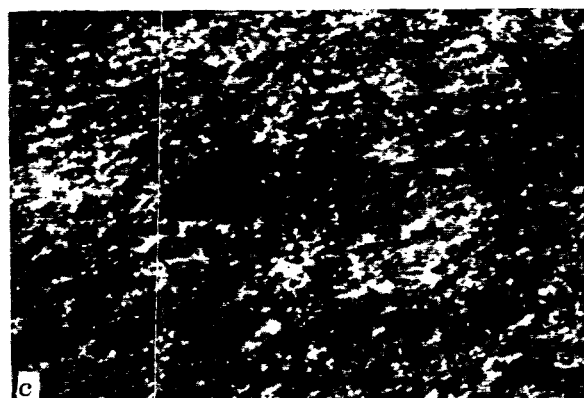
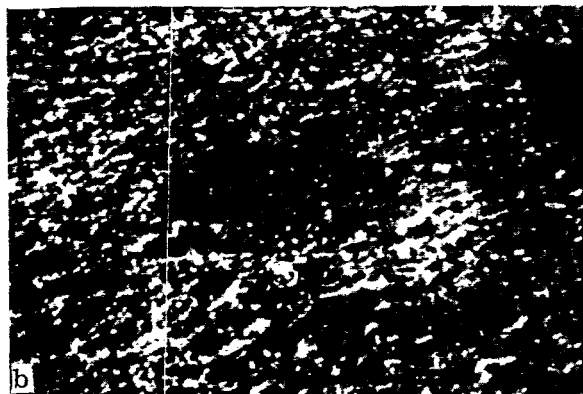
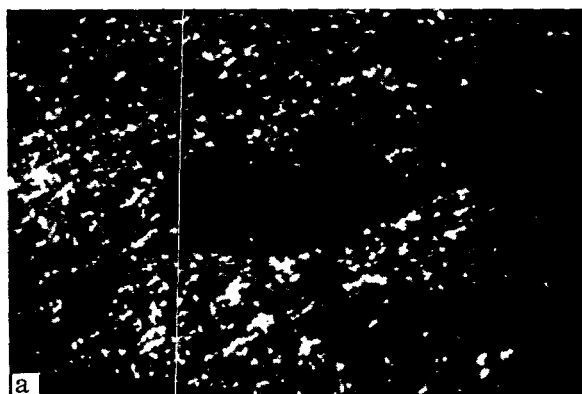


Figure 29. Small Crater with Traces of a Linear Formation in the Left-Hand Portion (170° - 185°):

a - Panorama II, b - III, c-V.

distinction between small stones and nodules is possible only in clearly typical cases when it is possible to consider the nature of a surface fracture or other indications of the enhanced solidity of the formation or of its clear differentiation from the surrounding grains of soil. Nevertheless the state of aggregation of the soil is not in question. The size of known nodules does not exceed 3 cm (with the predominating size not above 1-2 cm).

Stones are typically more sharply differentiated from the surrounding ground than are the nodules. In categorizing the smaller stones it is almost impossible to differentiate solid stones from friable nodules, and they both fall into a single category.

Rocks. 501 rocks were plotted on the topographical diagram of the Luna-13 area, over an area of about 55 m², whereas a selective enumeration over the panorama indicates that about 30% of the rocks were not plotted on the plan—i. e. the total number must be set at not less than 750-800 rocks or up to 15 rocks per square meter.

181 rocks are shown within 3 meters (145°-320°) of the probe.

If we consider the close-in region of the panorama in more detail and divide the region into sectors, we find that the concentration of rocks is 12.3 rocks per square meter in sector I, lying within 2 m and with an area of 6.16 m²; in sector II, from 2-3 meters, area 8.17 m², 12.8 rocks per square meter. Thus, considering that there is a clearly defined field of concentration of rocks in the right-hand portion of the panorama (320°-035°), and average concentration of 15 rocks per square meter would not be an overestimate. Table 5, drawn up from the data of the topographic chart, gives an approximate picture of the nature of the distribution of rocks by size.

It should, however, be remarked that selection by observers naturally could not be relied on in compiling the topographical diagram due to the finite resolving power of the apparatus. In this connection, two observers made independent rock and nodule counts over narrow sectors in three Luna-13 panorama fragments. The same observers made control counts of rocks on one panorama fragment from Luna-9. The results of these counts, referred to an area of 100 m², are shown graphically (Fig. 30), where the Roman numerals correspond to the range zone number and the curves show the approximate average obtained from the observational selection. The "stratified" distributions for range zones II and III of fragment 330°-010° for Luna-13 can obviously be attributed to range indeterminacy due to the relief complexity in the central depression.

/62

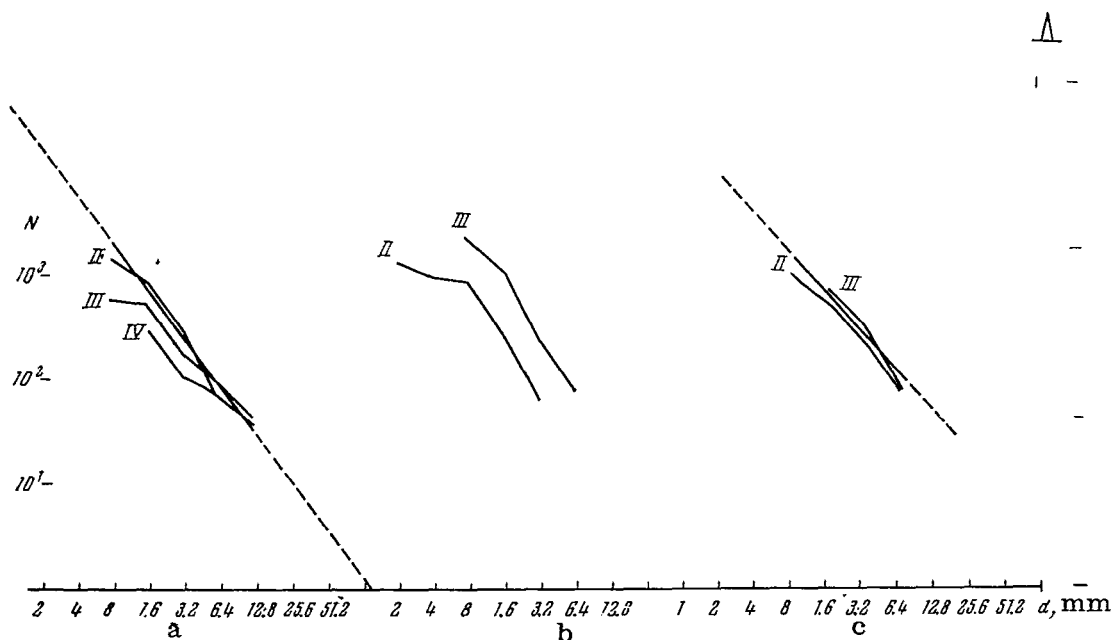
Figure 31 shows the average distribution of rocks from Luna-9, Luna-13 and Surveyor-1 data. Despite some differences in the line slopes, it is clear that the counts of rock density and their distribution by size are similar for all three examples.

The rock distribution in the area of the Luna-13 landing site was non-uniform, and numerous groups representing isolated accumulations are clearly visible, although they are difficult to characterize quantitatively due to the inadequate definition in depth of the panorama. By comparing two deposits of stones and the impoverished regions found under similar conditions of visibility near the horizon, we count 57, 19 and 49 stones included in equal angular intervals of visibility (Fig. 32, panorama V, 160°-190°). Reconstruction on the plan of the true shape of such accumulations is not possible. The clearly defined rock clusters on the horizon may also be seen in Fig. 33 (panorama II,

TABLE 5. Size Distribution of Rocks for Various Sectors

/61

Size of rock (cm)	Zone I; S = 6.16 m ²		Zone II; S = 8.17 m ²	
	number of rocks	concentra- tion per square meter	number of rocks	concentra- tion per square meter
1-3	50	8.1	68	8.3
3-5	17	2.8	29	3.6
5-10	8	1.3	6	0.8
10-15	1	0.2	1	0.1
15-20	—	—	1	0.1
Total	76	12.3	105	12.8

Figure 30. Size Distribution of Rocks as Selected by Inspection from the Luna-9 and Luna-13 Data (Referred to an Area of 100 m²).

Curve II - Considering Portions of the Panorama Distant 1-2 Meters from the TV Camera; Curve III - 2-3 Meters; Curve IV - 3-4 Meters.

a) Luna-13 ($\gamma = 150^\circ - 195^\circ$); b) Luna-13 ($\gamma = 330^\circ - 010^\circ$); c) Luna-9 ($\gamma = 140^\circ - 180^\circ$).

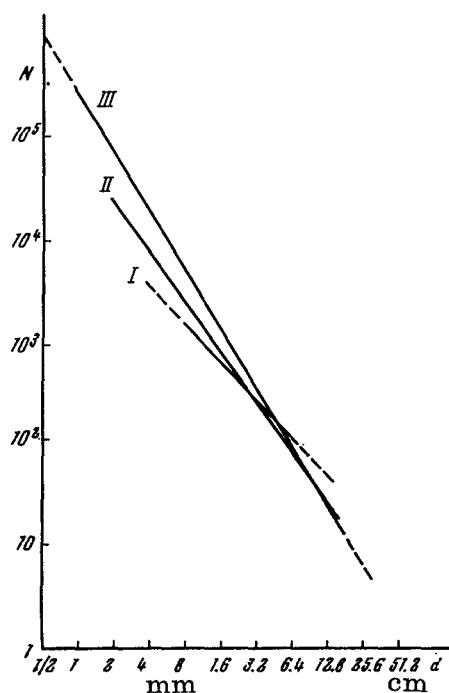


Figure 31. Size Distribution of Rocks in a 100 m² Area from Luna-9 Data (I), from Luna 13 (II) and Surveyor-1 (III).

six "freely-lying" rocks were counted, while there are 24 rocks lying snugly on the ground. The nature of the contact for the other rocks is not sufficiently clear. It is a curious note that the small hollow covered by a number of small irregularities (panorama V, 150°-160°, Fig. 16b), extending from the conspicuous rock in the foreground of the panorama plan (Fig. 16, rock 50) gives the impression of being a furrow possibly formed by a rocking motion of the rock over the surface, as is also shown on the topographical diagram.

The general nature of the rock surface is quite diverse; it is difficult to compare them because of the differing conditions of visibility of the rocks. We can note the rounded shapes of modified contours (Fig. 34, b, d), the irregular, small, step-like fractures (Fig. 34, a, c), the fine-toothed fracture along the crown of the above-mentioned rolling (?) stone in the foreground of the panorama (160°) and the apparently fresh rectangular cleavage surface of the rounded rock (Fig. 34c), with the fragments lying around it. One can deduce from an examination of this set that different rocks exhibit different stages of fracture freshness, or the processes acting on their surfaces have a long history. It is possible that the differing petrographic structures of the rocks plays a role here.

345°-005°). Individual clusters of rocks, for example the large rock in the left-hand portion of the panorama (150°) give a clear impression of having once been an isolated monolith that had broken into several pieces. What looks like repeated general fracture contours is visible on the frontal surface of three fragments (Fig. 34b), whose separations on the topographical plan may possibly be exaggerated.

Two types of juncture between stone and surface are noted. Most of the rocks have a rounded shape, tapering upward, and are in contact with the ground at the section having the largest perimeter (Fig. 34, c-d). It is quite unlikely that they are lying freely on the ground, as if on a flat base.

Rather, it can be thought that upward of half of the rock extends into the ground and its apex protrudes from the ground. Yet it is possible that some stones may be lying freely on the surface, in contact with the ground over a small area. Such stones are comparatively few (Fig. 35). Of the total number of 181 rocks in the zone of best visibility,



Figure 32. Rock-Clusters Visible on the Horizon (165° - 190°).

a - Panorama IV; b - Panorama V.



Figure 33. Clusters of Large Rocks on the Horizon. Panorama II (340° - 345°).

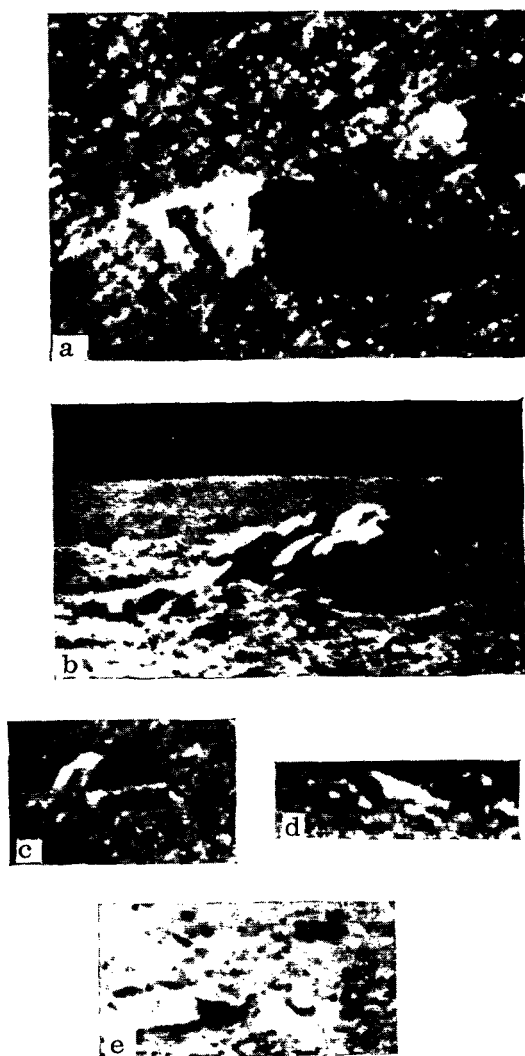


Figure 34. Various Types of Rocks on Panoramic Views.

a - Rock with Irregular, Acute-Angle Cleavages; Panorama IV (200° - 210°),
 b - a Group of Rocks Giving the Impression of a Splintered Monolith on the Surface; Panorama V (140° - 150°),
 c - a Rounded Rock with a Clear Acute-Angled Cleavage, Surrounded by Small Stones, Possibly Its Fragments; Panorama IV (200° - 205°), d - Irregular Stone with a Wide Base; Panorama II (355° - 360°),
 e - Bell-Shaped Protuberance on the Surface; Panorama I (290°).

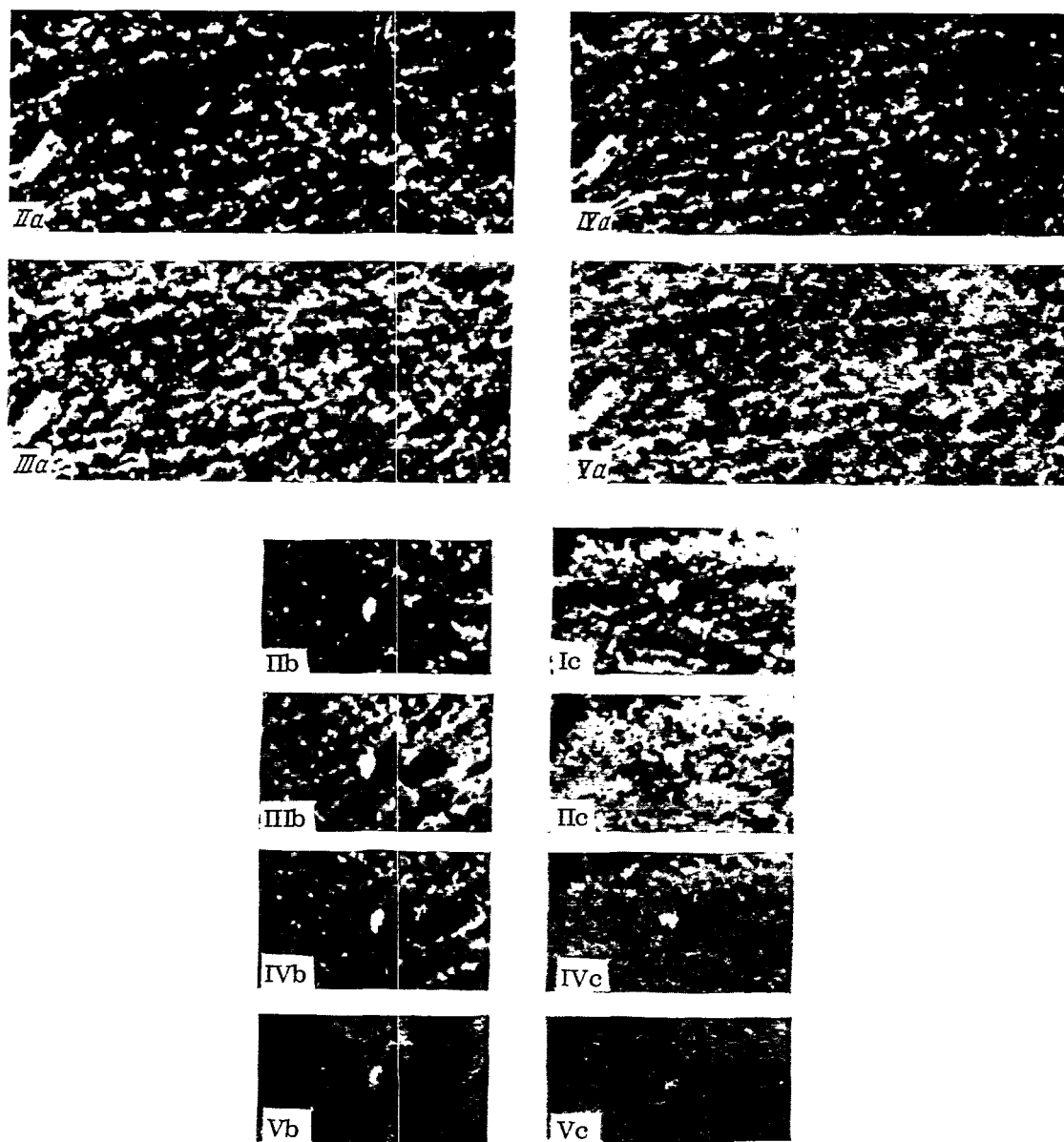


Figure 35. Stones Lying Freely on the Surface; their Shapes are Reproduced with a Different Solar Altitude.

a - a Small Depression, at the Bottom of which are Seen Two "Rolling" Pebbles; Panoramas II, III, IV, V (170° - 180°), b - Rounded Pebbles in the Foreground of the Panorama; II, III, IV, V (205° - 210°), c - Freely-Lying Stone; Panoramas I, II, III, V (320°).

Possible petrographic inhomogeneity, whose nature remains obscure, is also indicated by the diverse coloration of certain of the rocks. For example, we can single out the dark rock (Fig. 16, 307°, stone 23; Fig. 37 on the first plan).

/67

The shape features of the bell-shaped rock (Fig. 34, panorama I, 290°) are very interesting; this rock appears to be growing out of the ground. Its enlarged base may be interpreted in different ways, but there is reason to consider the overall nature of the relief as erosive, with a negative balance of matter, as noted earlier for the Luna-9 landing site.

Nodules. As discussed in the description of the Luna-9 panoramas, the general lack of a structureless, dust-like layer of soil on the surface, which is subject to the action of a number of disruptive forces, is already conducive to assuming a nodular structure of the fragmented layer of soil. A comparison of the microstructure of the surface and of the sizes of the circular craterlets leads to the assumption that the prevailing size of the nodules is 1-2 cm. It is particularly interesting to trace out mechanical effects easily able to break down the nodular structures.

We must not neglect the right-hand portion of the panorama (285°-310°), where two regions are seen with surface changes indicative of a breakdown of the nodular structure. Both regions preserve their configuration under different lighting conditions, so that various details of the structure are observable.

The first of these areas (Fig. 36) lies immediately below the rim II, where surface layer slippage may be assumed (285°-310°). It appears as a triangular formation, approximately the same size as a lobe of the probe. Panorama II shows the fine-nodular structure of the ground along the edges of the formation and the smooth surface inside. On panorama II it is seen that the entire inner surface is not smooth, and panorama V shows the triangular formation to best advantage.

If this information is actually the impression of a lobe, the depth of the loose layer at this location can be estimated as being several centimeters in depth, which is in good agreement with the penetrometer determination of ground solidity and the depth of the bend of the side of the central depression (see Fig. 37). The generally nodular structure of the ground and the bright smooth area to the right of the radiation densimeter and which reproduces its contour are seen in Fig. 37 (310°). This is not a solar hot-spot since the general contour of the impression remains unchanged for different solar sunrise angles. On the smoothed surface area of panorama III we see the complex shadow of the nodules lying on its edge, which emphasize the sharp boundaries of the trace and the complexity of the undisturbed surface.

/69

It should be noted that the individual probe components visible in some sections of the panorama are extremely light in weight and cannot give a measure of the solidity of the lunar soil.

The overall analysis of the data from Luna-13 confirms the results from Luna-9, both as regards the macroscopic morphological details of the lunar

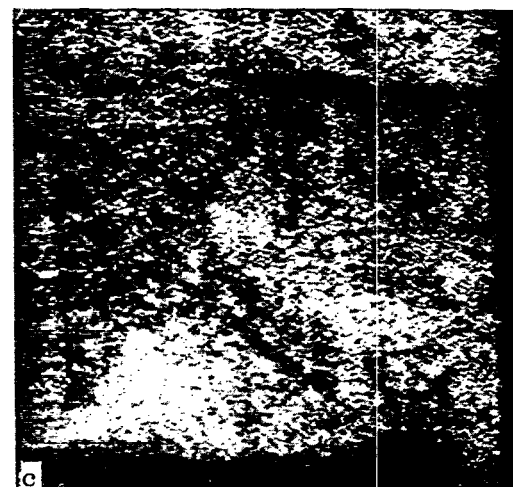


Figure 36. Nodular Structure of the Ground and its Breakdown (280° – 295°):

a - Panorama II, b - III, c-V.

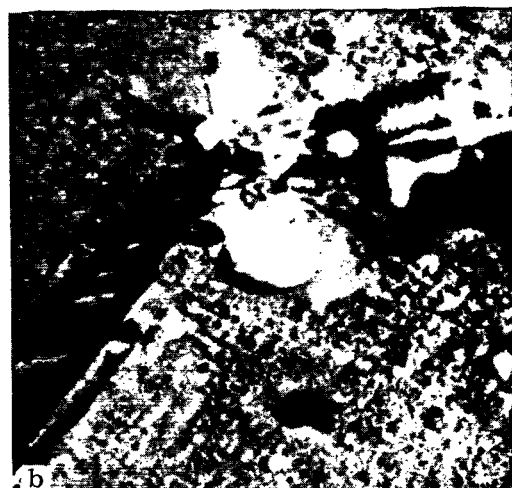
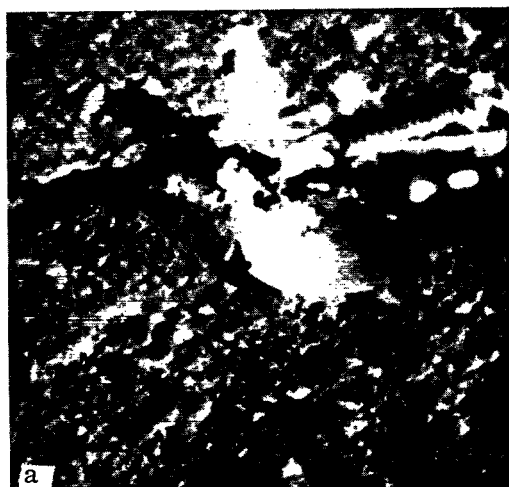


Figure 37. Ground Structure Break-down by the Action of the Radiation Densimeter (300° - 315°).

a - Panorama II, b - III, c-V.

surface and with respect to the spongy-nodular microstructures of the surface (Fig. 38). However, in considering this picture, which shows a portion of the panorama as a rectified plane picture, it should be kept in mind that there is some linear distortion of the contours of details in the upper portion due to distortions arising in the rectification process which do not reflect the true properties of the ground structure. Direct determinations of the density and solidity of the ground are in agreement with the qualitative estimates obtained from the panorama and confirm the earlier deduction as to the low strength of an immediate surface layer of the order of several centimeters in thickness.

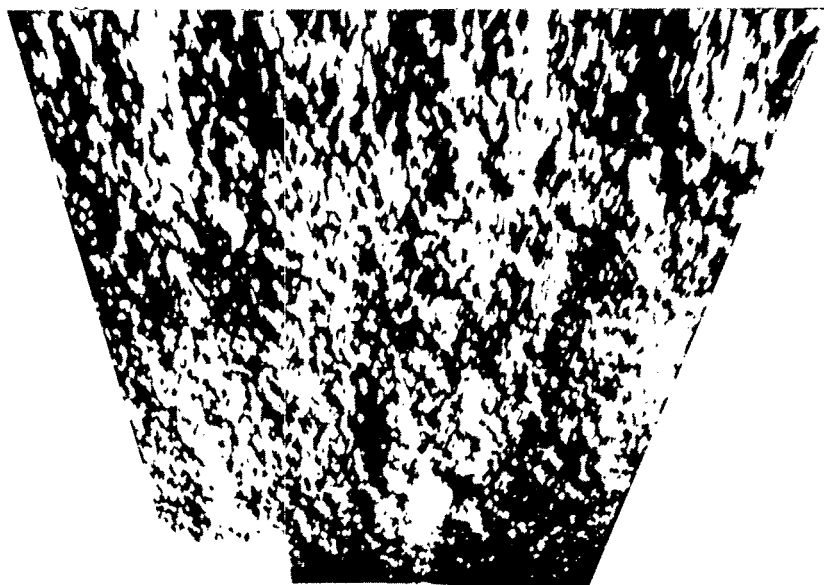


Figure 38. Rectified Plan View of a Section of the Surface on the Luna-13 Panorama. Scale 1:12. The Elongation of Details in the Upper Portion of the Picture is Due to the Rectification Conditions.

At the same time the interpretation of the Luna-13 results obviously does not allow excluding the possibility of "landslide" phenomena, perhaps related to a fragmentary, weakly-bound structure of the underlying layer in certain areas of the lunar surface.

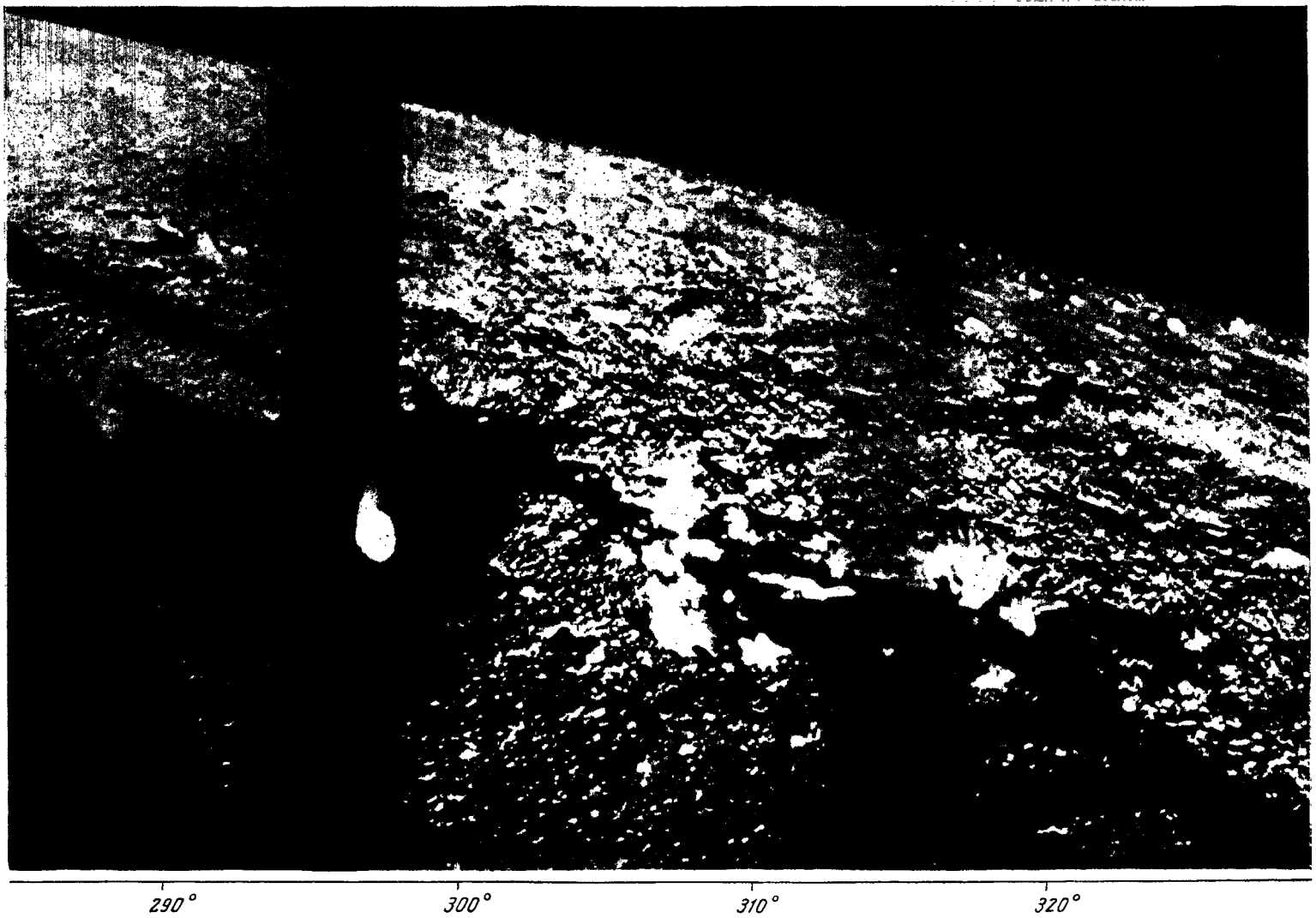
Owing to the widespread presence of craters and small depressions of various sizes and in various stages of breakdown over the entire lunar surface, it can be assumed that the structure of the inner slopes of small formations having small slope angles differs little in general from the average surface structure and may be taken as typical.

PART III
PANORAMIC PHOTOGRAPHS
OF THE LUNAR SURFACE

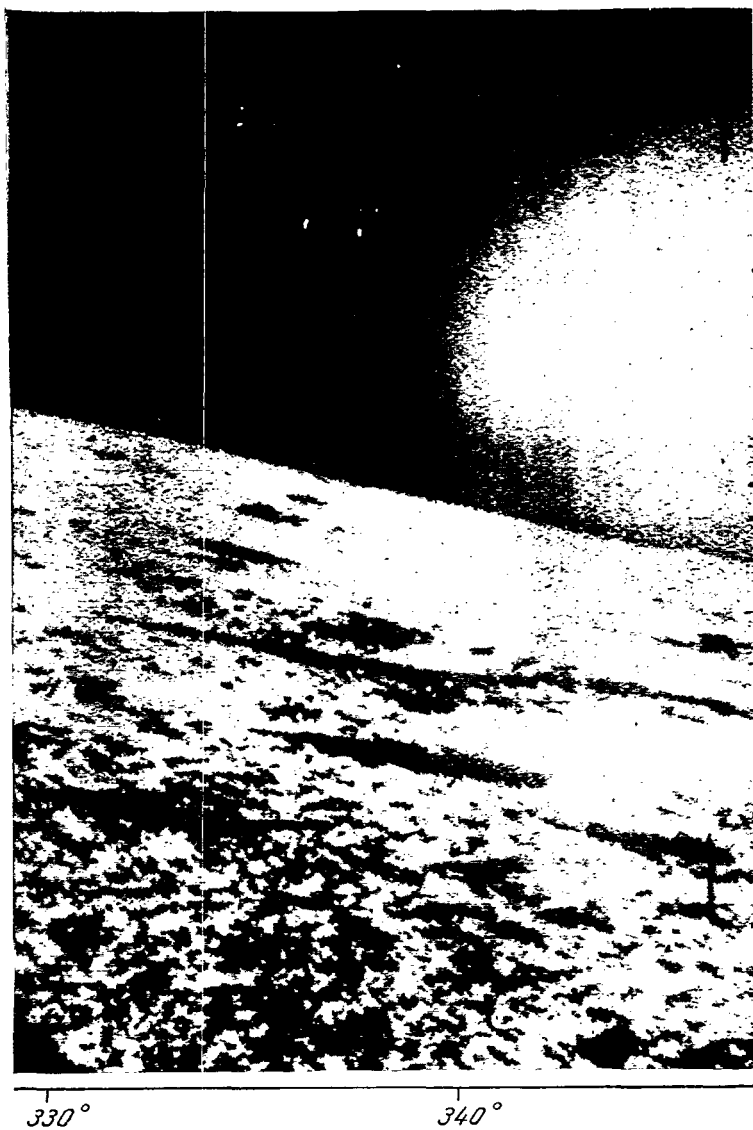
PANORAMA I, Fragments 1-2
PANORAMA II, Fragments 1-7
PANORAMA III, Fragments 1-7
PANORAMA IV, Fragments 1-4
PANORAMA V, Fragments 1-7
PANORAMA II, III, V
TOPOGRAPHICAL PLAN OF THE LANDING SITE
TOPOGRAPHICAL DIAGRAM OF THE LANDING SITE

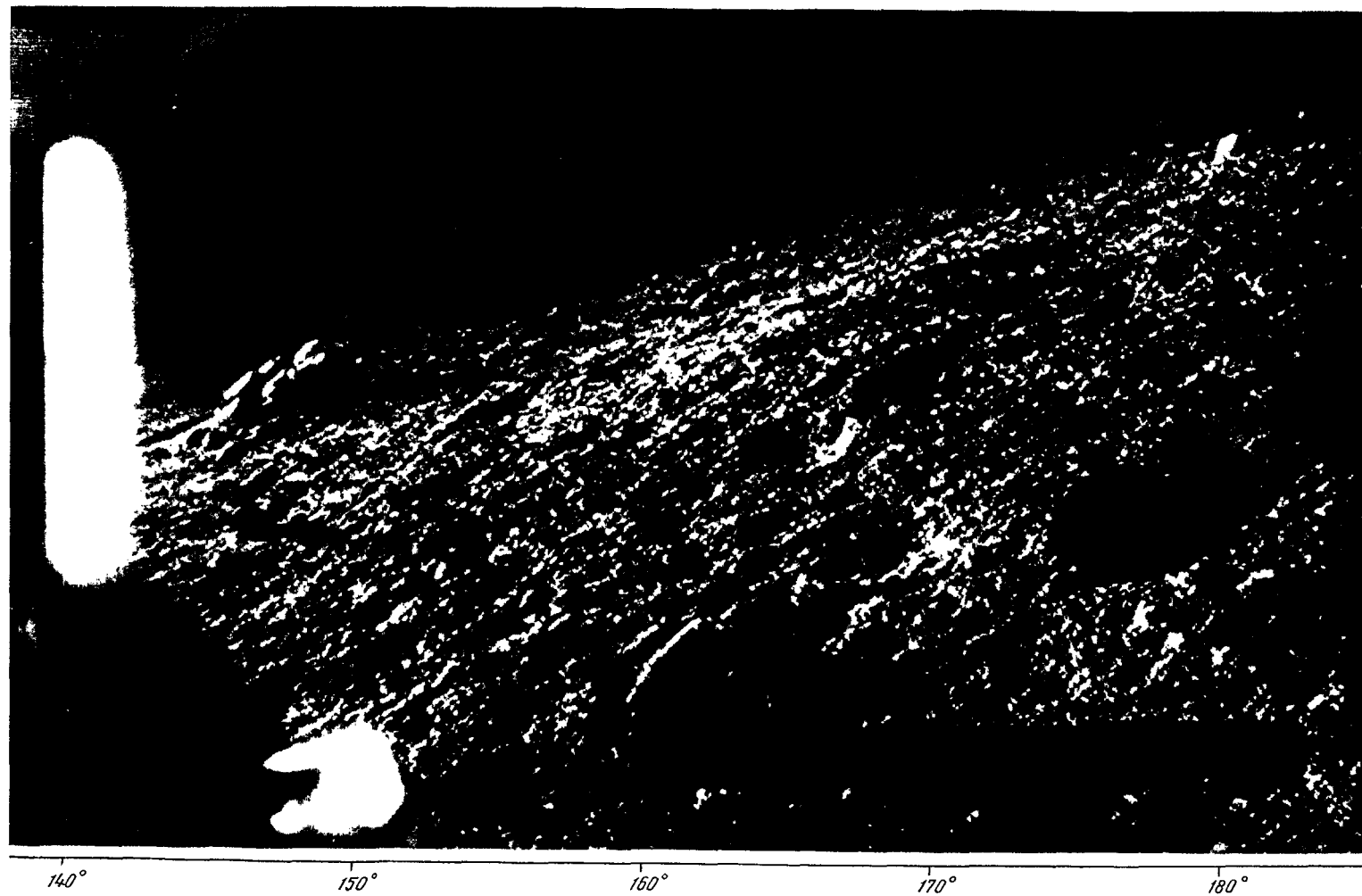
Panorama I, Fragment 1

Luna-13

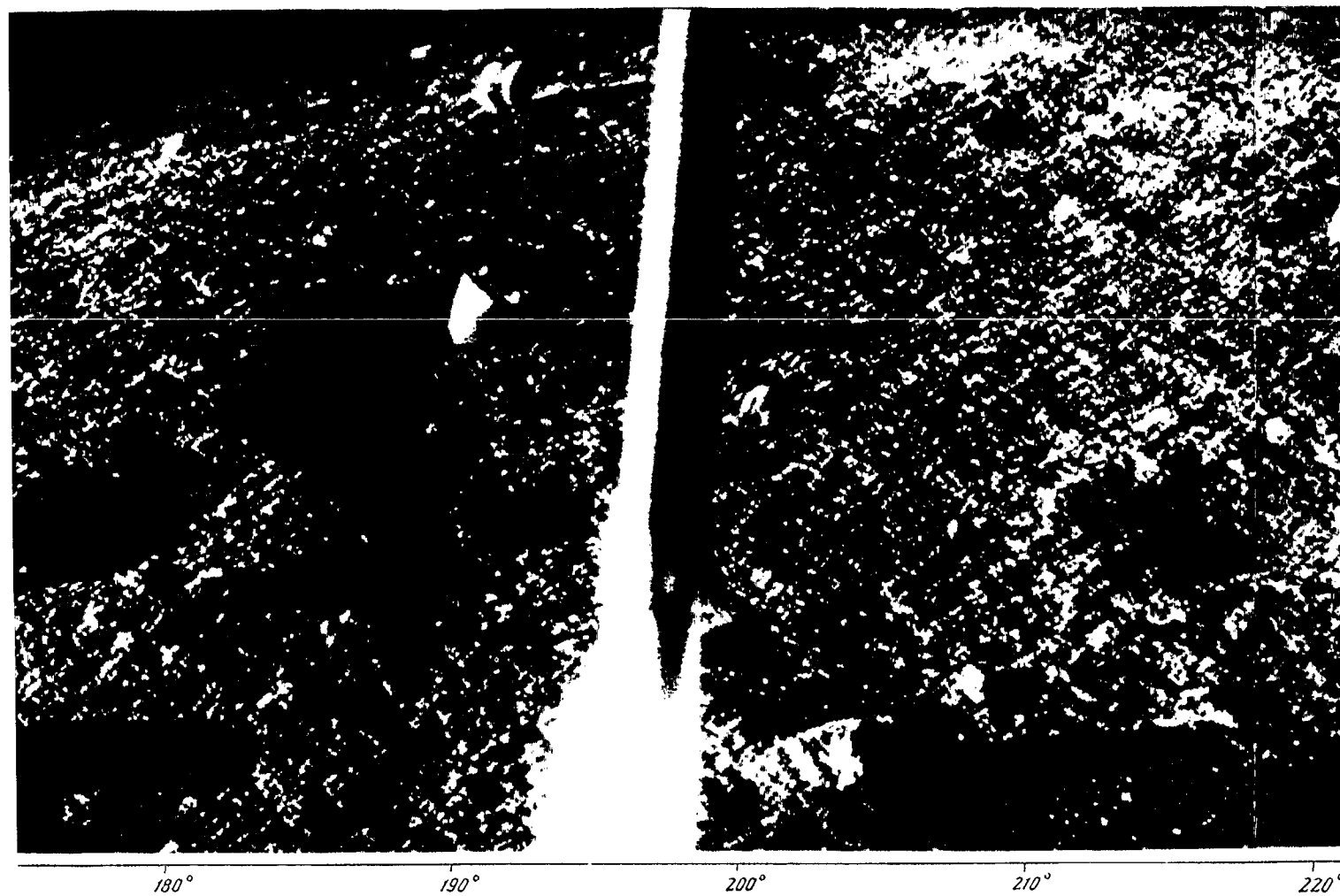


Panorama I, Fragment 2

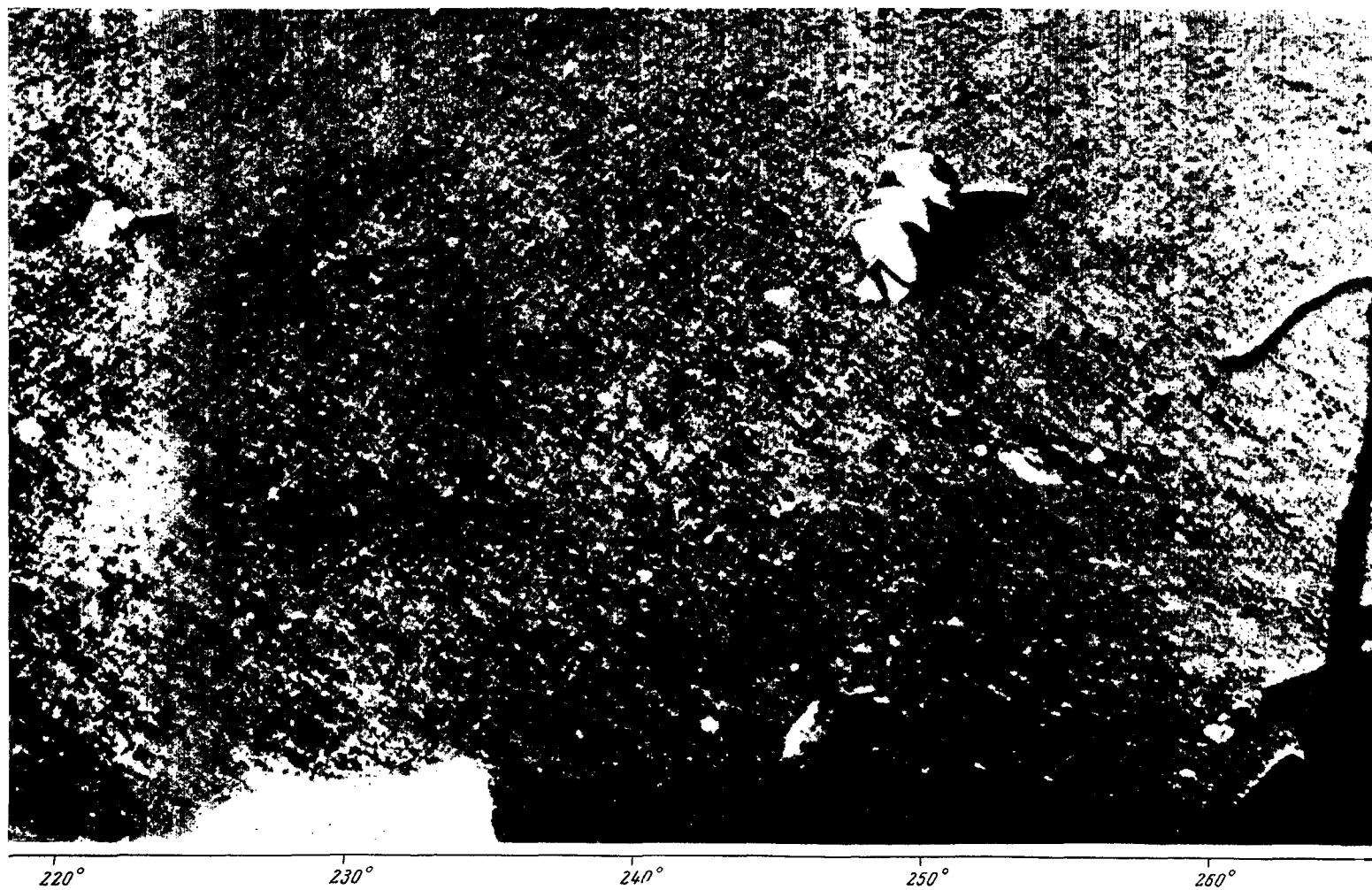




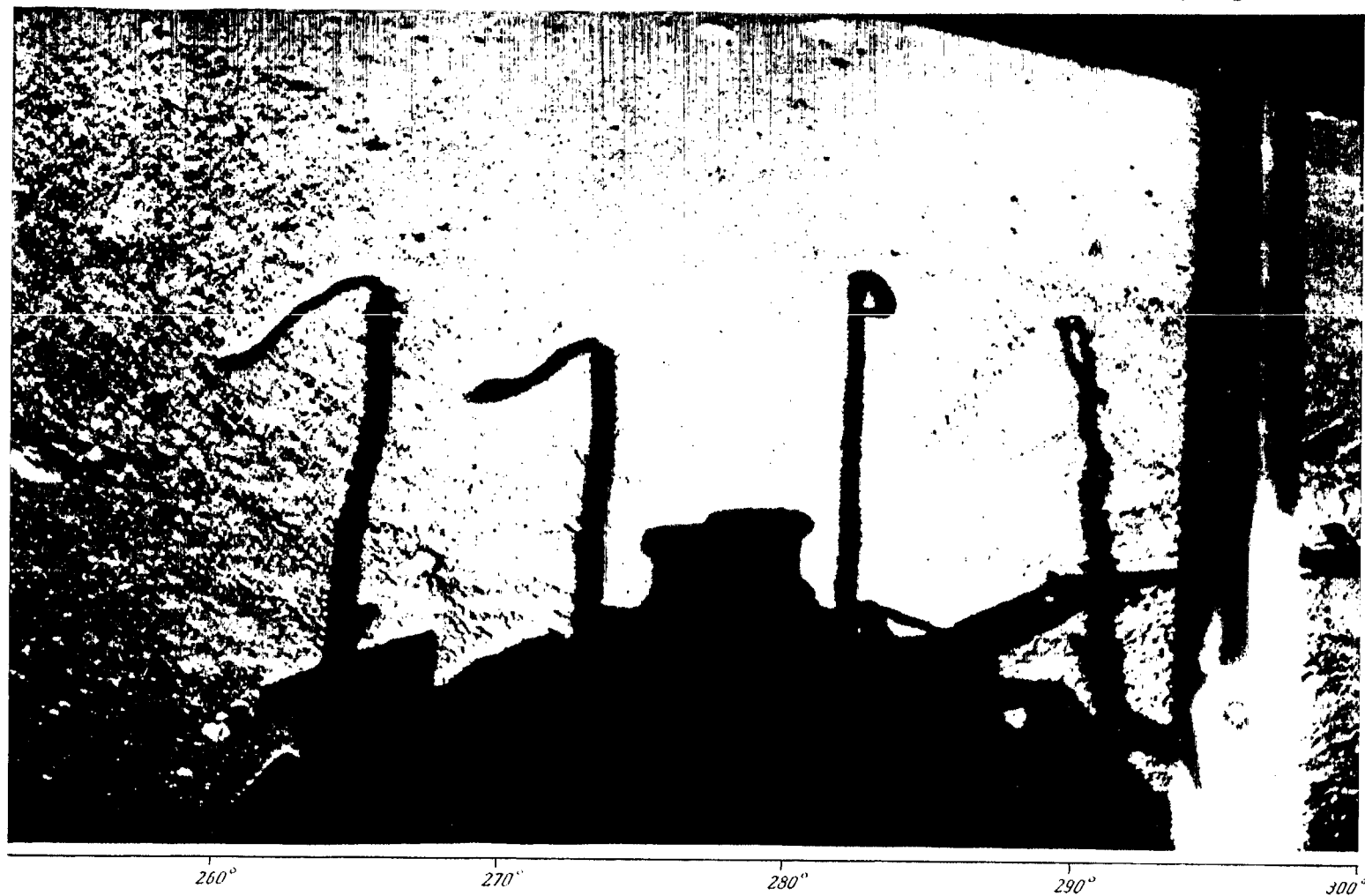
Panorama II, Fragment 2



Panorama II, Fragment 3

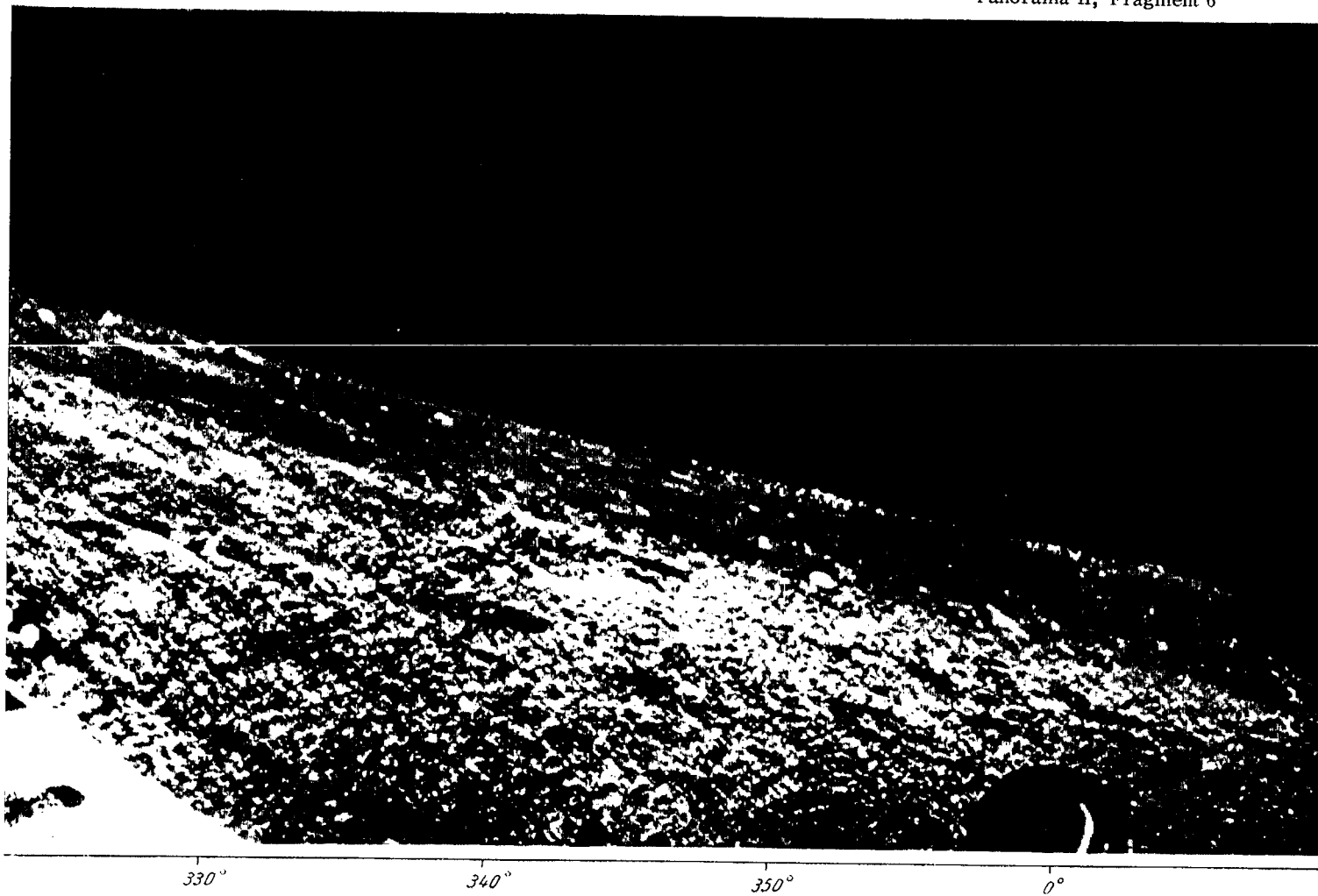


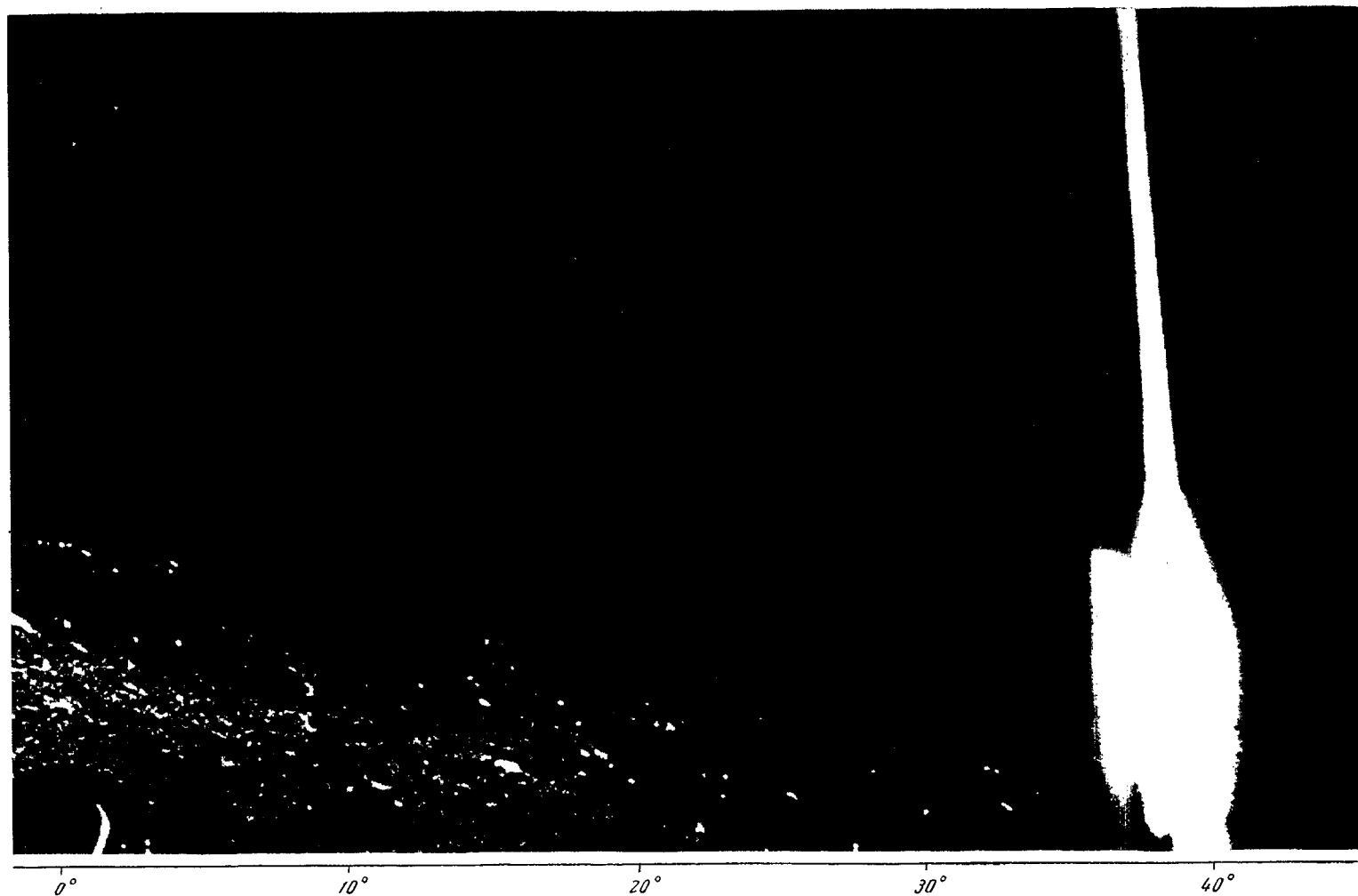
Panorama II, Fragment 4



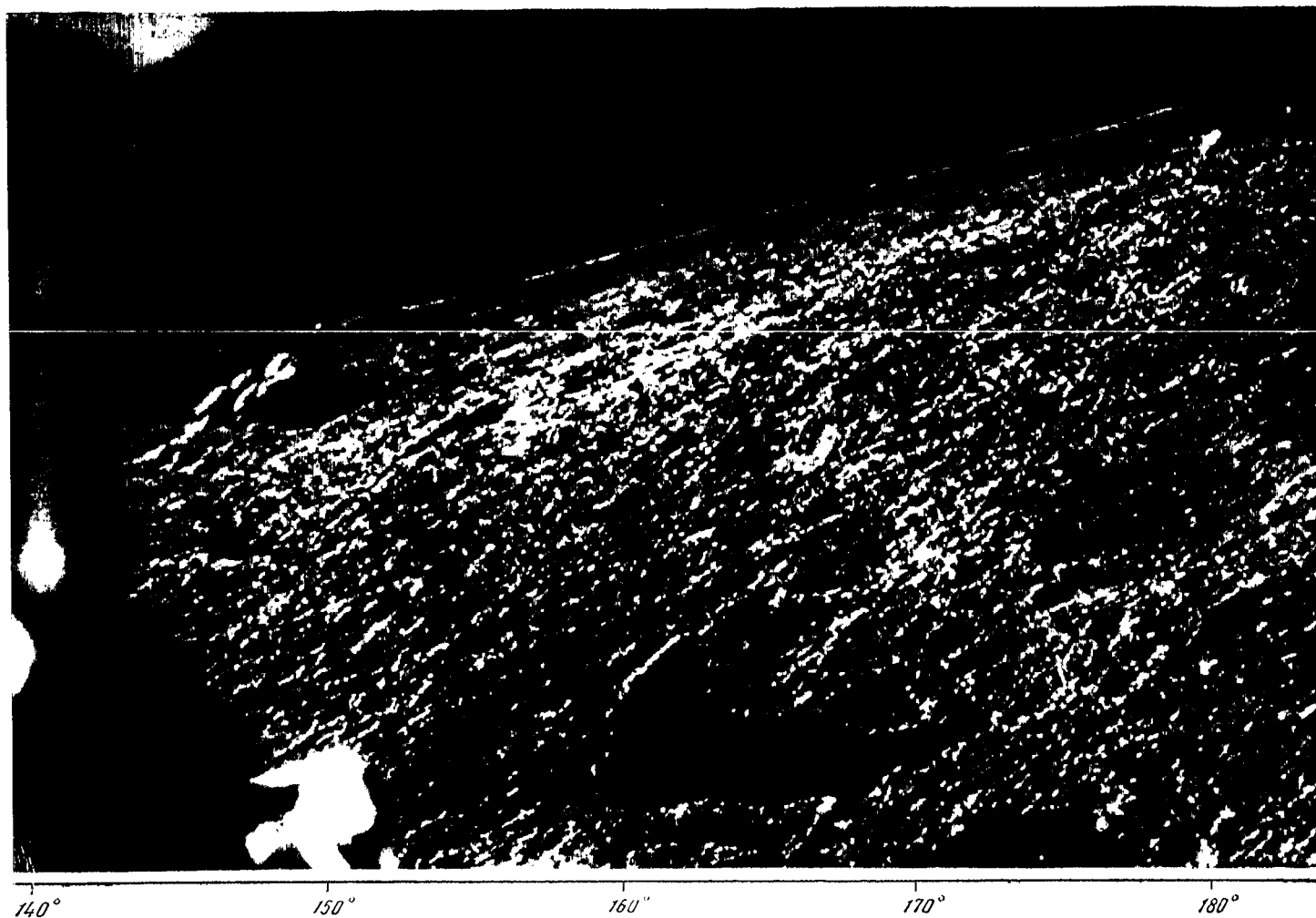


Panorama II, Fragment 6

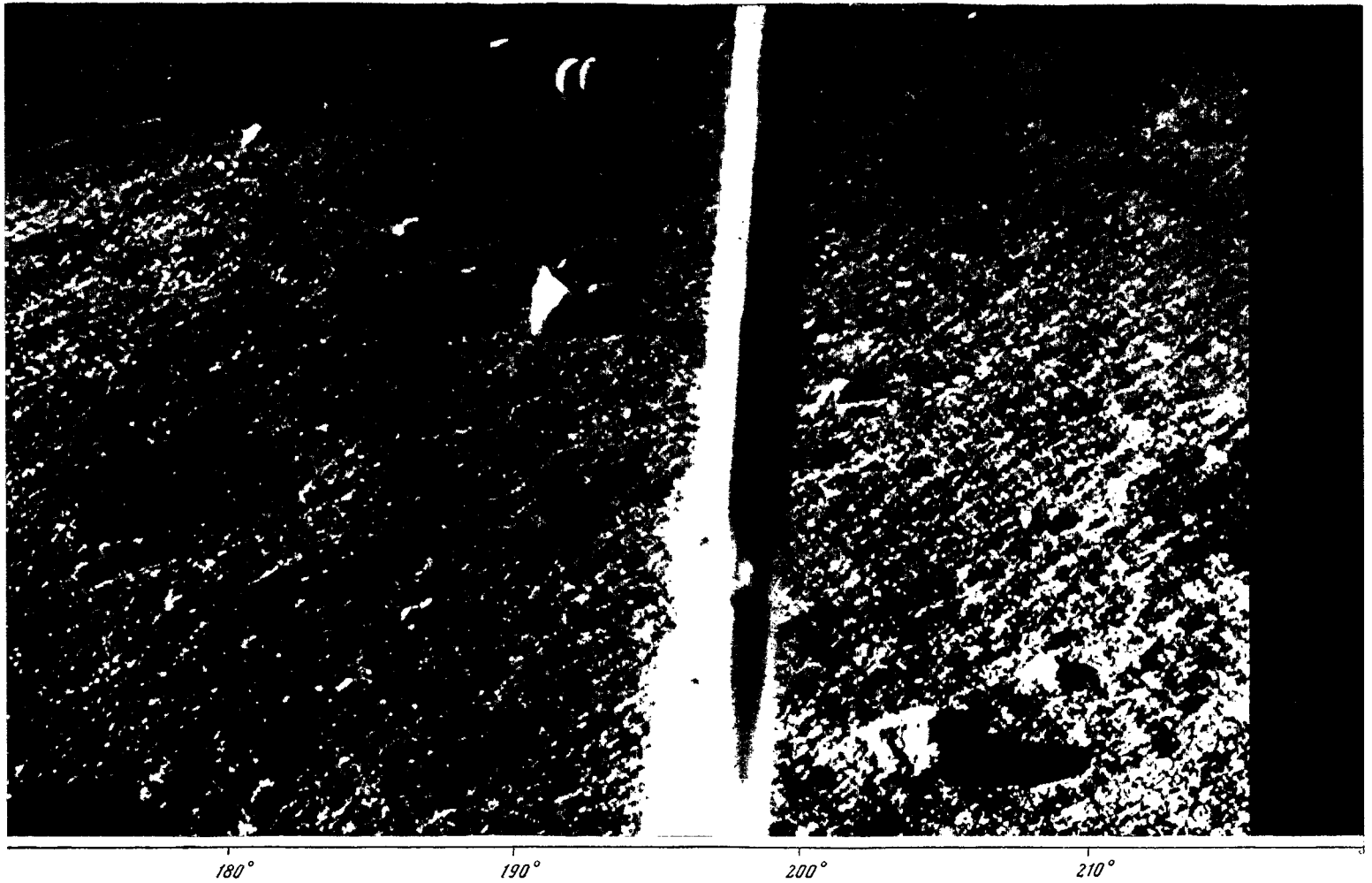




Panorama III, Fragment 1



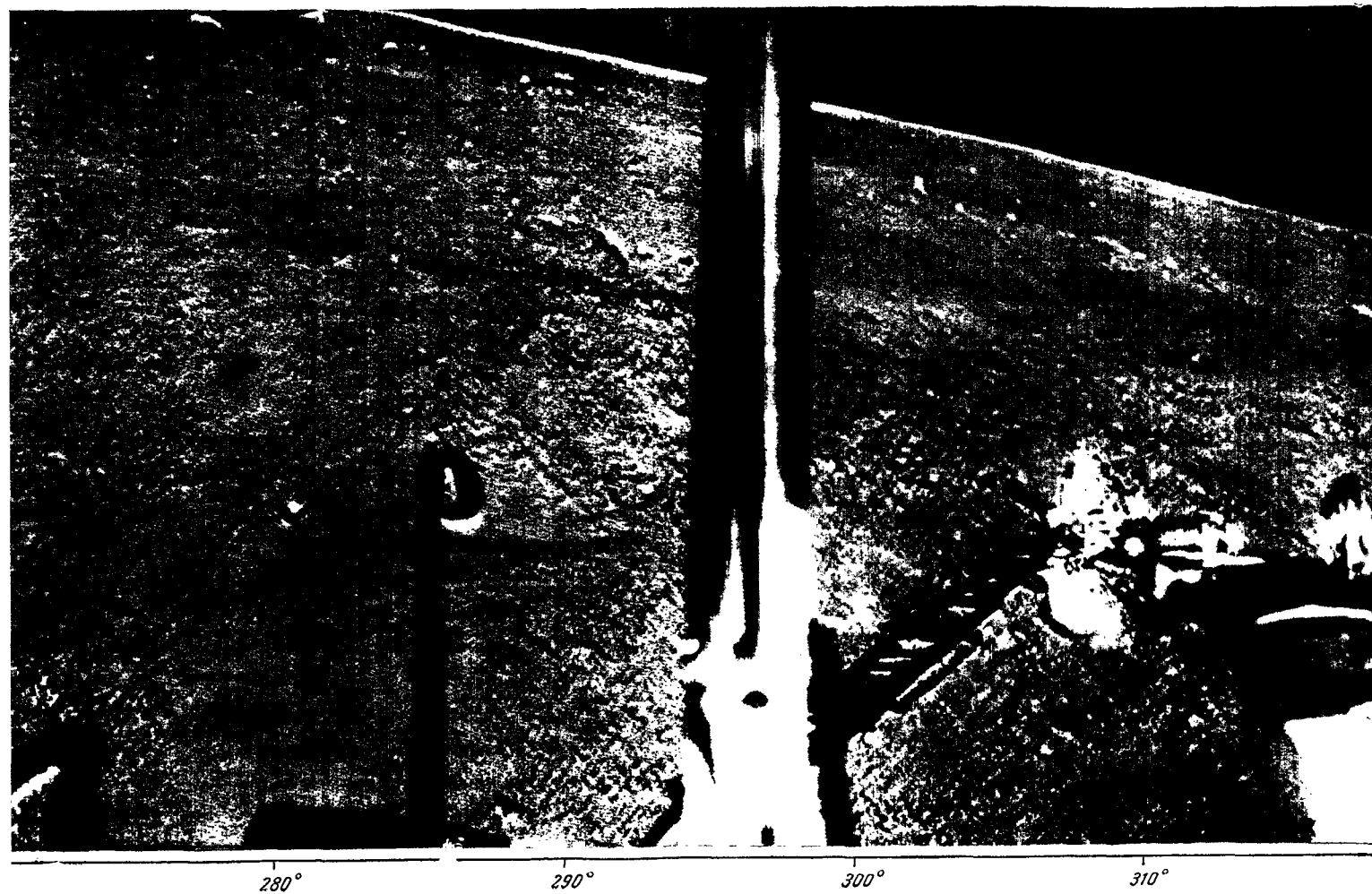
Panorama III, Fragment 2



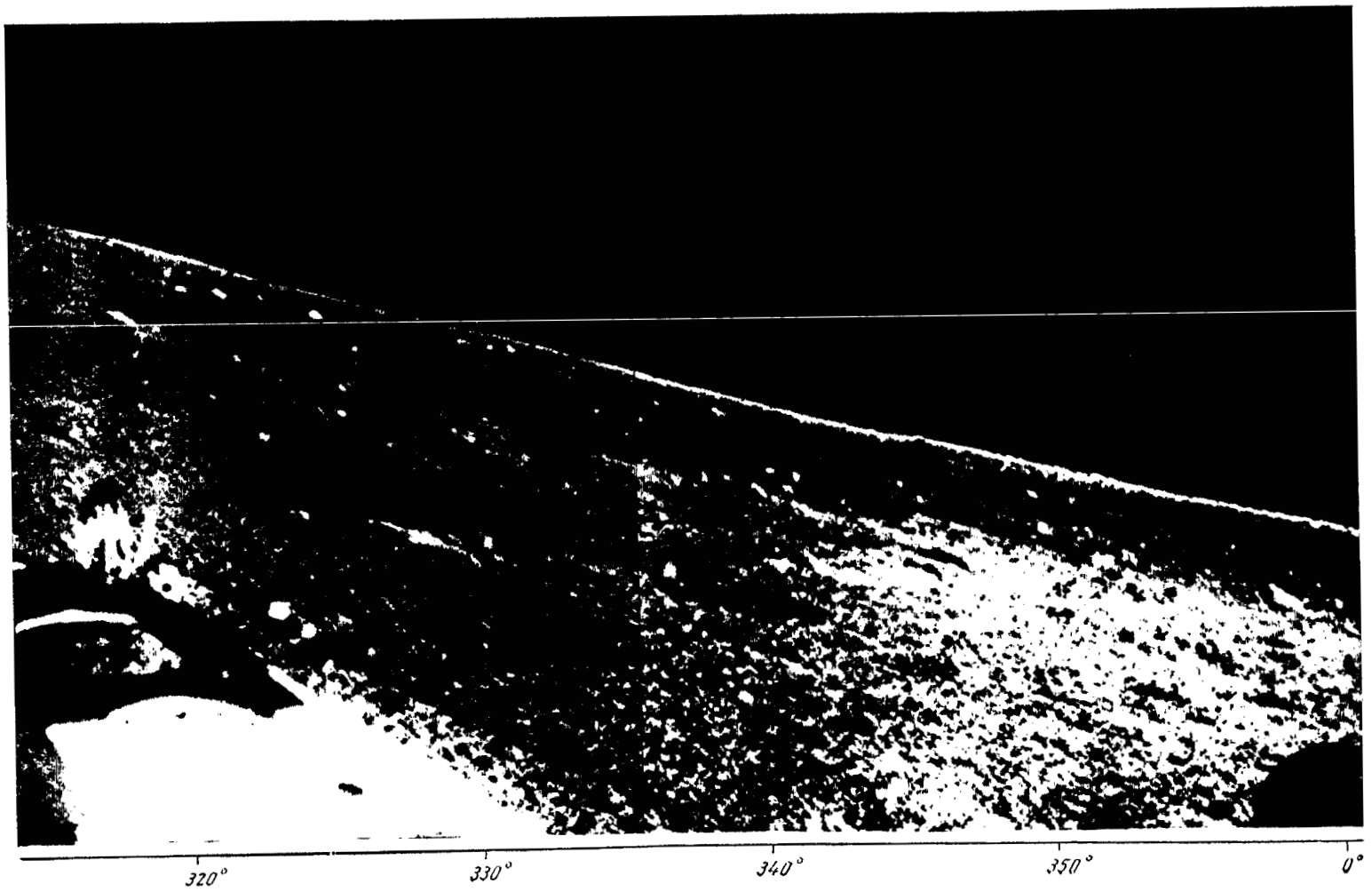
Panorama III, Fragment 3



Panorama III, Fragment 4

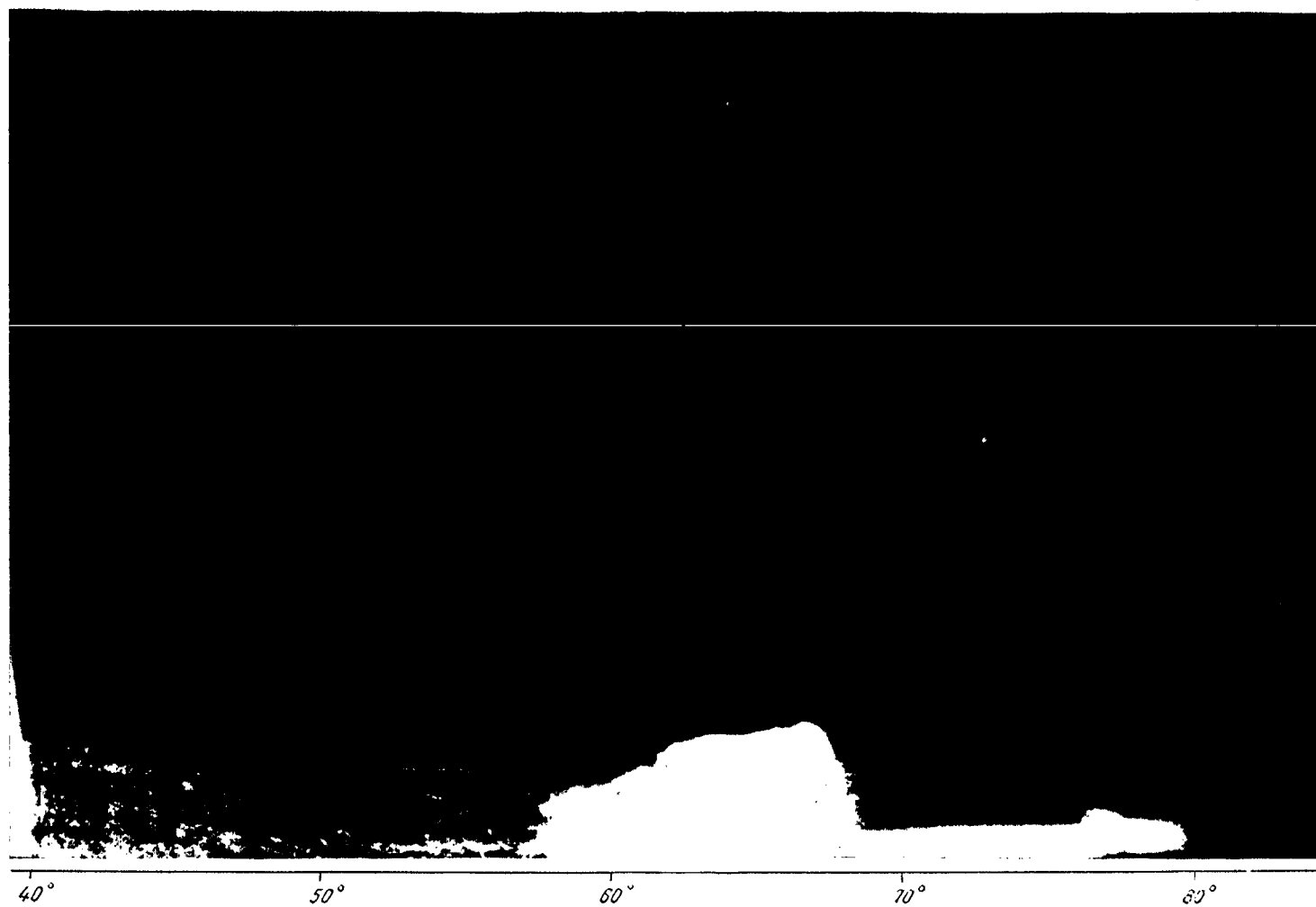


Panorama III, Fragment 5

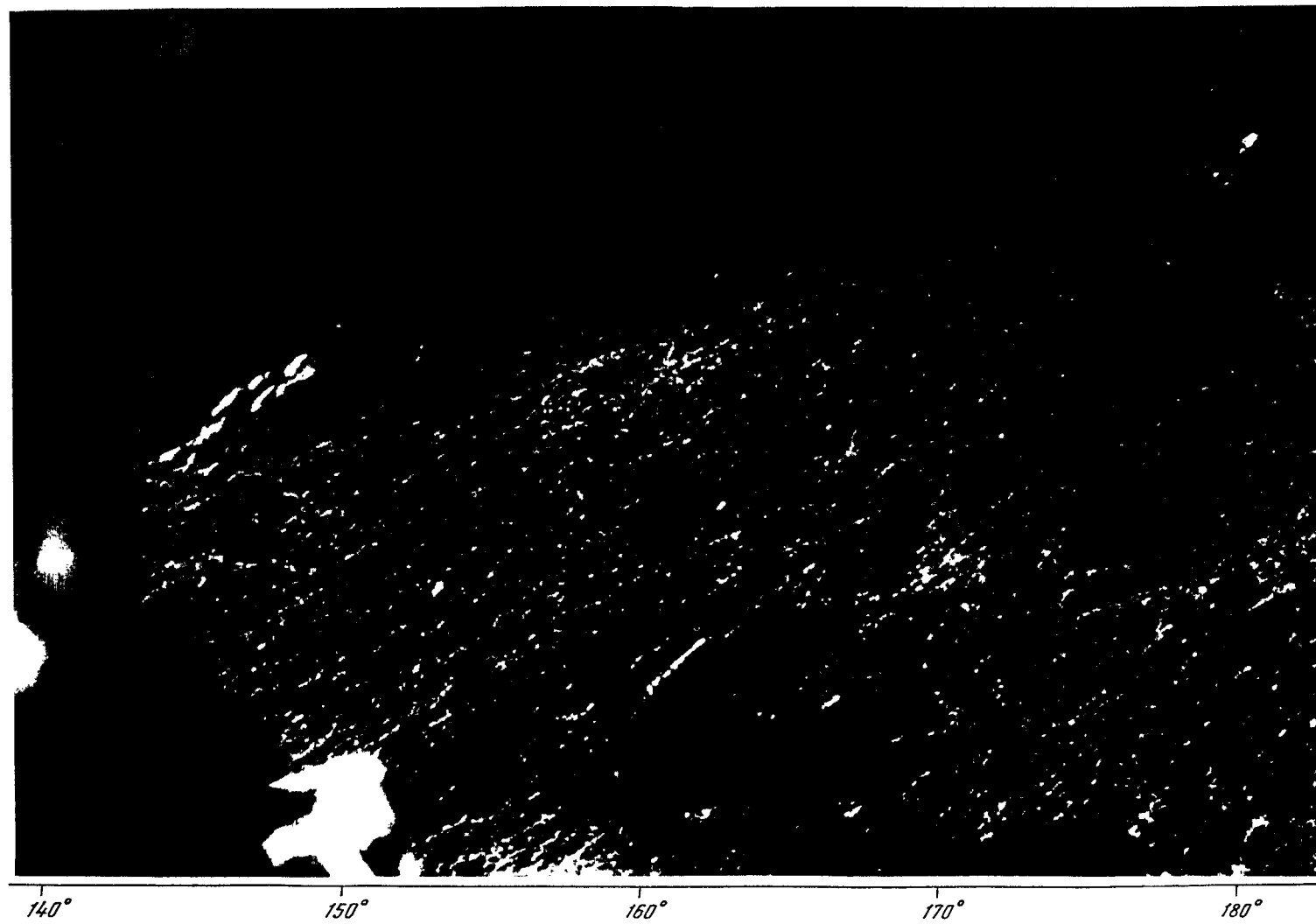




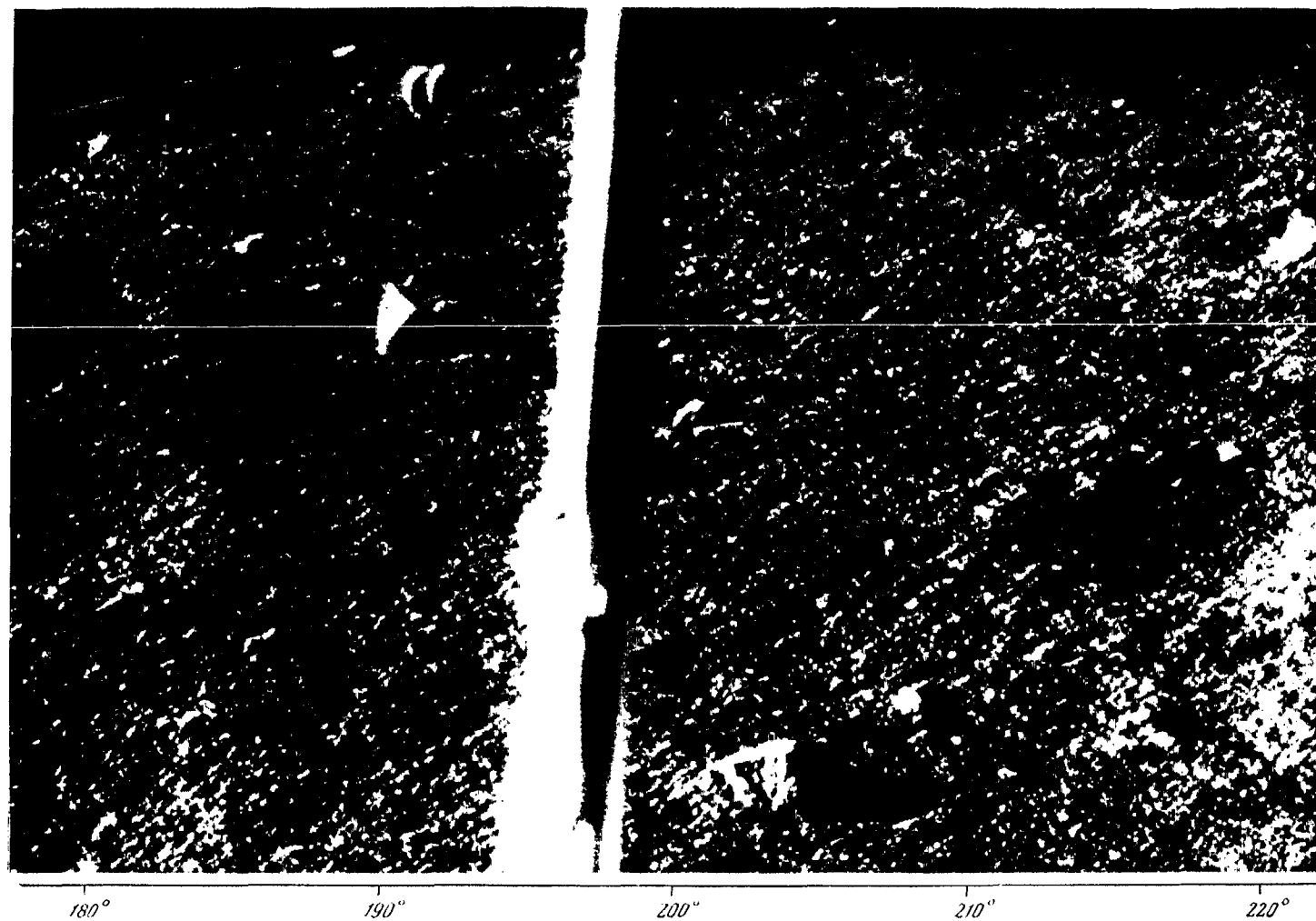
Panorama III, Fragment 7



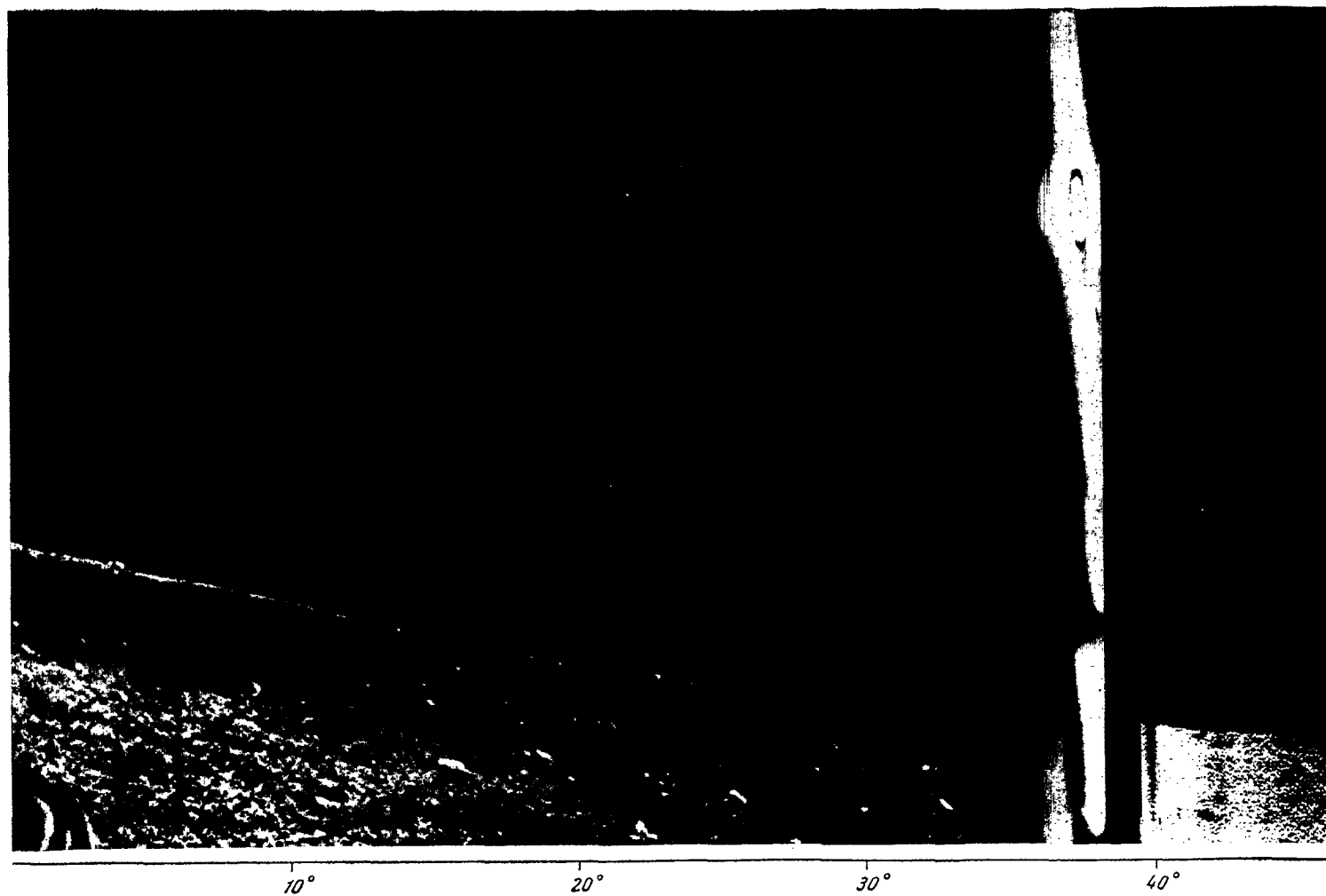
Panorama IV, Fragment 1



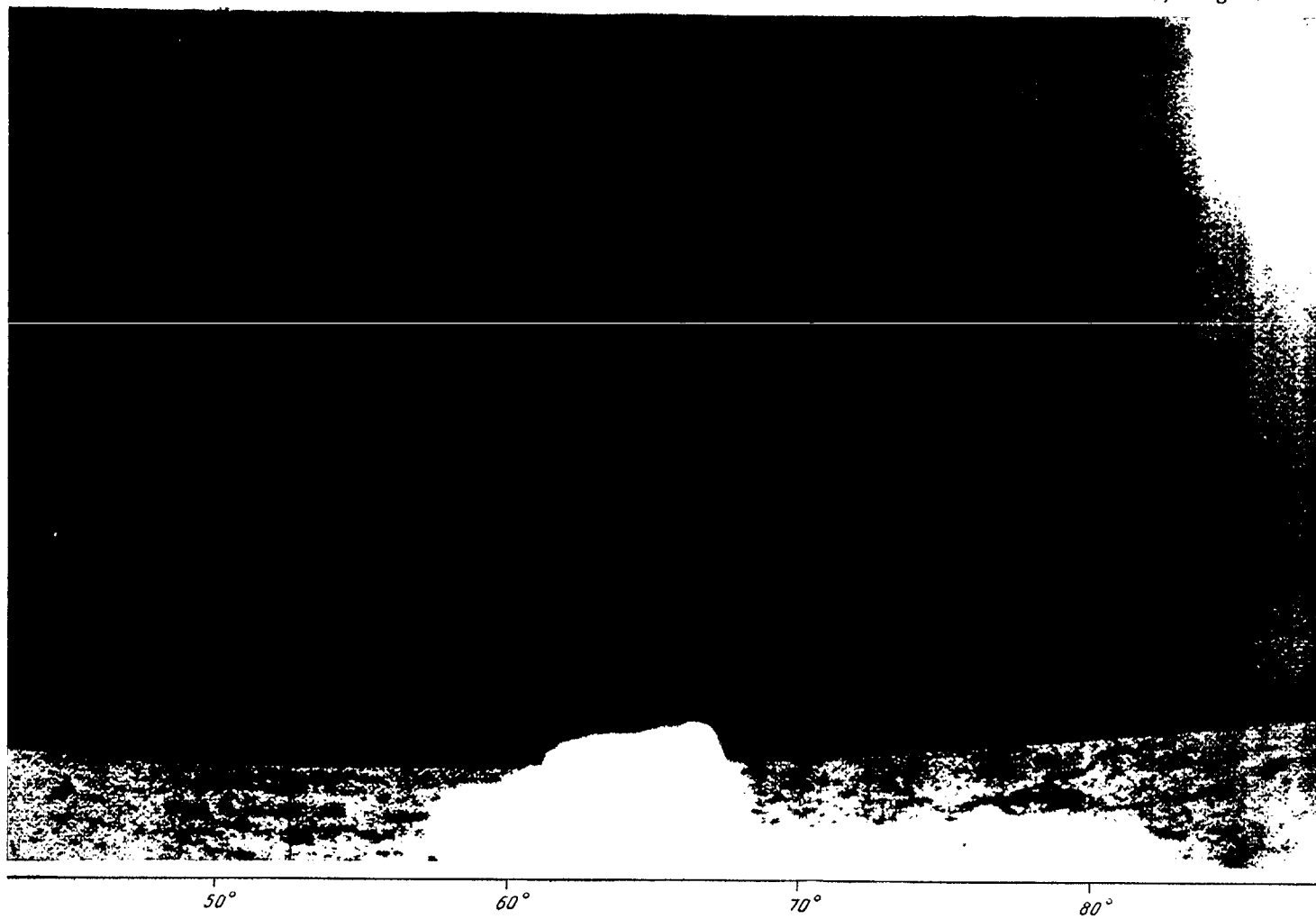
Panorama IV, Fragment 2



Panorama IV, Fragment 3

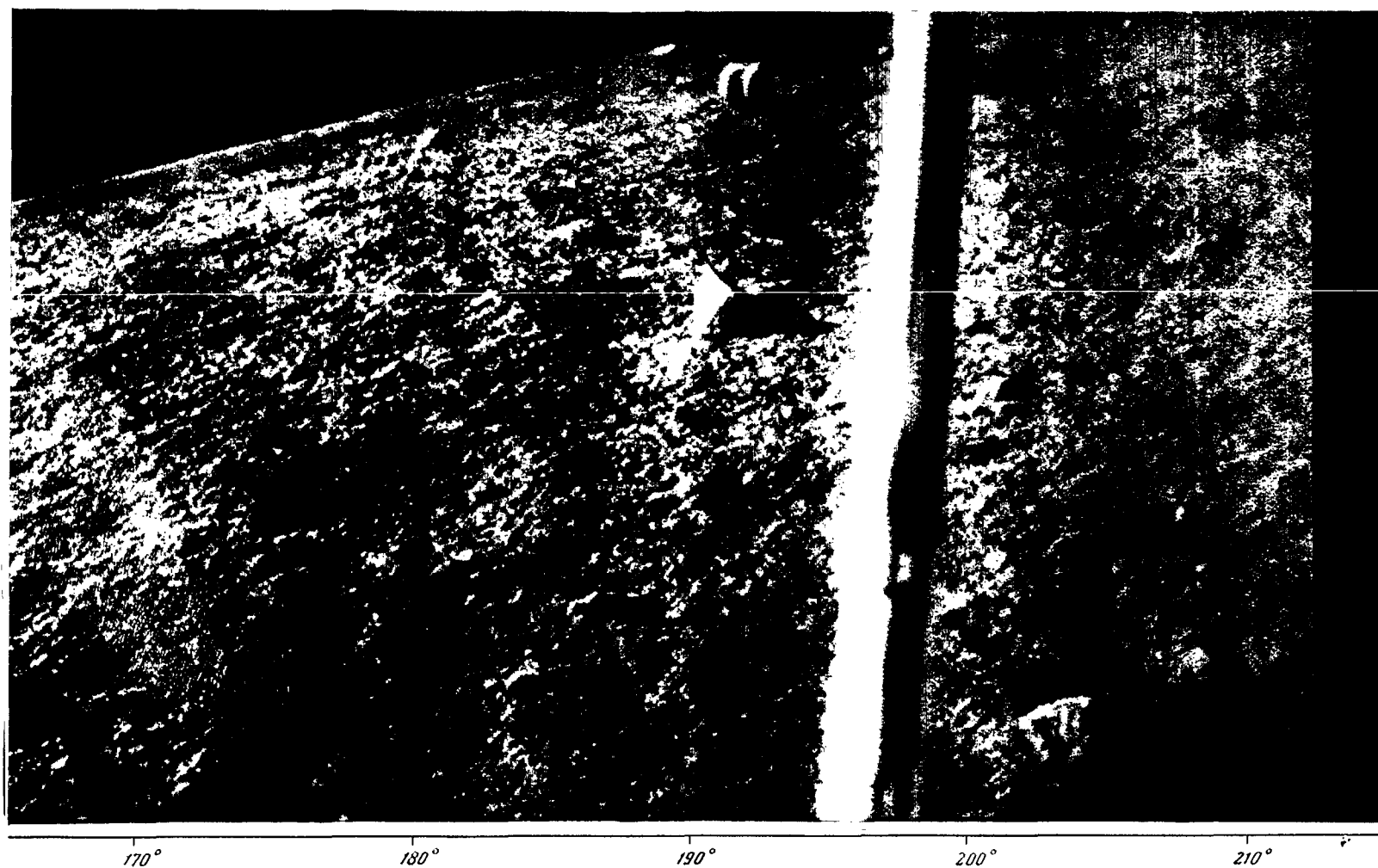


Panorama IV, Fragment 4





Panorama V, Fragment 2

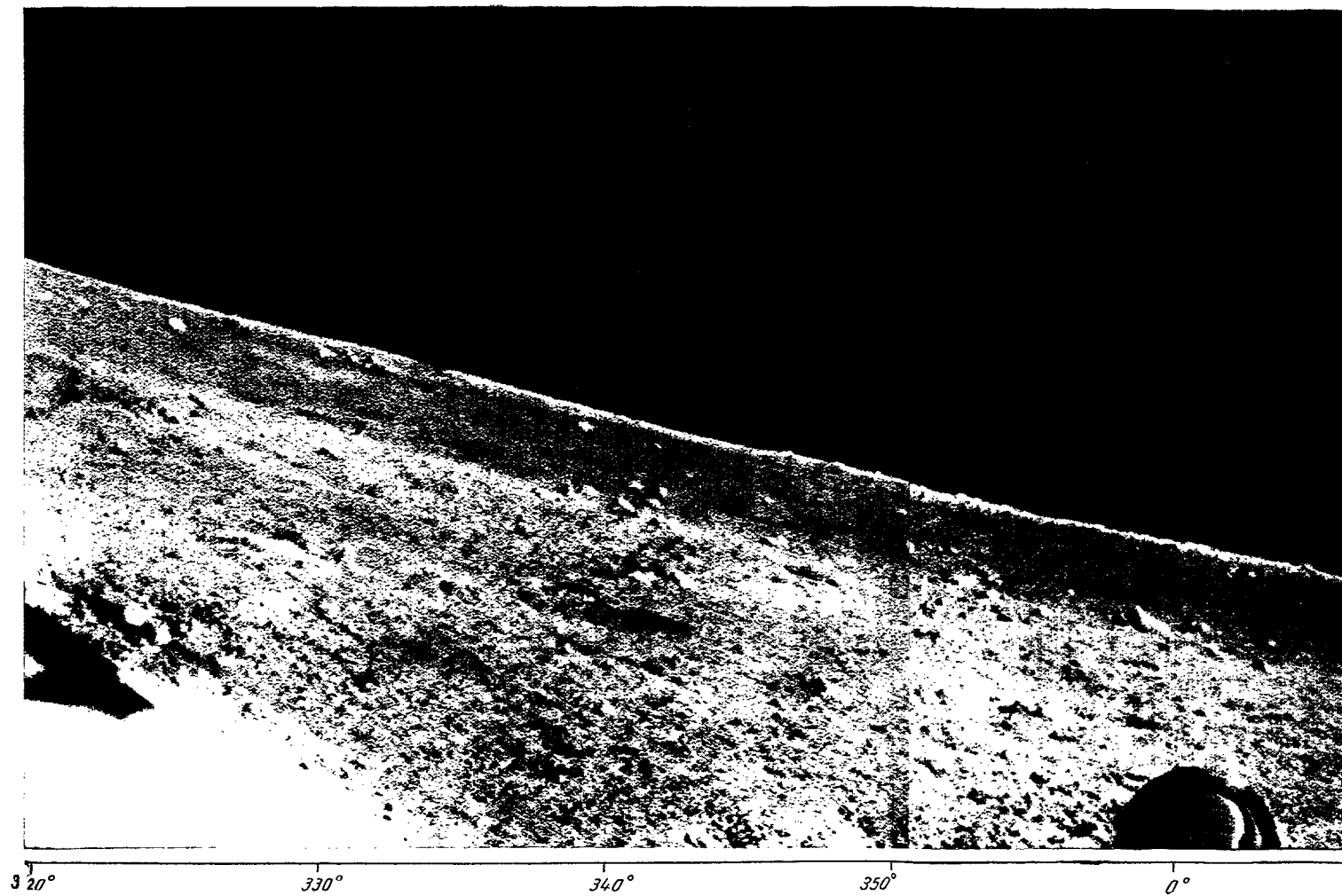




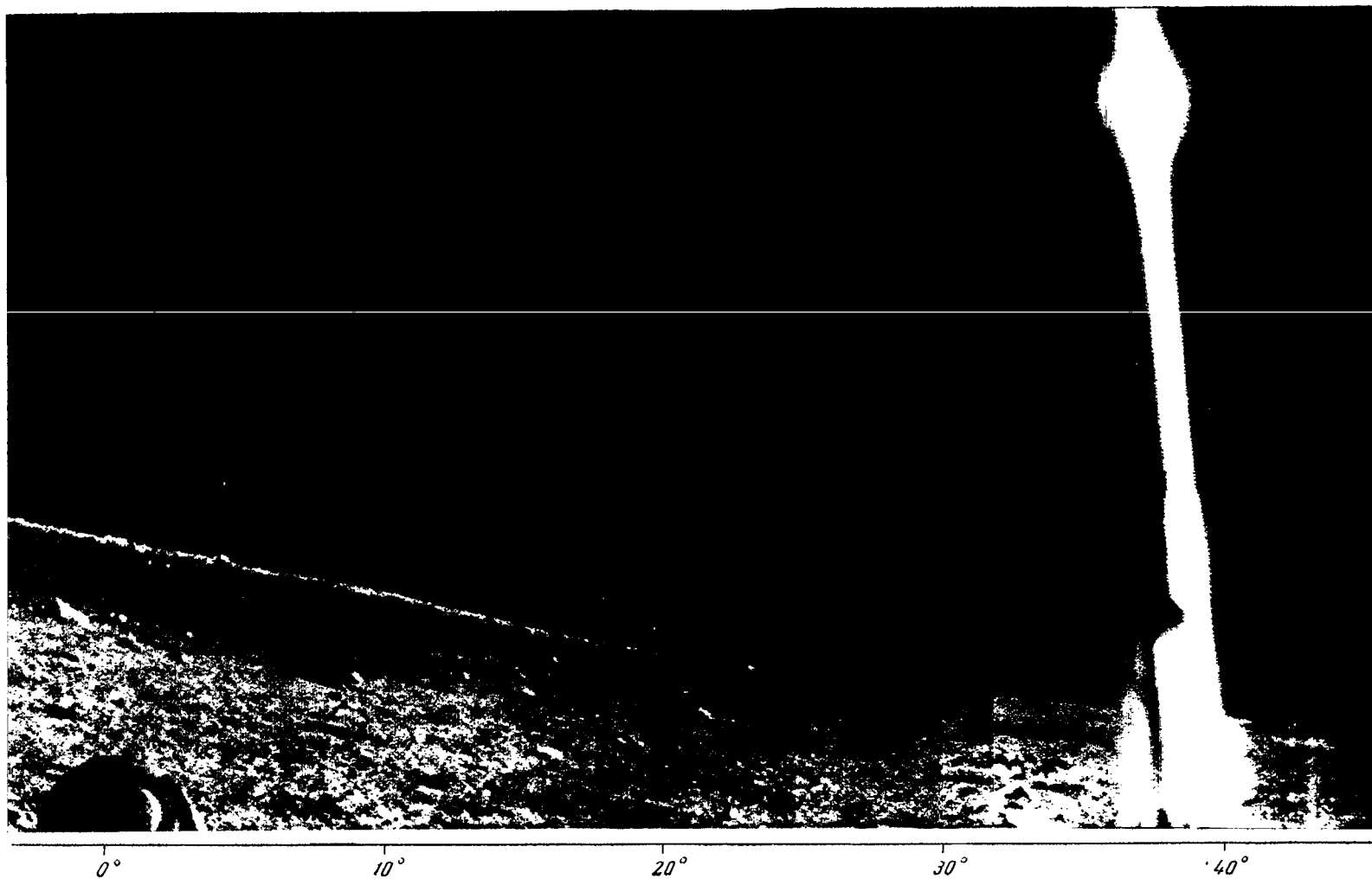
Panorama V, Fragment 4

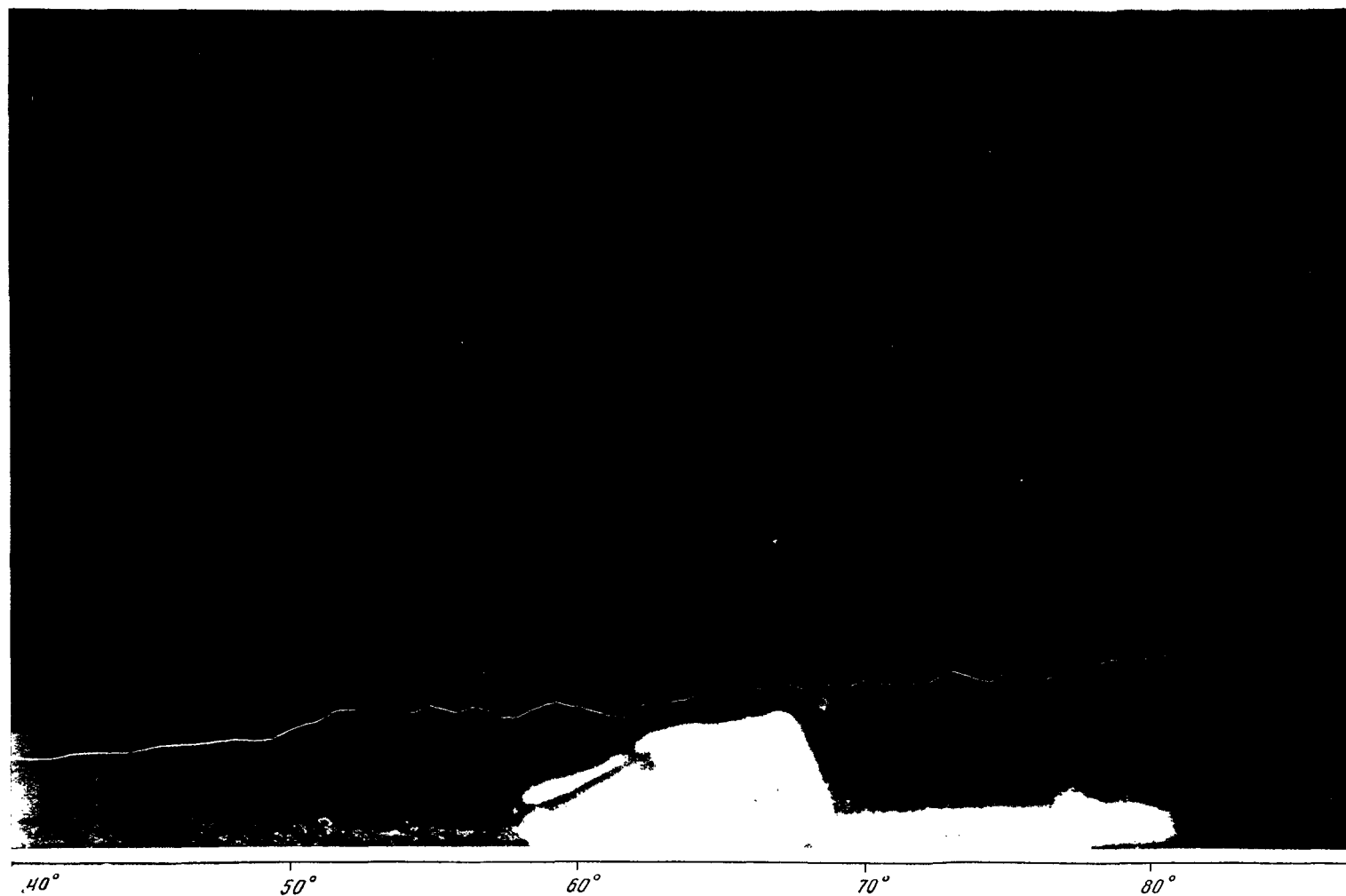


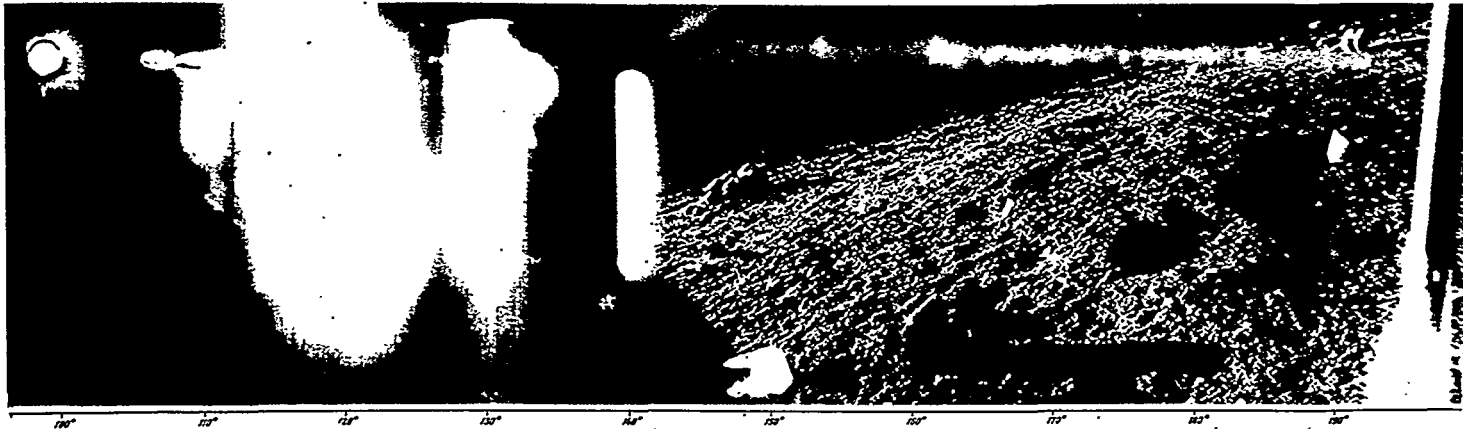
Panorama V, Fragment 5



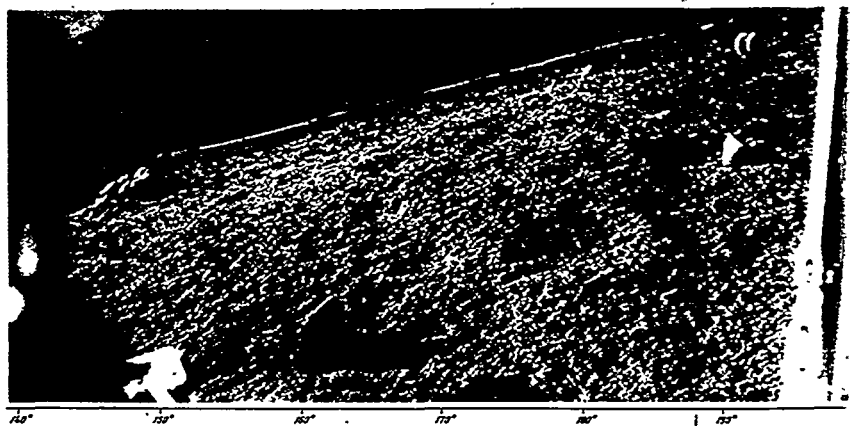
Panorama V, Fragment 6



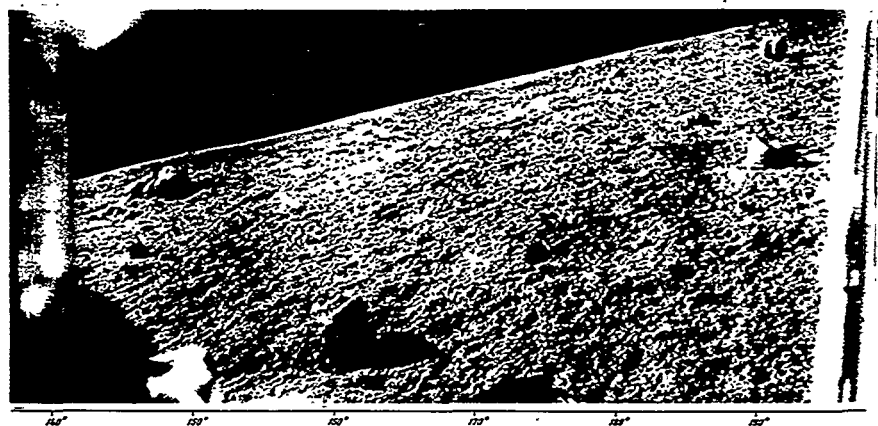




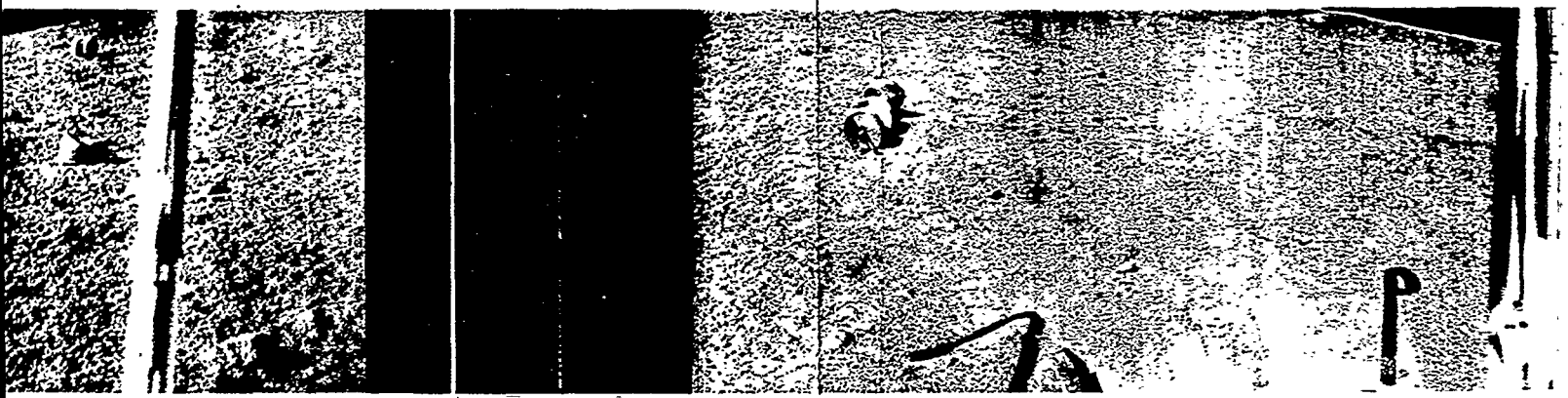
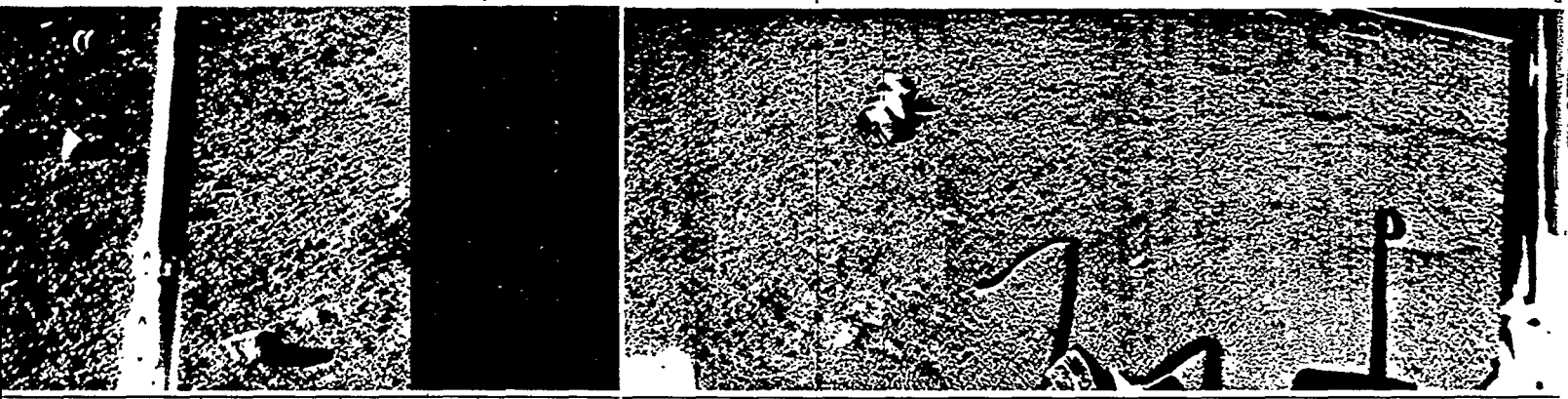
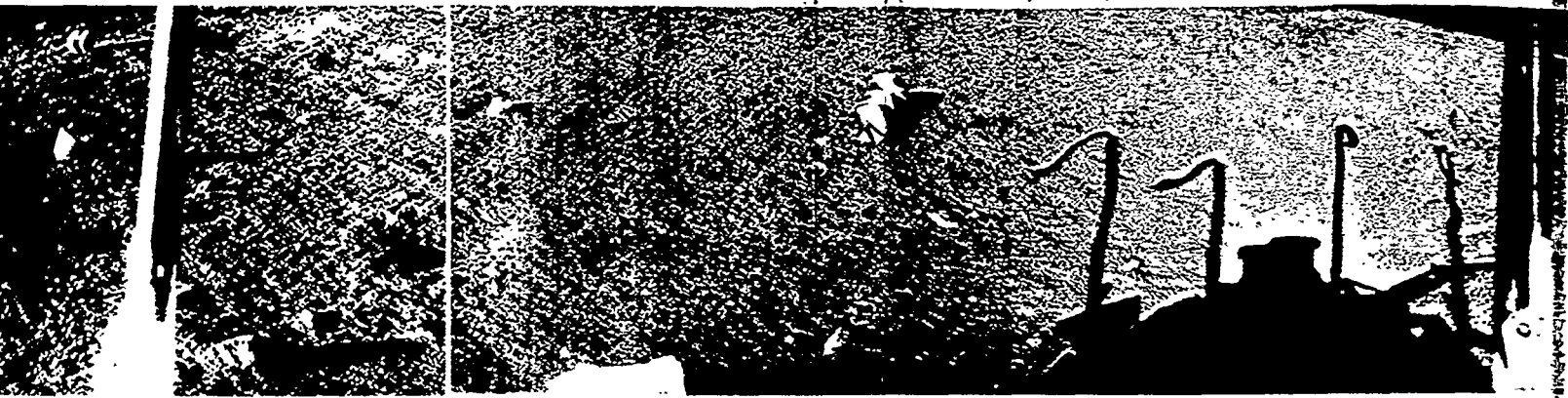
Panorama II

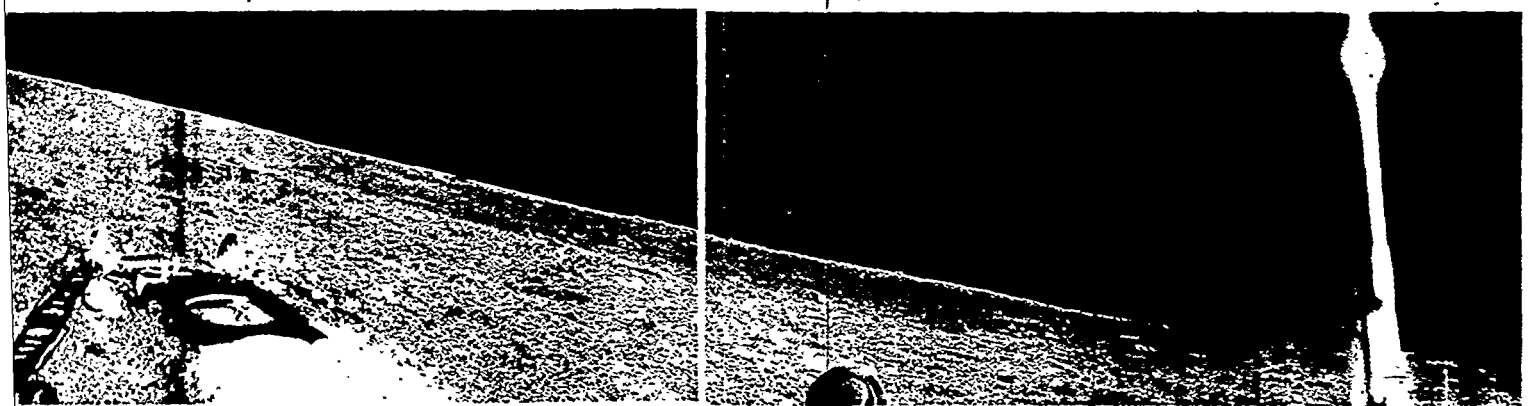
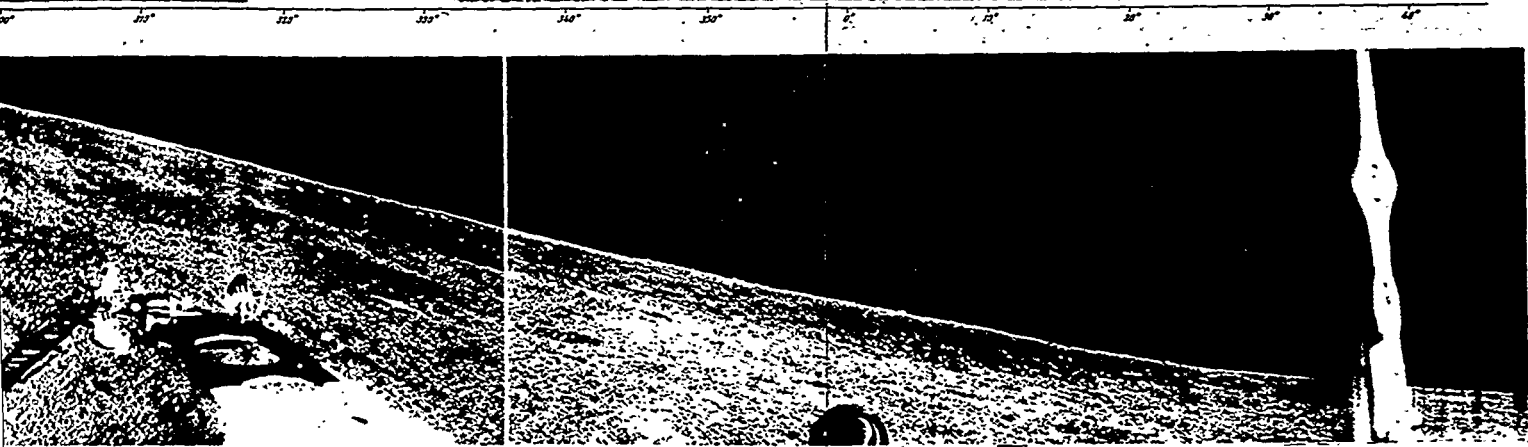
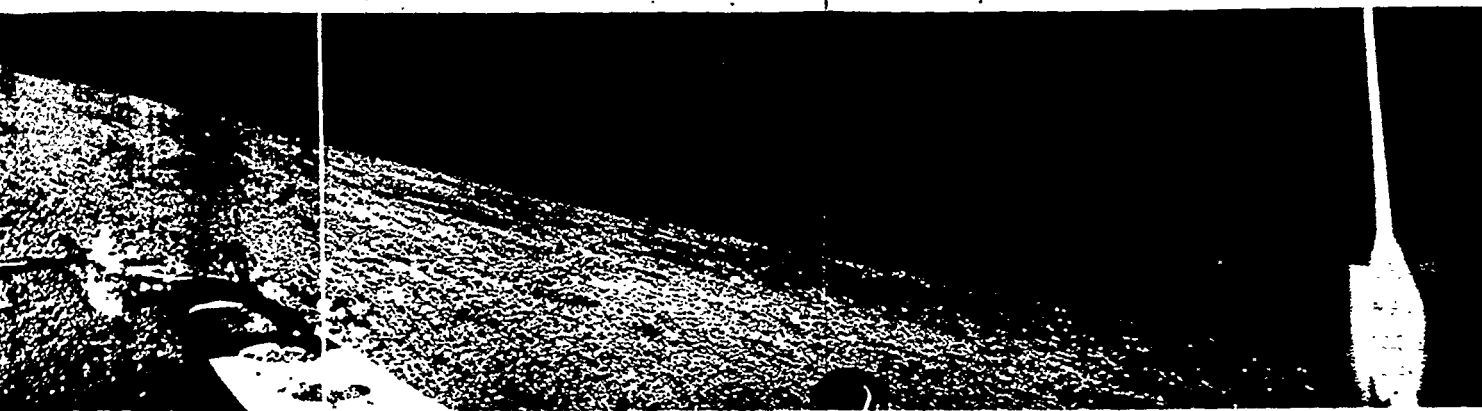


Panorama III

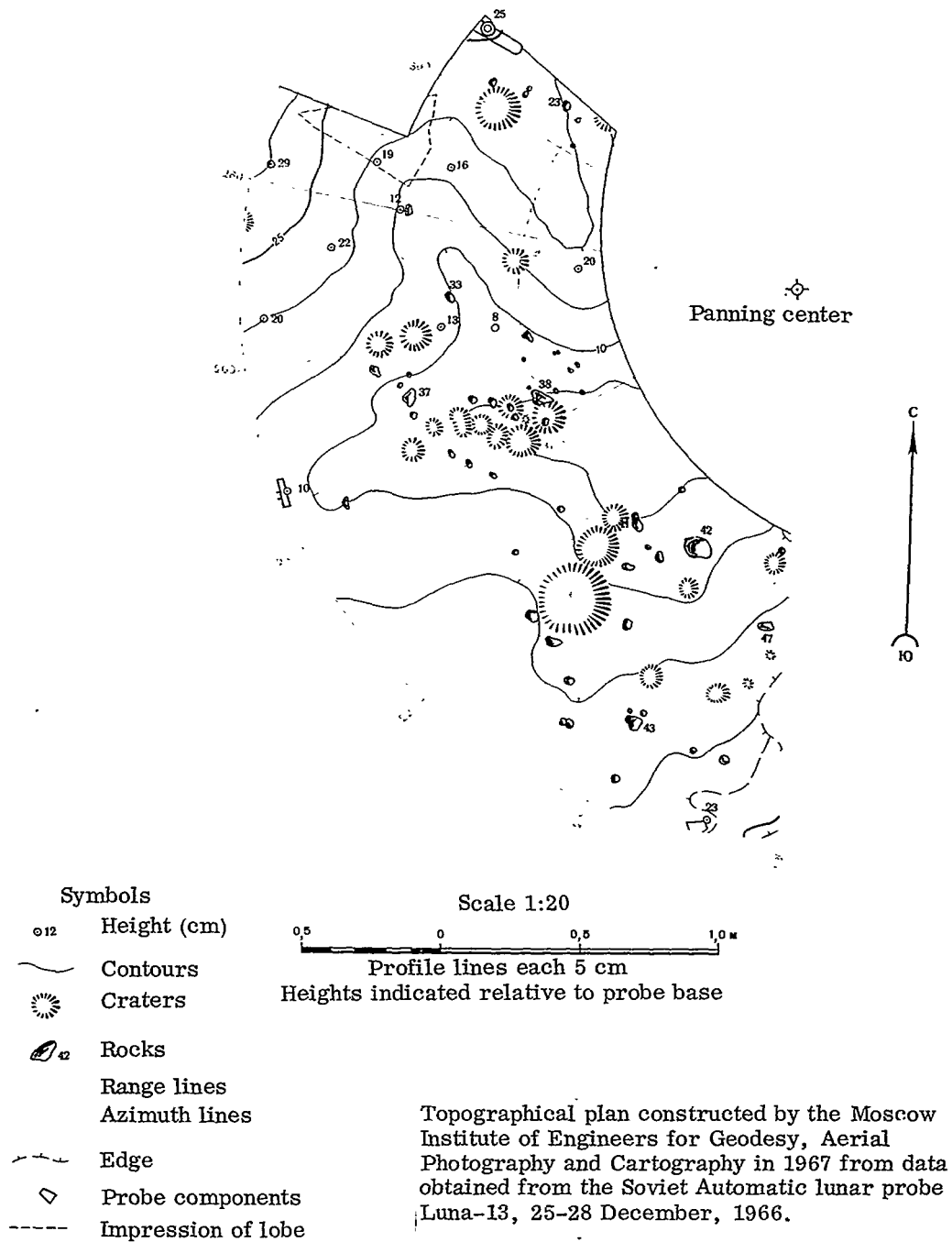


Panorama V

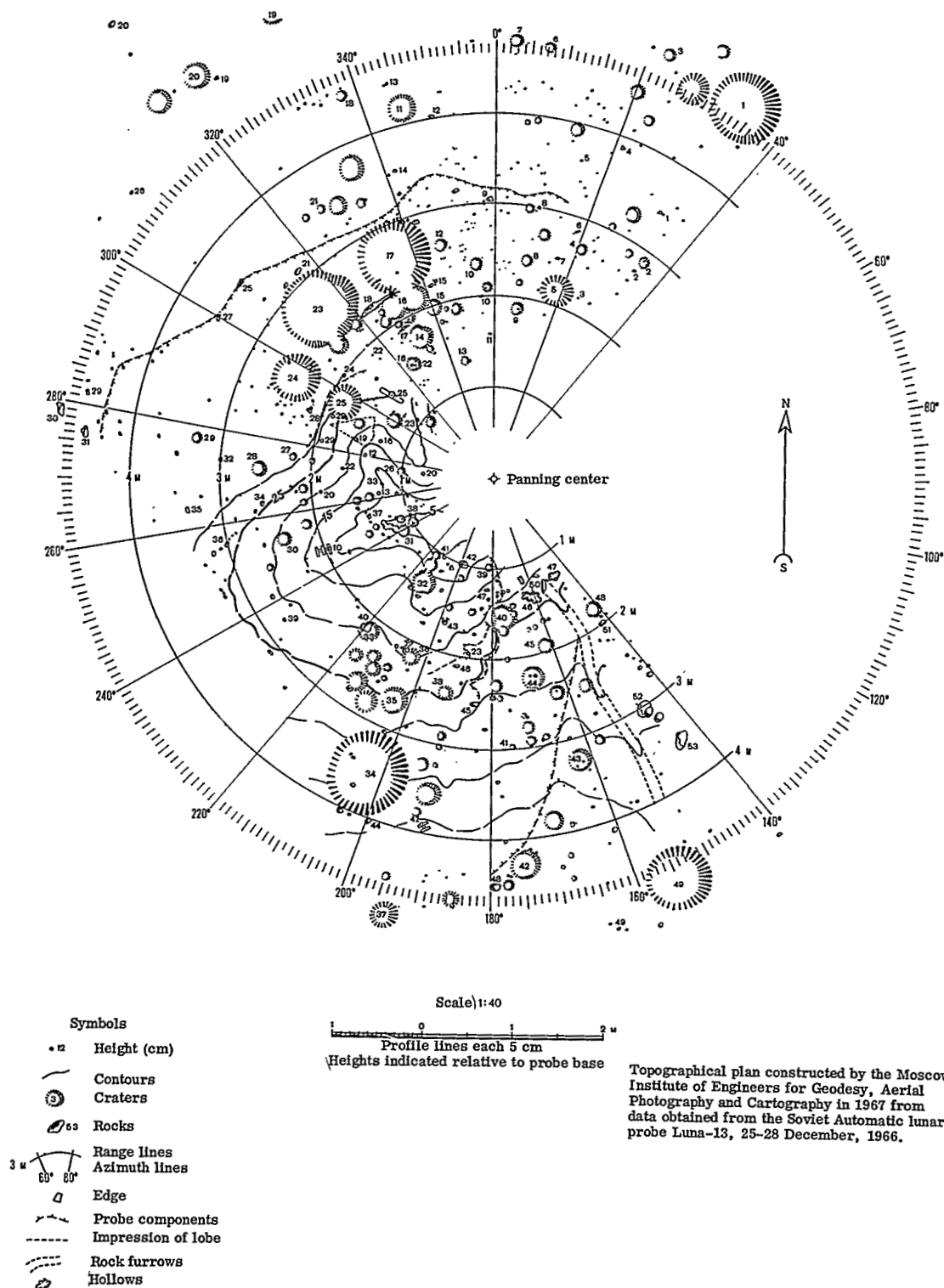




TOPOGRAPHICAL PLAN OF THE LUNA-13 LANDING SITE



SUPPLEMENT: TOPOGRAPHICAL PLAN OF THE LUNA-13 LANDING SITE



Translated for the National Aeronautics and Space Administration by Scripta Technica, Inc. NASW-2036.